



---

**Passive Gust Alleviation WT Model and Test 140408**

**Shijun Guo**  
**CRANFIELD UNIVERSITY**

---

**10/04/2016**  
**Final Report**

DISTRIBUTION A: Distribution approved for public release.

Air Force Research Laboratory  
AF Office Of Scientific Research (AFOSR)/ IOE  
Arlington, Virginia 22203  
Air Force Materiel Command

<b>REPORT DOCUMENTATION PAGE</b>				Form Approved OMB No. 0704-0188	
<p>The public reporting burden for this collection of information is estimated to average 1 hour per response, including the time for reviewing instructions, searching existing data sources, gathering and maintaining the data needed, and completing and reviewing the collection of information. Send comments regarding this burden estimate or any other aspect of this collection of information, including suggestions for reducing the burden, to Department of Defense, Executive Services, Directorate (0704-0188). Respondents should be aware that notwithstanding any other provision of law, no person shall be subject to any penalty for failing to comply with a collection of information if it does not display a currently valid OMB control number.</p> <p>PLEASE DO NOT RETURN YOUR FORM TO THE ABOVE ORGANIZATION.</p>					
<b>1. REPORT DATE (DD-MM-YYYY)</b> 04-10-2016		<b>2. REPORT TYPE</b> Final		<b>3. DATES COVERED (From - To)</b> 30 Sep 2014 to 31 Dec 2015	
<b>4. TITLE AND SUBTITLE</b> Wind Tunnel Model and Test to Evaluate the Effectiveness of a Passive Gust Alleviation Device for a Flying Wing Aircraft				<b>5a. CONTRACT NUMBER</b>	
				<b>5b. GRANT NUMBER</b> FA9550-14-1-0408	
				<b>5c. PROGRAM ELEMENT NUMBER</b> 61102F	
<b>6. AUTHOR(S)</b> Shijun Guo				<b>5d. PROJECT NUMBER</b>	
				<b>5e. TASK NUMBER</b>	
				<b>5f. WORK UNIT NUMBER</b>	
<b>7. PERFORMING ORGANIZATION NAME(S) AND ADDRESS(ES)</b> CRANFIELD UNIVERSITY COLLEGE ROAD BEDFORD, MK43 0AL GB				<b>8. PERFORMING ORGANIZATION REPORT NUMBER</b>	
<b>9. SPONSORING/MONITORING AGENCY NAME(S) AND ADDRESS(ES)</b> EOARD Unit 4515 APO AE 09421-4515				<b>10. SPONSOR/MONITOR'S ACRONYM(S)</b> AFRL/AFOSR IOE	
				<b>11. SPONSOR/MONITOR'S REPORT NUMBER(S)</b> AFRL-AFOSR-UK-TR-2016-0025	
<b>12. DISTRIBUTION/AVAILABILITY STATEMENT</b> A DISTRIBUTION UNLIMITED: PB Public Release					
<b>13. SUPPLEMENTARY NOTES</b>					
<b>14. ABSTRACT</b> This report presents the work and results of Wind Tunnel Model and Test to Evaluate the Effectiveness of a Passive Gust Alleviation Device for a Flying Wing Aircraft. The gust response of the aircraft by using the PGAD integrated at the wing tip was analyzed in a procedure starting from design to numerical modeling and optimization. The previous results show that the PGAD leads to gust response reduction by 18% of the elastic deflection at wingtip, and 15% of the bending moment at the wing root respectively when the wing is constrained at root. For the aircraft with free rigid-body symmetric motion in transverse direction, the wingtip deflection and bending moment relative to the root is reduced by over 20% and 17% respectively. Based on the scaled wing model, a wind tunnel test was performed to validate the effectiveness of PGAD for gust alleviation. The model test results show that a maximum reduction of gust response by 9.4% can be achieved. Finally, the study was further extended to aeroelastic tailoring of the full-scale composite wing for minimum gust response. Together with the PGAD, 28.5% gust alleviation has been achieved.					
<b>15. SUBJECT TERMS</b> EOARD, passive gust alleviation					
<b>16. SECURITY CLASSIFICATION OF:</b>			<b>17. LIMITATION OF ABSTRACT</b>  SAR	<b>18. NUMBER OF PAGES</b> 104	<b>19a. NAME OF RESPONSIBLE PERSON</b> CUMMINGS, RUSSELL
<b>a. REPORT</b>  Unclassified	<b>b. ABSTRACT</b>  Unclassified	<b>c. THIS PAGE</b>  Unclassified			<b>19b. TELEPHONE NUMBER (Include area code)</b> 011-44-1895-616021

**Final Technical Report****(FA9550-14-1-0408)****Wind Tunnel Model and Test to Evaluate the  
Effectiveness of a Passive Gust Alleviation  
Device for a Flying Wing Aircraft****Dr Shijun Guo****Prof. Otto Sensburg****Aerospace Engineering****Cranfield University, UK****20 March 2016**

## ABSTRACT

This report presents the work and results of Wind Tunnel Model and Test to Evaluate the Effectiveness of a Passive Gust Alleviation Device for a Flying Wing Aircraft. The project is funded by EOARD/USAFRL from 30 Sep. 2014 to 30 Dec. 2015 (Contract No. FA9550-14-1-0408).

This is a project following the previous one to investigate the passive gust alleviation device (PGAD) for a Sensorcraft of high aspect ratio flying-wing configuration (FA8655-11-1-3073). The gust response of the aircraft by using the PGAD integrated at the wing tip was analysed in a procedure starting from design to numerical modelling and optimization. The previous results show that the PGAD leads to gust response reduction by 18% of the elastic deflection at wingtip, and 15% of the bending moment at the wing root respectively when the wing is constrained at root. For the aircraft with free rigid-body symmetric motion in transverse direction, the wingtip deflection and bending moment relative to the root is reduced by over 20% and 17% respectively. This current project is aimed at validating the previous analysis and further evaluating the PGAD effectiveness. The project has been carried out through the following stages: design a scaled wing model of dynamic similarity with the full-scale wing; build the model; design and build a gust generator; perform wind tunnel test and measure the gust alleviation with the PGAD effect. In addition, aeroelastic tailoring of the composite wing for the full scale aircraft gust response in conjunction with PGAD has been carried out.

The scaled wing model of dynamic similarity is designed as 1:25 in dimension with respect to the full-scale aircraft. The full-scale wing structure was first simplified to an equivalent Basic Beam Model (BBM). The Scaled Beam Model (SBM) of the wing structure was then designed and built to keep equivalent stiffness and mass distribution to the BBM model based on the scale factors. The scaled wing model was validated by a ground vibration test with a frequency deviation within 7% for the first five modes.

Based on the scaled wing model, a wind tunnel test was performed to validate the effectiveness of PGAD for gust alleviation. The model test results show that a maximum reduction of gust response by 9.4% can be achieved.

Finally, the study was further extended to aeroelastic tailoring of the full-scale composite wing for minimum gust response. Together with the PGAD, 28.5% gust alleviation has been achieved. The investigation has explored a great potential of applying the passive gust alleviation technology to unmanned aircraft.

## **ACKNOWLEDGEMENTS**

Dr. S. Guo and O.T. Sensburg acknowledge European Office of Aerospace Research and Development (EOARD) and USAFRL for their financial support to this research project. We also thank Dr. Raymond Kolonay at USAF AFMC AFRL and Dr. Gregg Abate at EOARD for their technical advice and support, and acknowledge Dr. Y.Liu for his technical contribution to the project during his PhD study at Cranfield University.



## TABLE OF CONTENTS

1 INTRODUCTION.....	1
2 . SCALED PHYSICAL MODEL DESIGN.....	4
2.1 Scale Factor Determination .....	4
2.2 Model Design.....	5
2.3 Numerical Analysis .....	8
2.4 Manufacture and Assembly .....	14
2.5 Ground Vibration Test.....	15
3 . GUST GENERATOR DESIGN .....	19
3.1 General Requirement.....	19
3.2 Preliminary Design.....	19
3.3 Manufacture.....	27
3.4 Load Free Functional Test .....	27
4 WIND TURNNEL TEST OF THE SCALED WING MODEL .....	28
4.1 Test Plan and Preparation .....	28
4.2 Experimental Validation of Gust Flow Field .....	34
4.3 Gust Alleviation Test.....	38
5 AEROELASTIC TAILORING .....	47
5.1 Aeroelastic Tailoring of Baseline Wing.....	47
5.2 Gust Response of Wing with PGAD.....	57
6 CONCLUSION .....	60
REFERENCES.....	61
APPENDIX A . GUST RESPONSE WITH PGAD .....	72
A.1 PGAD Design .....	72
A.2 Gust Response Analysis .....	73



---

A.2.1 Response with Longitudinal Rigid Body Motion .....	74
A.2.2 Open Loop Active Control Case .....	77
APPENDIX B . POSSIBLE DESIGNS FOR GUST GENERATOR .....	80
APPENDIX C . TORSION SPRING DESIGN .....	81
APPENDIX D . TEST INSTRUMENTS SPECIFICATIONS .....	83

## 1 INTRODUCTION

This project concludes the second phase of the investigation of a passive gust alleviation device (PGAD) for minimizing the gust response of a flying wing aircraft. The concept of PGAD is a device mounted at the wing tip through a rigid shaft and rotation spring as illustrated in Figure 1-1. The rotation shaft is designed to be ahead of the aerodynamic pressure centre, which leads to a nose down rotation in response to an increase of aerodynamic force such as gust load. Such a passive rotation will reduce the local and therefore overall aerodynamic load on the wing as a result of a reduced angle of attack as shown in Figure 1-2. In the previous project (final report for FA8655-11-1-3073), the effectiveness of the PGAD technology for the application of high aspect ratio flying-wing aircraft has been studied by numerical simulation. The results show that gust alleviation up to 18% for wingtip deflection and 20% for wing-root bending moment can be achieved. In the current project, the investigation has been extended to free transverse rigid body motion including heave and pitch mode and an actively controlled PGAD device for further comparison and evaluation (see APPENDIX A. GUST RESPONSE WITH PGAD in this report). Based on the above study, this project is focused on the scaled model of dynamic similarity and wind tunnel test to validate the PGAD gust alleviation effectiveness. The research proposal was made with a 15-month contract granted by EOARD/AFRL. In the proposal, the work programme and time schedule as shown in Table 1-1 was set for the project.

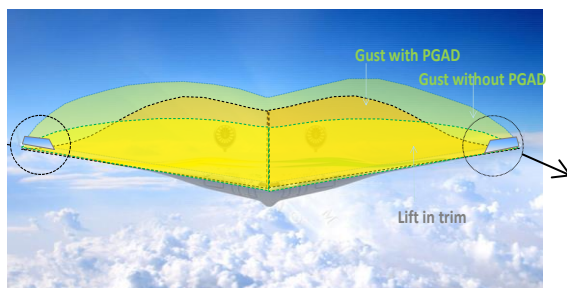


Figure 1-1 Gust load alleviation with PGAD

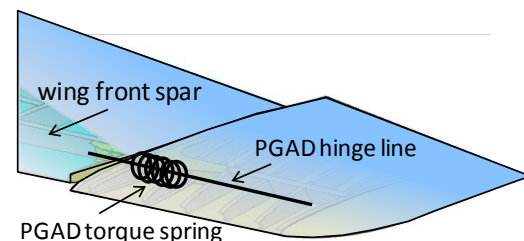


Figure 1-2 PGAD outline

**Table 1-1. Work Programme and Time Schedule**

#	Activity	Elapsed Time [months]
1.	Design, Analysis and Manufacture	
1.1.	Design, FE modelling and analysis of a dynamically scaled half aircraft test model of 1.24 m with the PGAD and control surface	3
1.2.	Design and manufacture of the gust generator (frame, blades, actuation and control system)	2
1.3.	Manufacture of the half aircraft test model mounted with the PGAD and control surface device	3
1.4.	Stiffness and vibration experiment of the test model to validate the analysis and measure the static and dynamic behaviour of the manufactured model	1
2.	Wind Tunnel Test and Measurement	
2.1.	Wind tunnel test setup (mounting the gust generator and model, and measurement devices and equipment)	1
2.2.	Test case 1: the steady aerodynamic force and deflection with the PGAD locked and unlocked; the control surface actuated to simulate a manoeuvre action with the PGAD locked & unlocked.	1
2.3.	Data processing and analysis to evaluate the influence of the PGAD on the flight control effectiveness	0.5
2.4.	Test case 2: In gust response test, the unsteady aerodynamic force and deflection will be measured with the PGAD locked / action	1.5
2.5.	Data processing and analysis to evaluate the PGAD effectiveness	0.5
2.6.	Aeroelastic tailoring of composite wing together with the PGAD	1.0
3.	Final technical report	0.5

The project has been carried out through the following stages: design of the scaled wing model, including the gust generator design, model manufacture and assembly; The wind tunnel test model is designed and manufactured under a constraint of dynamic similarity with the original full-scale wing; Wind tunnel testing to validate the PGAD gust alleviation. In addition, aeroelastic tailoring of the full-scale composite wing has been carried out to evaluate the reduction of gust response in conjunction with PGAD.

The Report Chapter 2, presents how the scaled wing model of 1:25 dimension ratio is designed subject to dynamic similarity with respect to the full-scale wing. The scale factors are chosen based on physical parameters and aeroelastic characteristics of the wing. The full-scale wing structure was first simplified to an equivalent Basic Beam Model (BBM). The Scaled Beam Model (SBM) of the wing structure was then designed and built to keep equivalent stiffness and mass distribution as the BBM model following the scale factors. The scaled wing model was validated by a ground vibration test with a frequency deviation within 7% for the first five dominant modes.

In Chapter 3, a gust generator with two rotating blades was designed and manufactured to induce a transverse turbulence for wind tunnel test. A CFD simulation was conducted to analysis the downstream airflow field of the gust generator for transverse flow velocity. The maximum offset value of flow velocity at 8C (eight times of blade chord length) achieved 1.3%.

In Chapter 4, the wind tunnel test of the scaled wing model is presented, including the experimental validation of gust flow field and gust alleviation test of the PGAD device. The test results show that with PGAD, a reduction of gust response of the wing model by 9.4% has been achieved.

Finally, the study was further extended to aeroelastic tailoring of the full-scale composite wing for minimum gust response, which shows that, together with the PGAD, the aeroelastic tailored wing can achieve 28.5% gust alleviation. This indicates a great potential of the passive gust alleviation technology.

## 2 . SCALED PHYSICAL MODEL DESIGN

For wind tunnel test and validation of PGAD, a 1:25 scaled physical model of the wing has been designed and manufactured. The scaled model must have similar aeroelastic characteristics with the full-scale aircraft. In this chapter, the design and dynamic analysis, manufacture and Ground Vibration Test (GVT) of the scaled model are presented.

### 2.1 Scale Factor Determination

Determination of a series of scale factors was a starting point of the model design based on the theoretical laws [73]. The scale factors can be classified into two categories, independent scale factors and induced factors as listed in Table 2-1. The induced factors are calculated from the independent ones, which are determined based on the design objective and test conditions. Scale factor  $\eta$  with specific subscript represents the ratio of the specified quantity of wind tunnel model and the full-scale aircraft.

**Table 2-1 Model design scales**

	Design Scale	Symbol	Scale factor
Independent Scale	Dimension	$\eta_L$	0.040
	Density	$\eta_\rho$	1.000
	Velocity	$\eta_V$	0.115
Induced Scale	Mass	$\eta_m = \eta_\rho \eta_L^3$	6.400E-5
	Inertia	$\eta_{Jm} = \eta_\rho \eta_L^5$	1.024E-7
	Rotation spring stiffness	$\eta_{k_\theta} = \eta_\rho \eta_V^2 \eta_L^3$	8.464E-7
	Section bending stiffness	$\eta_{EI} = \eta_\rho \eta_V^2 \eta_L^4$	3.382E-8
	Frequency	$\eta_f = \eta_V / \eta_L$	2.874

Normally, the larger scale model is likely to have higher precision of dynamic similarity and easier manufacture. However, the large test model also means higher expense in running larger wind tunnel. So, the dimensional scale of  $\eta_L = 1:25$  was mainly determined by a compromise between the benefit of larger model and the limit of cost and wind tunnel availability.

$\eta_V$  is flutter speed scale here. The flutter speed of scaled model for wind tunnel test is an assigned value, which is 36m/s in this case considering tunnel speed limit.  $\eta_\rho$  is 1.0 because both wind tunnel test and the aircraft flight condition are at sea level. The remaining induced scales were worked out from the independent scale factors.

## 2.2 Model Design

First of all, the full-scale aircraft structure was simplified to an equivalent Basic Beam Model (BBM) that was practical for manufacture in small scale. The BBM had a configuration of single spar for outer wing and double spars for inner wing as shown in Figure 2-1. It was carefully designed in an iterative procedure to keep the dynamic similarity of the original structure. A Scaled Beam Model (SBM) as a scaled copy of BBM was created to keep equivalent stiffness and mass distribution as the BBM model following the scale factors defined above.

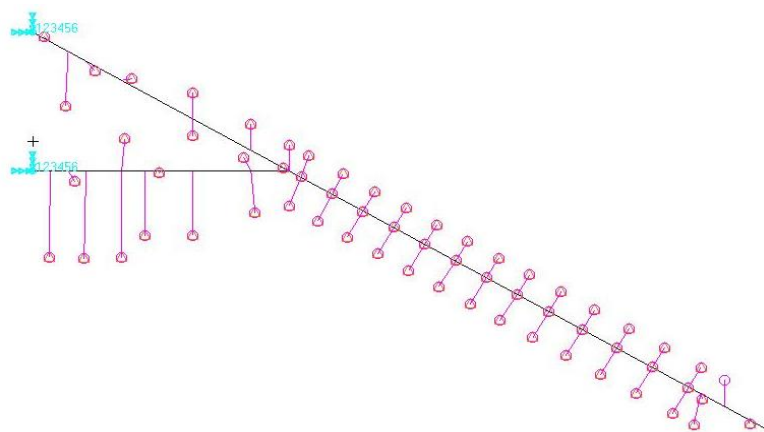


Figure 2-1 The Basic Beam Model

### 2.2.1 Spar

The spars were designed to have equivalent stiffness of the original model since all the loads are experienced by the spars. The model stiffness for each spanwise section can be obtained from the full FE model using the following equations (2-1) and (2-2).

$$M_b = EIw'' \quad (2-1)$$

where

$M_b$	The bending moment	
$w$	The deflection	
$EI$	The bending stiffness	
	$T = GJ\theta'$	(2-2)

where

$T$	The torque
$\theta$	The rotational angle
$GJ$	The torsional stiffness

#### 2.2.1.1 Rib and Stringer

The ribs and stringers were designed to maintain the airfoil and transfer aerodynamic load. There were heavy ribs and light ribs but mainly the former was designed to transfer the aerodynamic loads to the spar. It meant that each section of the frame was connected to the spar at a single point and the load would be transferred without additional stiffness being introduced. Both heavy and light rib webs had oval holes to save weight. Balanced mass was also attached onto the heavy rib to tailor the detailed mass redistribution.

### 2.2.2 Skin

The wing box was covered by a shrinkable membrane material as skin. It should be noted that the skin was also isolated section by section to avoid

additional stiffness. The skin mass was estimated by the applied area and density of material.

### 2.2.3 PGAD

#### a) Torsion spring

The torsion spring designed for the physical model can be categorized as long leg spring. The calculated spring stiffness 47.9 Nmm/rad is slightly less than the required value 49.1 Nmm/rad which is scaled down from the optimized PGAD parameter following the factor, see . .

#### b) Rigid Shaft

The shaft is located at 15% chordwise along Y axis in global coordinate system as illustrated in the FE model. The inboard end of the shaft is supported by a component with two bearings while the outboard end is fixed to the integral PGAD frame. The aerodynamic load on the device is transferred from the shaft to the spar through the component except the pitch degree of freedom which is constrained by the torsion spring assembled coaxially with the shaft.

#### c) Device Frame

An integral structure configuration shown in Figure 2-2 was designed and manufactured as the device frame to meet the mass restriction since it is proved that the flutter characteristic of the wing is quite sensitive to the device mass. Both the spring arm and the shaft were fixed on a heavy rib with 1/3 chord length attached at the inboard side of the device frame.



Figure 2-2 The 1:25 scaled PGAD model



## 2.2.4 Base

As the inner wing has a two-spar configuration, a rigid base along the mid line of the aircraft was made to fix and support the spars. For the vibration and wind tunnel test, it is critical to ensure that the base was stiff enough to constrain all the six degrees of freedom at wing root and avoid modal interaction between base and the spars.

## 2.3 Numerical Analysis

### 2.3.1 Mass Distribution

In the design of the dynamic similarity model, it is always necessary and important to analyse the mass distribution including the mass, inertia and CG. The procedure in determination of the equivalent mass is listed below:

- 1) Build up a CATIA model of scaled wing and input the density of each material to be used;
- 2) Measure the mass properties of each spanwise section in CATIA model;
- 3) Measure the mass properties of each section in FE model (SBM);
- 4) Calculate mass properties to be balanced and relocate them to heavy ribs.

It is worth mentioning that not only mass and CG but also inertia equivalents must be considered as described in Equation (2-1) when redistributing the mass properties.

$$\begin{cases} m_A + m_B = m_P \\ m_A l_A = m_B l_B \\ m_A \bar{l}_A^2 + m_B \bar{l}_B^2 = J_{mp} \end{cases} \quad (2-3)$$

where,

Subscript A and B refer to the new points at which the concentrated mass will be relocated; while subscript P is the original CG of the current wing section;

$m_A, m_B$  are the masses of point A and point B;

$l_A, l_B$  are the lengths between original point and new point respectively;

$\bar{l}_A, \bar{l}_B$  are the lengths between new point and stiffness centre line;

$J_{mp}$  means the moment of inertia at original point.

### 2.3.2 Vibration and Flutter Analysis

In Table 2-2, the SBM's frequencies in the column named 'target' were obtained from the natural frequencies of BBM multiplied by the frequency scale  $\eta_f$  in Table 2-1. The column 'Ref.' is the corrected frequency of SBM by replacing the mass and CG data in SBM with those measured in Physical Test Model (PTM). It was found that the first three modes, the first bending, the PGAD rotation and the second bending, are very close to the target values. The third bending and first torsion modes however have over 10% division from the target due to the simplification of the spar cross section of the model and more difficulty to meet the higher order target. Since they do not have significant influence on the gust response, the accuracy of the high order modes was not a big concern.

According to flutter analysis of the Scaled Beam Model, the flutter mode is close to the first bending mode. The flutter result also has a good accordance with the targets. When comparing Figure 2-3 with Figure 2-4, it can be seen that the trends of frequency and damping were almost the same. This meant the major aeroelastic characteristics of the wing were successfully simulated.

**Table 2-2 The vibration calculation results**

Mode Name	Frequency (Hz)					
	Numerical simulation results			Experimental test results		
	Target	SBM	Error	Ref.	PTM	Error
The First Bending	2.020	1.974	-2.3%	1.945	1.938	-0.4%
PGAD Rotation	5.539	5.610	1.3%	5.620	5.313	-5.5%
The Second Bending	9.599	9.730	1.4%	9.686	9.563	-1.3%
The Third Bending	20.331	22.514	10.7%	22.195	20.688	-6.8%
The First Torsion	37.003	31.751	-14.2%	30.718	31.125	1.3%

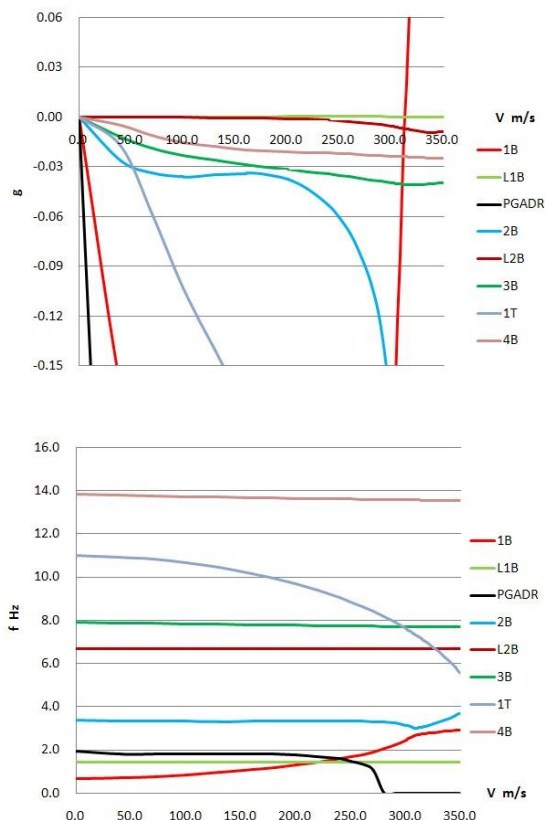


Figure 2-3 BBM V-g-f plot

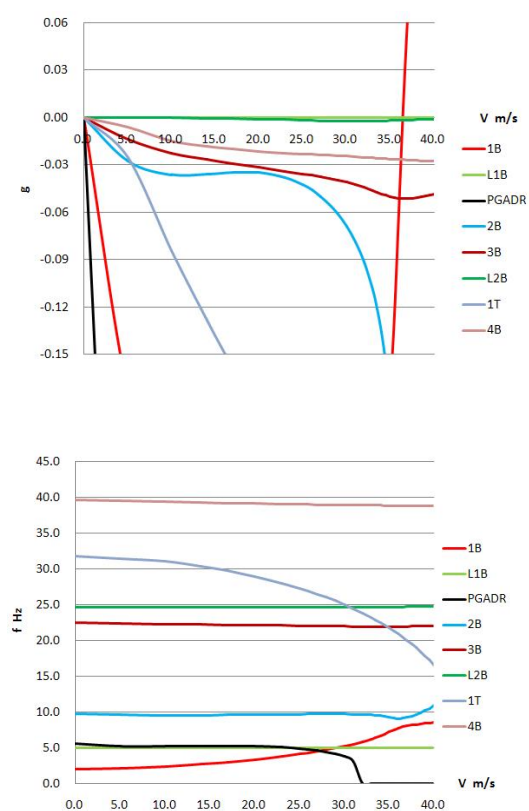


Figure 2-4 SBM V-g-f plot

### 2.3.3 Additional Analysis with Variable Parameters

Since the wing fundamental mode and PGAD rotation mode are both quite sensitive to PGAD design parameters, parametric study was conducted to evaluate the impact of the mass, CG and the spring stiffness on the aeroelastic characteristics.

In this study, the PGAD mass variation covered the range from one to three times of the initial design. The results in Figure 2-5 and Figure 2-6 show that both the flutter frequency and flutter speed decrease significantly with increasing PGAD mass.

In the study of other variable parameters, the CG of the PGAD was shifted from 10% to 70% of the local chord. Two cases, initial mass at 7.9g and double mass at 15.7g were analysed individually. As presented in Figure 2-7 and Figure 2-8, the flutter frequency and speed reduced slightly when the CG moved

backwards while the drop in frequency of the PGADR mode was much more dramatic.

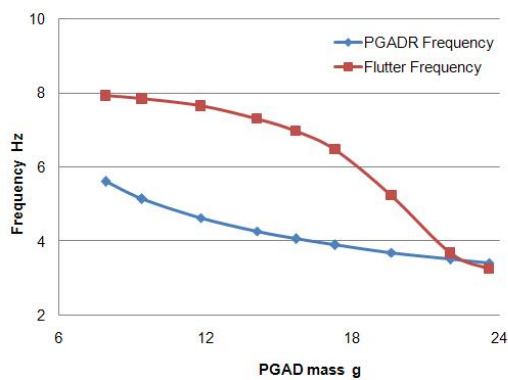


**Figure 2-5 Frequencies vs. PGAD mass**

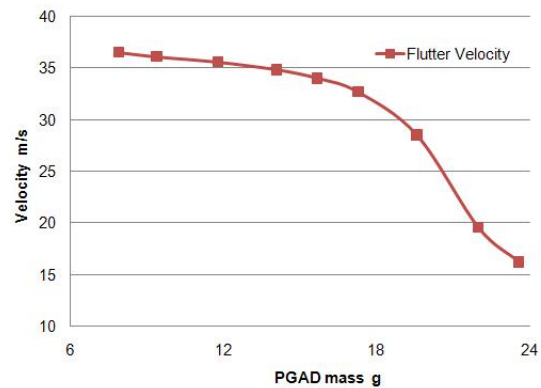


**Figure 2-6 Flutter Velocity vs. PGAD mass**

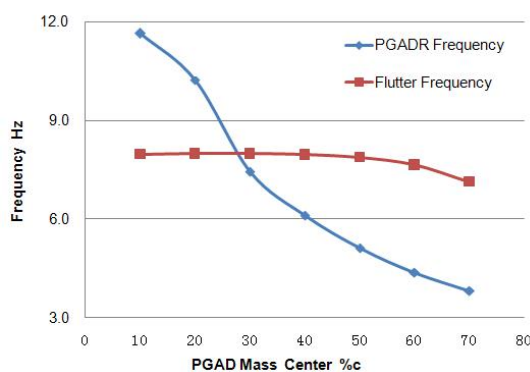


**Figure 2-7 Frequencies vs. PGAD CG**

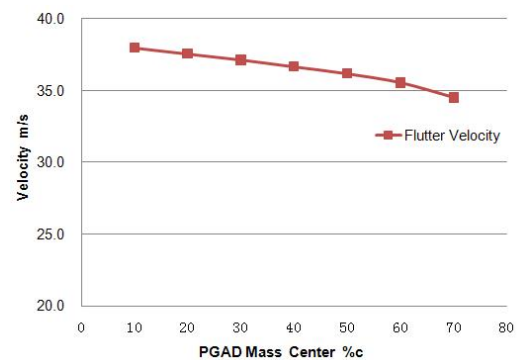


**Figure 2-8 Flutter Velocity vs. PGAD CG**

In Figure 2-9 and Figure 2-10, there was little change in flutter even if the spring stiffness was increased from 0.1 to 10 times of its original value. But, the frequency of the device mode increased obviously.

In summary, the aeroelastic characteristics, especially the flutter velocity, were found to be sensitive to PGAD mass. In this study case, there was a significant drop in flutter velocity if the PGAD mass was over 15.7g. So, the mass must be controlled since any flutter during the gust alleviation test is undesirable.

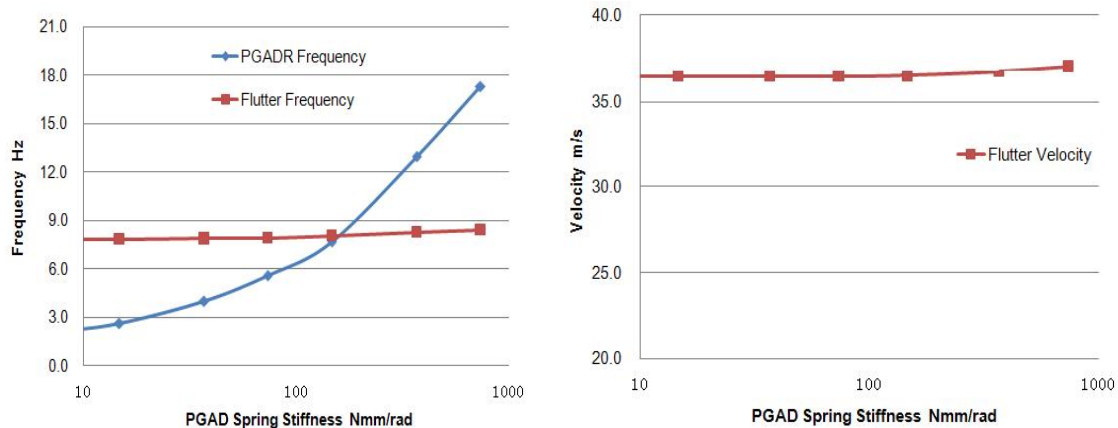


**Figure 2-9 Frequencies vs. spring stiffness    Figure 2-10 Flutter Velocity vs spring stiffness**

### 2.3.4 Gust Response Analysis

A gust response analysis was carried out once the scaled beam model had been designed. The wing tip deflection at different gust gradients is shown in Figure 2-11.

The 3.2% error between the SBM and the full FE model means that the gust response of the BBM is in accordance with initial design. So, the gust response characteristics can be presented well by the SBM. Further analysis will be conducted after a wind tunnel test which will provide more practical information and help to determine the final design variables.

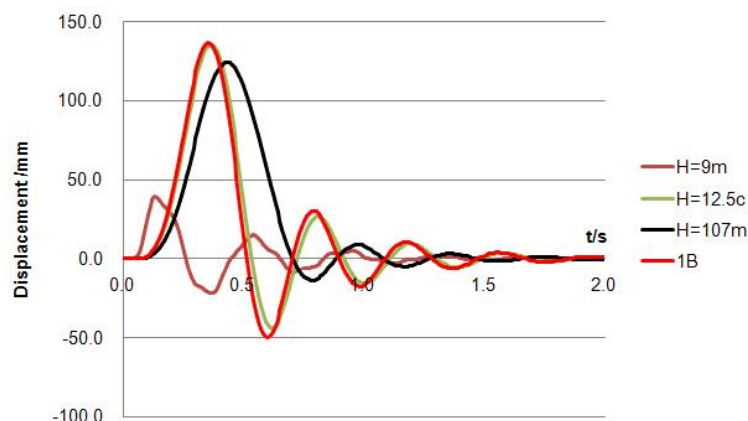


**Figure 2-11 Gust response of SBM**

### 2.3.5 CFD Simulation

Although a lot of aerodynamic study has been done in the others' research, further analysis in this particular case was necessary to gain more information.

As shown in Figure 2-12, the PGAD lift of the SBM is approximately linear for rotation angle variation from  $0^\circ$  to  $20^\circ$  when the wing AoA changes from  $0^\circ$  to  $5^\circ$ . The induced bending moment at the SBM wing root by CFD simulation agrees well with the lifting surface theory using NASTRAN as shown in Figure 2-13.

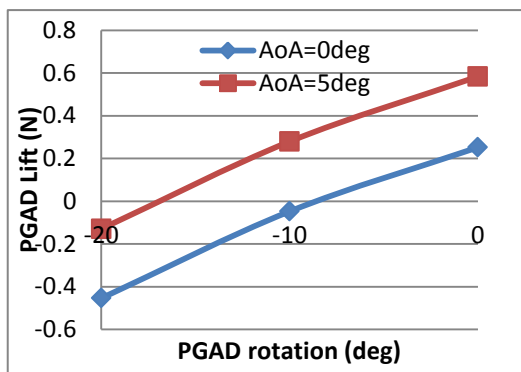


Figure 2-12 PGAD lift Vs. rotation

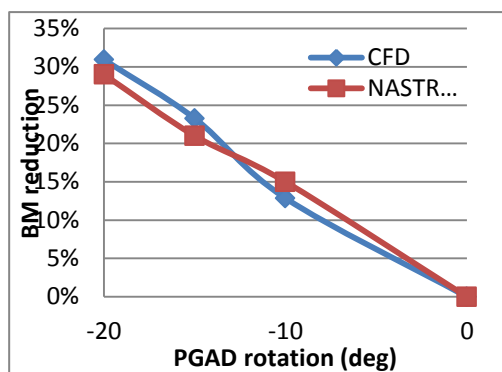


Figure 2-13 BM reduction due to PGAD

Comparing with the one when PGAD is treated as an independent lifting surface, the reduction of the PGAD lift is almost halved when it was attached to the wing, see Figure 2-14. One explanation might be that the upwash, which is introduced by the vortex due to the gap between the wing and PGAD as shown in Figure 2-15, caused reduction of the PGAD efficiency.

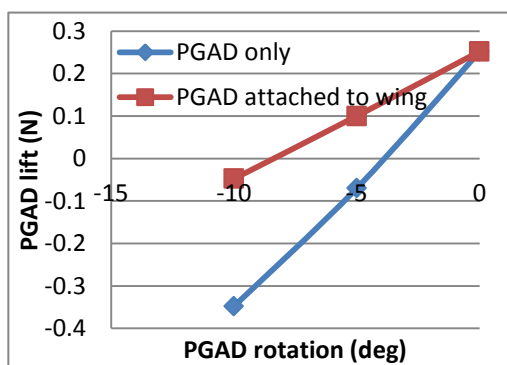


Figure 2-14 PGAD lift comparison (AoA=0)

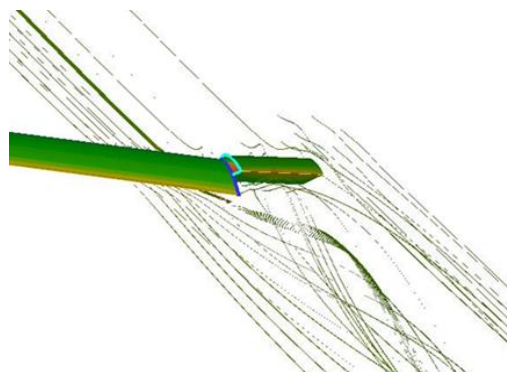
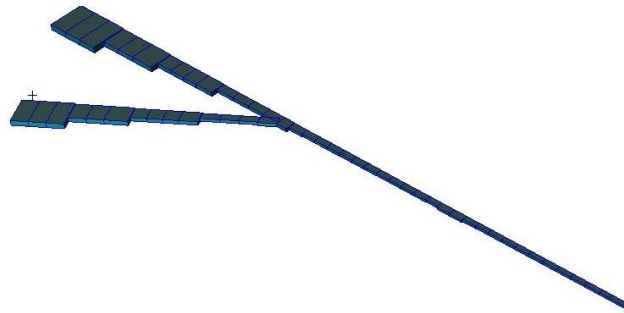


Figure 2-15 Flow field around PGAD

## 2.4 Manufacture and Assembly

Based on the numerical calculation, the SBM model was designed in CATIA. To facilitate manufacture and assembly, spars made of HE30 aluminium alloy were divided into 3 parts including two spars (front spar and rear spar) for the inboard wing and one outboard spar, see Figure 2-16.

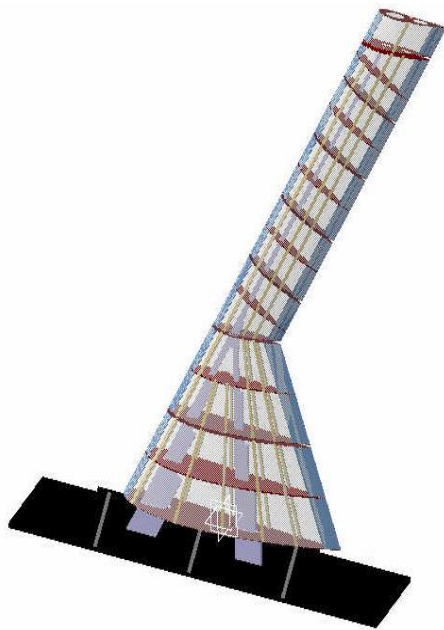


**Figure 2-16 The metallic spar CATIA model**

Aerofoil shape was maintained by heavy ribs, light ribs, stringers, leading edge and trailing edge. Both light ribs and heavy ribs were made of ply board with different thicknesses, 1.5mm and 3mm respectively. All ribs were manufactured by laser cutter. Stringers were built with balsa wood. High density engineering foam was used to create the leading and trailing edges. The skin was a special material named Ripmax Lightweight Covering Tissue, which would shrink when soaked with special cellulose dope.

It should be noted that the assembly procedure was different to normal. The wing box was separated into several spanwise segments to make sure that only the spar was subject to aerodynamic loads. So, each box had one heavy rib in the middle and two adjacent light ribs on the left and right. The heavy rib was bonded to the spar while the light ribs were connected to the heavy ribs by stringers, leading edge and trailing edge. The skin was applied after a Ground Vibration Test (GVT) to reserve an open access to the sensors. And also, the skin was separated for each segment to avoid additional stiffness. Distributed masses were built by lead blocks attached to the heavy ribs according to numerical calculation.





a) CATIA wing model



b) Physical wing model

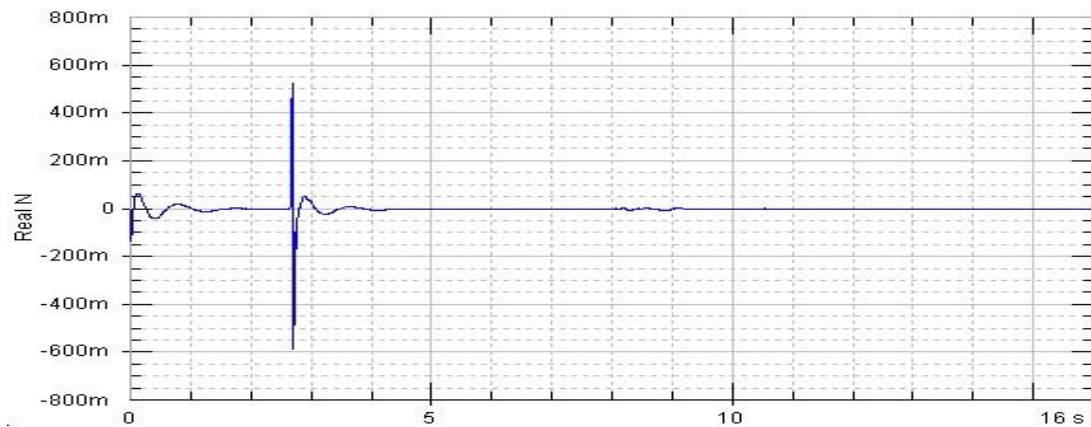
**Figure 2-17 The 1:25 scaled wing model**

## 2.5 Ground Vibration Test

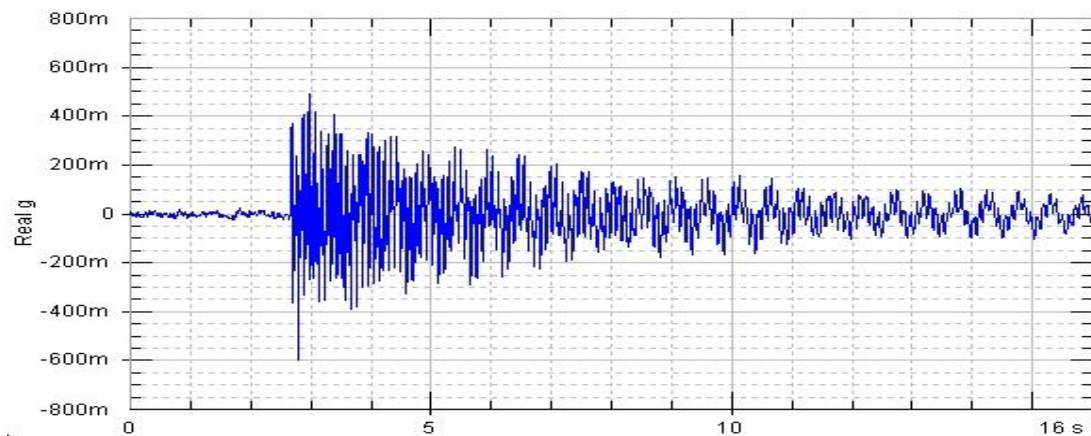
Once the physical model as shown in Figure 2-17 was assembled, the GVT could be run to verify and update the simulation. An accelerometer was fixed at the outboard tip of the spar with its sensitivity axis in Z direction. Two full-bridge strain gauges were attached at the roots of front spar and rear spar respectively to measure the bending moment. The pulse excitation applied to the spar tip by an impulse hammer was recorded as well as the responses of the accelerometer and the strain gauge as shown in Figure 2-18.

It can be seen in Table 2-2 that in practice the frequencies of all the dominant modes agreed well with those in the numerical analysis at a 6.8% maximum error. This was a reasonable value for engineering. It would have been more accurate if a more complicated cross-section shape had been used in place of the rectangular one. The frequency and damping of primary structural modes was achieved by the data post-process, see Table 2-3. Those data, especially damping, can be employed as a reference for the definition of related parameters in the aeroelastic analysis.

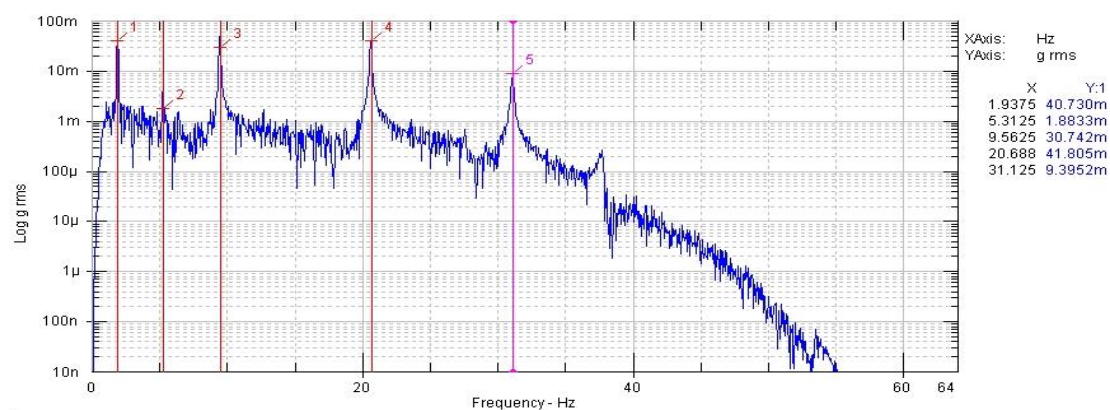




a) Excitation input



b) Accelerometer response time history



c) Response in frequency domain

**Figure 2-18 GVT results**

**Table 2-3 Major modes frequency and damping**

<b>Mode Name</b>	<b>Frequency (Hz)</b>	<b>Damping (%)</b>
The First Bending	1.938	2.11
PGAD Rotation	5.313	4.78
The Second Bending	9.563	1.82
The Third Bending	20.688	3.05
The First Torsion	31.125	3.19

### 3 . GUST GENERATOR DESIGN

#### 3.1 General Requirement

In wind tunnel test, a specialized device called gust generator is required to induce a transverse turbulence. The general specification for the gust generator is as follows:

- 1) Generate a turbulent flow field around the test section where the model is located;
- 2) The velocity of the gust should cover the pertinent range;
- 3) The gradient length of the gust should satisfy the regulation requirements (CS-25.341) and cover the major structural modes.

#### 3.2 Preliminary Design

### APPENDIX A There are a few possible designs for a gust generator as discussed in . GUST RESPONSE WITH PGAD

#### A.1 PGAD Design

As introduced above, the PGAD has the same aerofoil as the wing and mounted to the wing tip by a rigid shaft and a torsion spring. Based on a previous study [92], shaft location, torsion spring stiffness, mass, and CG are the key parameters for PGAD design to alleviate the gust response. The initial values of parameters for the PGAD are shown in Table A-1.

**Table A-1 PGAD key design parameters for single wing**

	Span (m)	Mass (kg)	CG (% of local chord from LE)	Shaft location (% of local chord from LE)	Spring stiffness (Nm/rad)
Initial value	2	82	44.7%	15%	5.8E4

The PGAD mass and CG had been investigated in a previous parametric study [98]. To quantify the effect of PGAD spring stiffness, the study was carried out with the stiffness altered in a range of 0.1 to 10 times of initial value, CG shifted from 10% to 70%, and the mass changed between 1 and 3 times of initial value. The results indicated that the more flexible the spring, the better the gust alleviation. The mass and CG had less influence on the gust response but would affect the flutter characteristics. For this case, the mass should be less than twice of the initial design and the CG should be ahead of the mid chord.

The torsion spring stiffness was designed to restrict the PGAD rotation angle within 10 degrees to prevent stall. To minimize the interaction between wing and PGAD, the interface is set to run parallel to the air stream. Accordingly the shaft should be normal to the interface to make sure the PGAD can rotate freely. The shaft location 'a', which is defined in Equation (A-1) and Figure A-1, and the torsion spring stiffness (GJ) were taken as independent design variables. In the FE modelling, the shaft and torsion spring are modelled by using spring elements.

$$a = \frac{x_s - x_m}{b_l/2} \quad (\text{A-1})$$

where,

$x_s$  is the shaft x-axis location in global coordinate system;

$x_m$  is the local mid-chord point in global x-axis coordinate;

$b_l$  is the local chord length

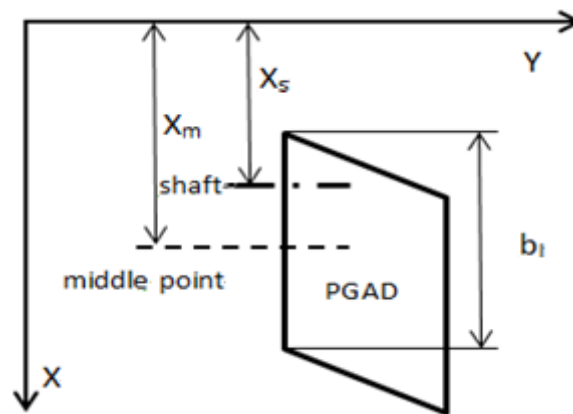


**Figure A-1 Definition of parameter ‘a’ related variables**

Further investigation on PGAD shaft location was implemented in the following section.

**A.2 Gust Response Analysis**

The gust response analysis is presented in four parts: a) First, the analysis was implemented with the aircraft restricted at the centre line which in this case is the same as wing root because of the flying-wing configuration. b) Then the aircraft was set free in Z direction to take the heave motion effect into account. c) Next, after trimming the aircraft longitudinally, the investigation was extended to involve both heave and pitching mode by releasing the translational DoF in Z direction ( $U_z$ ) and rotational DoF in Y direction ( $R_y$ ). d) Finally, further response investigation with an actively controlled device was carried out for better comparison and evaluation.

The All case studies took the same flight conditions of sea level, 0.3 Mach and full fuel mass (MTOM). Results of the first two parts a) and b) presented in last technical report FA8655-11-1-3073 were not included in this report.

**A.2.1 Response with Longitudinal Rigid Body Motion****A.2.1.1 Aircraft Trim**

Normally, an aircraft with tailless flying-wing configuration is statically unstable. Hence an elevon and active control was employed to meet the dynamic stability requirement. The following section presents an investigation into the PGAD efficiency considering the interaction between gust response and stability. Longitudinal analysis, which is relatively simple but typical and important, was involved in the current study.

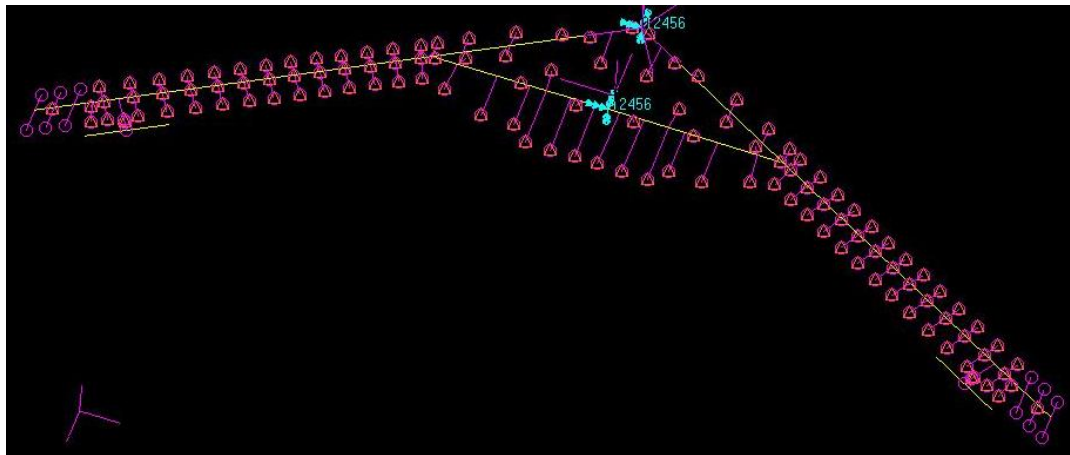


**Figure A-2 Aircraft model with PGAD and elevon**

As shown in Figure A-2, an elevon was added to the FE model to trim the aircraft to level flight condition. The elevon was modelled by rigid beam and concentrated mass (80kg) with its hinge line located at 80% of the local chord. The aerodynamic load was calculated based on the mesh shown in Figure A-3, in which the elevon surface (shown in grey) was 4,000mm span length and 780mm chord length.

Because the stiffness information about the actuator of the elevon was unavailable, an empirical value was applied to fall the rotation frequency into a practical range. The frequency needed to be high enough to avoid the coupling between the elevon rotation and wing bending, which would decrease the flutter speed significantly. According to modal analysis, the elevon rotation frequency of 30.5Hz was not involved in the undesirable coupling and was unlikely to cause aeroelastic instability problem.

The trim condition was set to 0.3 Mach with MTOM at sea level, the typical gust case. It should be noted that the engine attachment point was moved forward 4m to balance approximately the nose up moment. Without moving the engine position, the elevon would not have been able to trim the aircraft by itself even using the maximum deflection angle of  $30^\circ$ . Finally, the aircraft was trimmed at the AoA of  $-1.3^\circ$  with a small elevon deflection of  $0.17^\circ$ . The abnormal negative AoA, which was in accordance with the CFD result of  $-1^\circ$  [97], was because of the fairly high lift coefficient of the NACA4415 aerofoil ( $C_{l_0} \approx 0.5$ ).

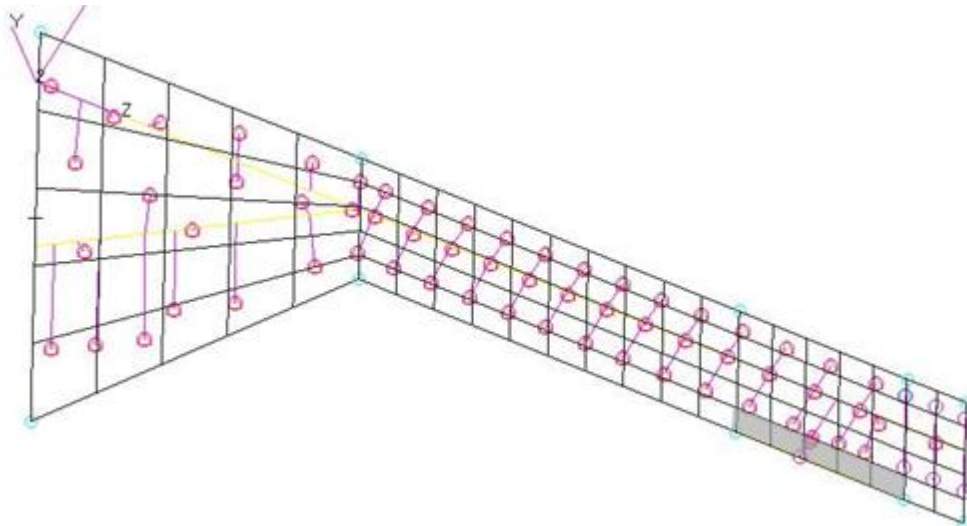
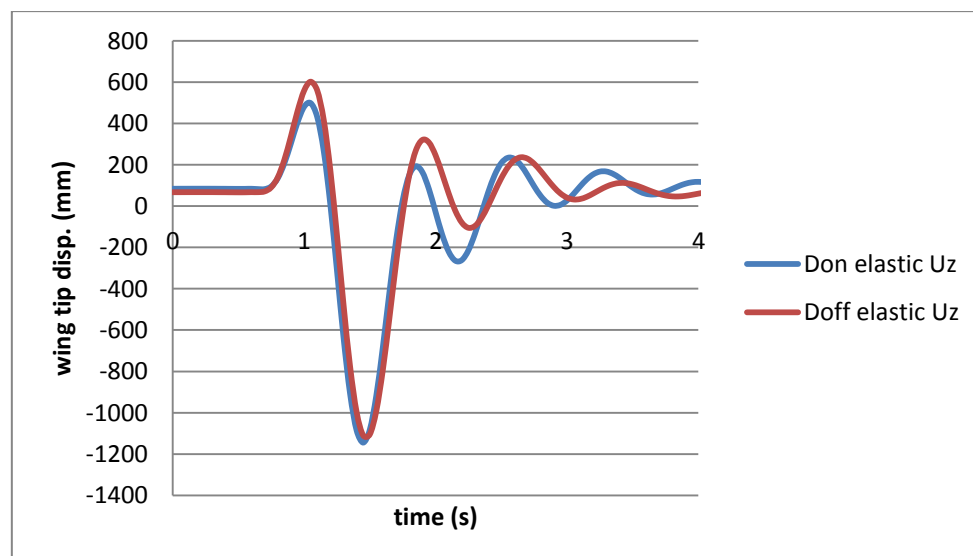


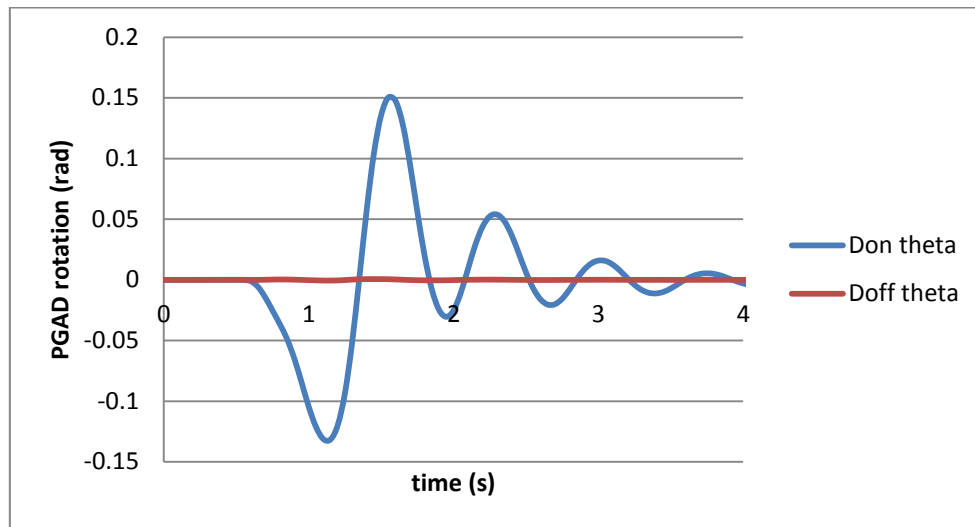
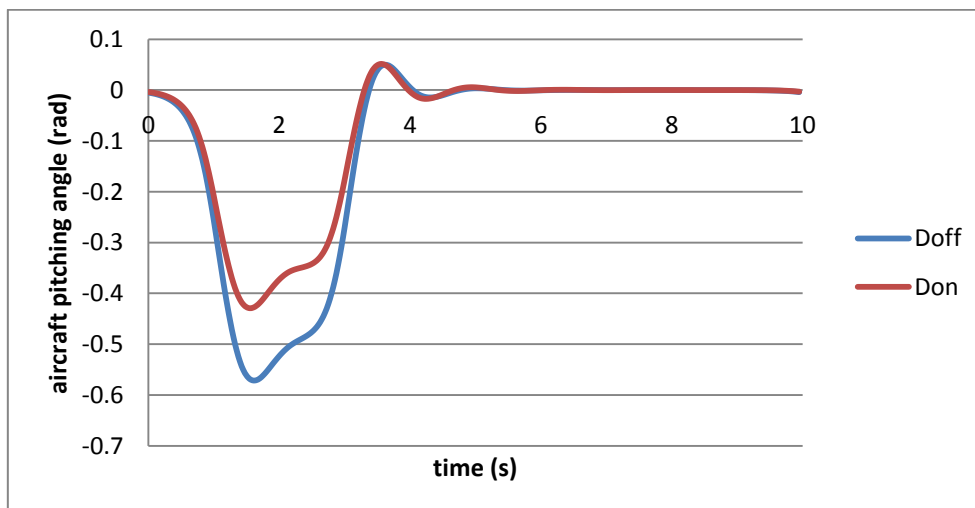
**Figure A-3 Aerodynamic mesh with PGAD and elevon**

### **A.2.1.2 Response with Heave and Pitching Motion**

Once the aircraft was trimmed longitudinally, the gust response analysis could proceed forward appropriately with both heave and pitching modes included by releasing  $U_z$  and  $R_y$ .

In this case, the gust induced wing tip deflection relative to wing root with heave and pitching motion of the aircraft is shown in Figure A-4. The PGAD passive rotation in response to the gust load is shown in Figure A-5. 'Don', and 'Doff' indicate the conditions of Device free and Device clamped respectively. As shown in Figure A-4, the 17.3% gust response reduction in terms of wing tip elastic deflection achieved with the PGAD.



**Figure A-4 Wing tip response with heave and pitching mode****Figure A-5 PGAD rotation with heave and pitching mode****Figure A-6 Aircraft pitching angle under gust**

The entire aircraft longitudinal gust response is shown in Figure A-6 represented by the pitching angle at CG. Due to the positive increment of lift and pitching moment produced by gust, the aircraft, without a flight control system, experienced a nose down pitching motion. A sufficient alleviation of this response with PGAD activated was observed from the simulation.

### A.2.2 Open Loop Active Control Case

In order to make a comparison of the passive gust alleviation with active control, a simple open loop active control of the PGAD was studied. In this case, the



wing root was clamped and the gust was set at the same frequency of 0.5Hz, and 0.8Hz respectively. An enforced deflection, with identical amplitude as passive motion of device and exactly opposite phase as gust input, was applied on the PGAD to simulate the active control case.

The response results of the wing are presented in Figure A-7~Figure A-10. Curve legend 'Don Uz', 'Doff Uz' and 'act Uz' mean the wing tip deflection in Z directions with the device on, device off and active control respectively. 'Theta' is the PGAD rotation relative to the wing tip. The angular limit to PGAD rotation was removed to give a clear picture.

In the 0.5Hz gust case, the gust response was reduced by 15.8% for the active device and 8.2% for the passive device, see Figure A-7.

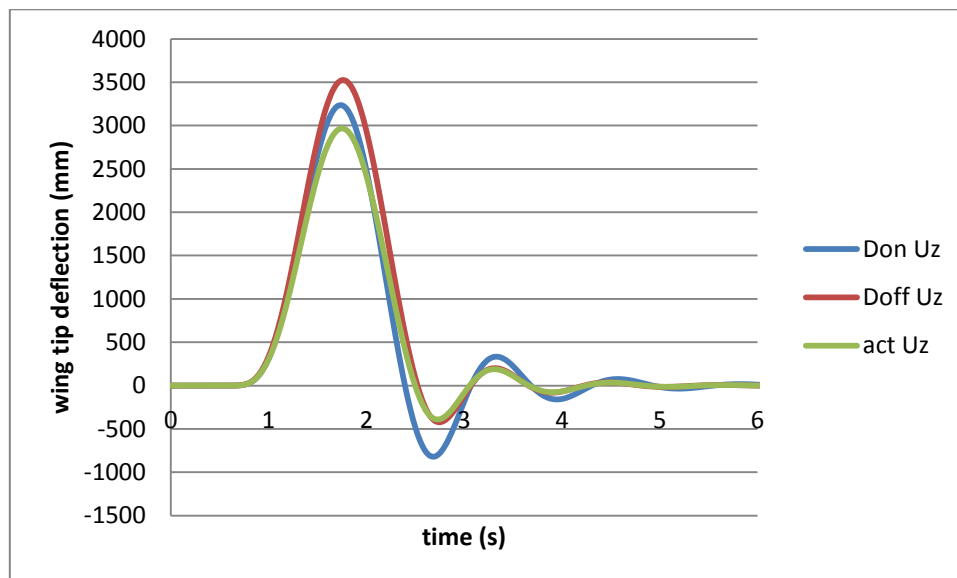
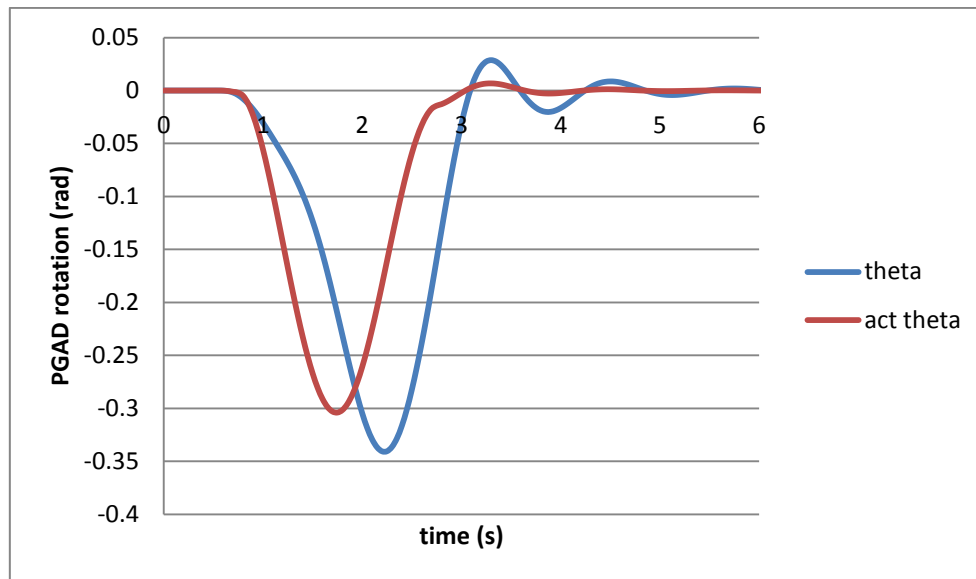
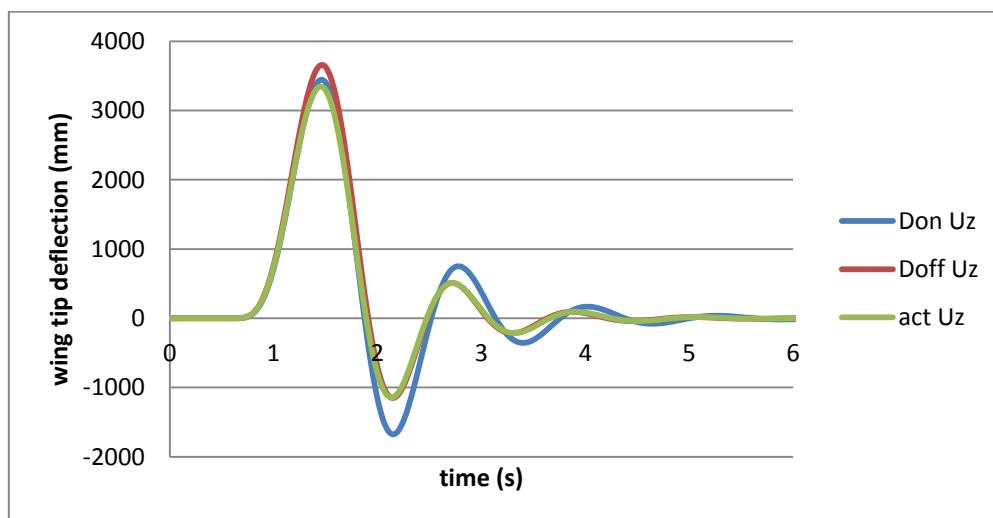


Figure A-7 Wing tip deflection in response to 0.5Hz gust



**Figure A-8 PGAD relative rotation at 0.5Hz gust**

In the 0.8Hz gust case, the reduction was 8.4% and 5.8% for active and passive device respectively, see Figure A-9. So, the active controlled device achieved more reduction in the 0.5Hz and 0.8Hz gust input. This is mainly because the specified rotation angle of the active device is larger and the phase much different from the PGAD. It can be observed in Figure A-10 that a clear phase delay of the PGAD occurs for the passive maximum nose down deflection compared with the active device.



**Figure A-9 Wing tip deflection in response to 0.8Hz gust**

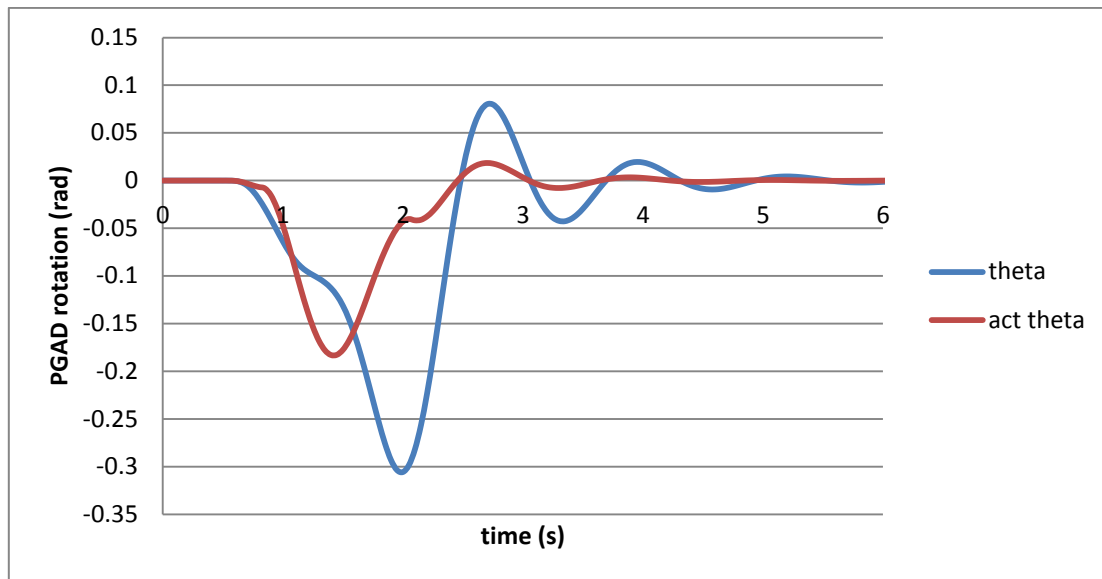


**Figure A-10 PGAD relative rotation at 0.8Hz gust**

The conclusion can be drawn that both passive and active device are effective in gust response alleviation. The efficiency is also related to the phase of deflection motion which is one of the dynamic characteristics of the rotation spring and device mode. So, phase should be another dependent design parameter for focus in the future.

. . The first option with two straight blades in front of the model was the best choice for the current study taking into account wind tunnel condition, functional requirements, and cost.

### 3.2.2 Geometry

The blades were designed as NACA0015 aerofoil with 200mm chord and 1,000mm span. Other dimensions, such as blade spacing, and test model location ( $d_x$ ,  $d_y$ ) as shown in Figure 3-1, need to be investigated by numerical simulation and by experimental test which will be discussed later.

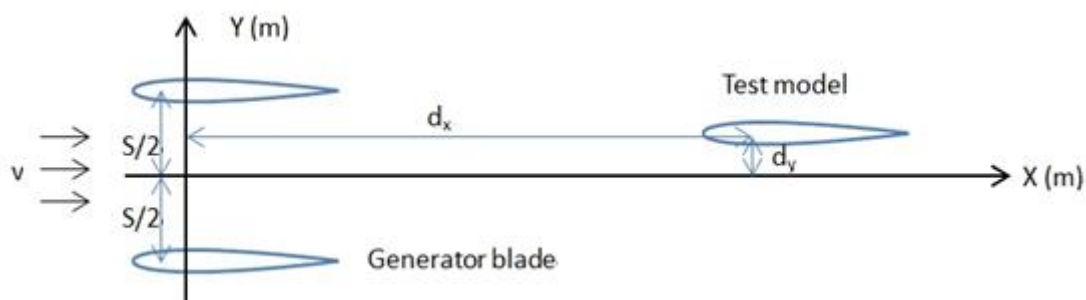
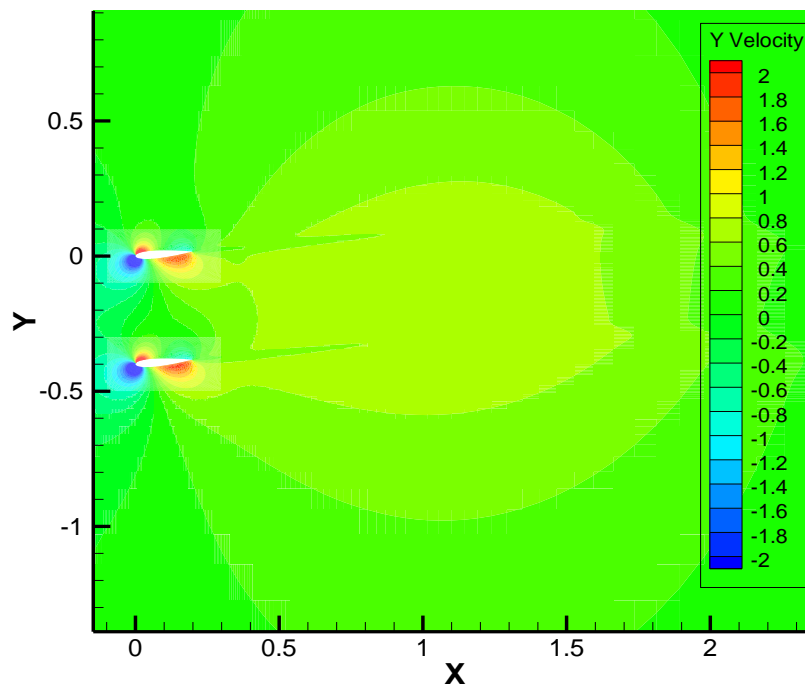


Figure 3-1 Generator configuration (top view)

### 3.2.3 Aerodynamic Analysis

A CFD simulation of the generator was conducted to evaluate the flow field around the blades and to search the appropriate location for wing model. The 2D unstructured grids were firstly generated using the Integrated Computer Engineering and Manufacturing code. The dynamic motion of the blades was simulated afterwards by User Defined Function in FLUENT to drive the dynamic mesh. Dynamic analysis was based on a combination of various cases with different blade spacing, blade maximum AoA and oscillation frequency. One result of 2D generator model was shown in Figure 1-2.



**Figure 1-2 CFD result of 2D blade model**

In the case of 11.7m/s wind speed at inlet, 2C (two times of blade chord length) blade spacing and 2Hz blade oscillation, the induced gust velocity was reduced and kept a periodical sinusoidal shape when measured at points down the central line, see Figure 1-3. Further investigation seen in Figure 1-4 shows that the bigger maximum AoA of blade led to the higher transverse gust. But, there was a distortion when the AoA reached  $25^\circ$  as illustrated in Figure 1-6. The gust velocity was higher and damping was slower when the blades oscillated at 4Hz instead of 2Hz, see Figure 1-5.

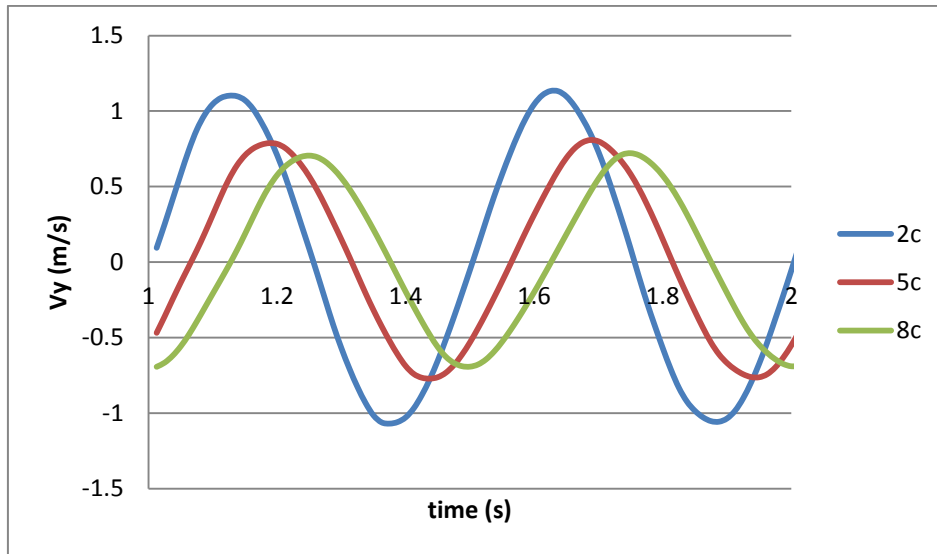


Figure 1-3 Gust speed at various location

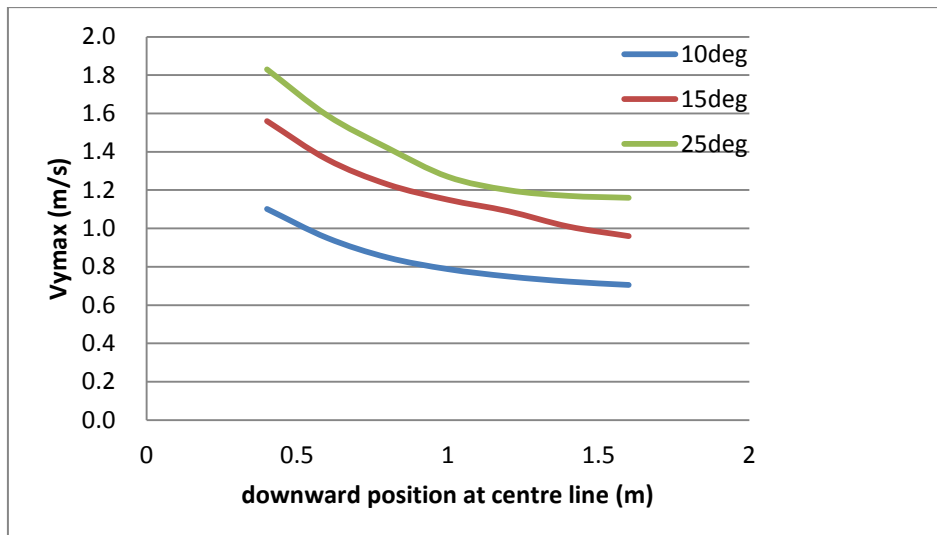


Figure 1-4 Gust velocity at different maximum AoA of blade

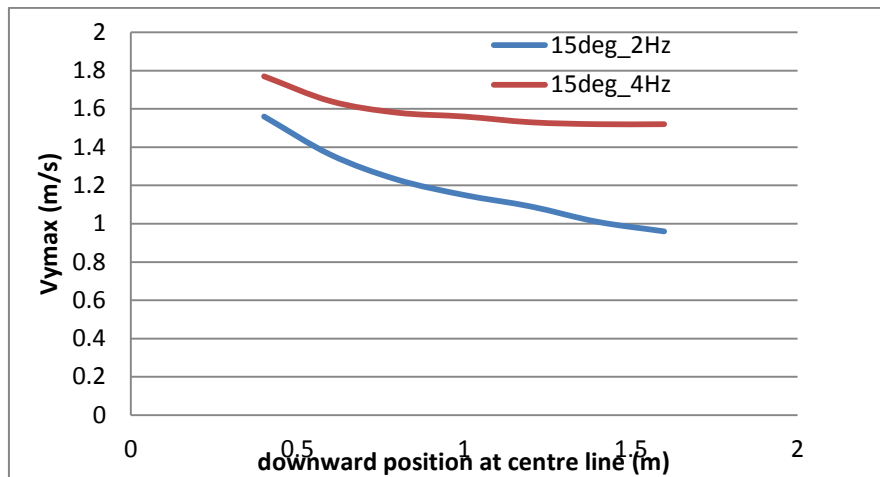


Figure 1-5 Gust velocity at different generator oscillation frequency

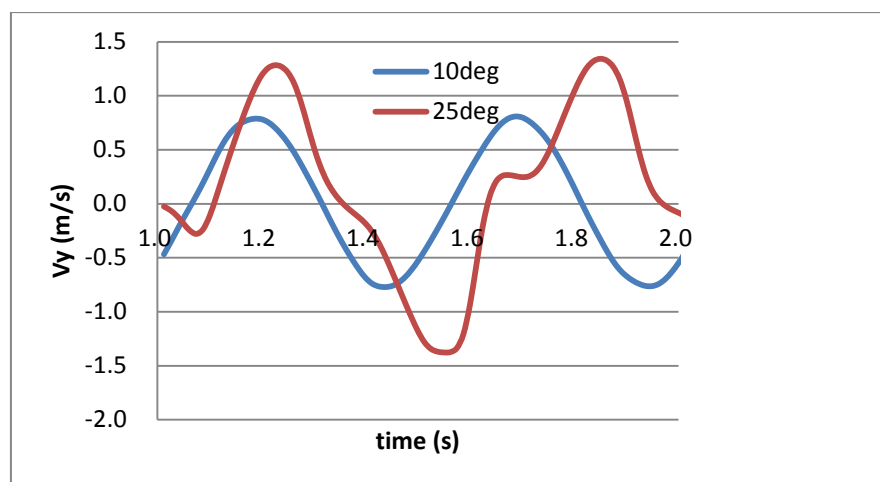


Figure 1-6 Gust time history at two different AoA (location=5C)

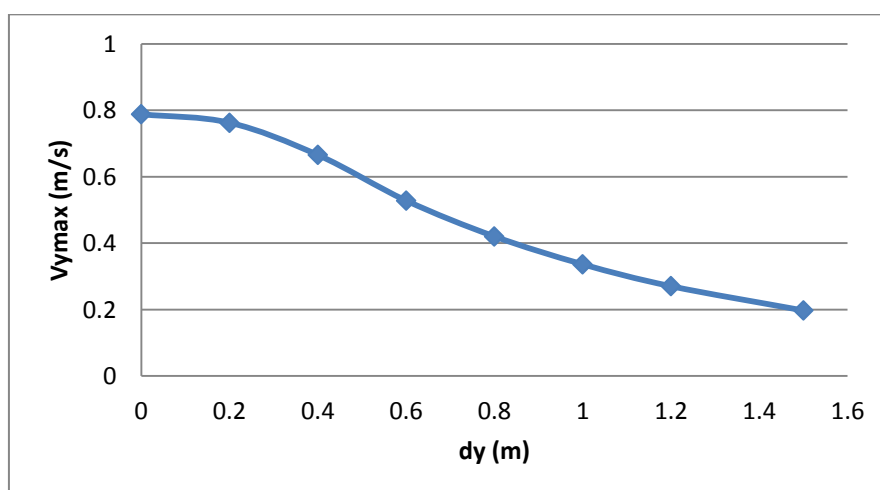


Figure 1-7 Cross section gust speed at 5C downward

As the wing model was highly flexible, it deformed away from the centre line during the test. So, the cross section flow field characteristics were investigated as well. It can be seen in Figure 1-7 that the gust intensity declined when measured outward from the centre line, but nevertheless it could be treated as quasi-steady in the adjacent field, approximately  $\pm 0.2\text{m}$ .

Figure 1-8 shows that the airflow velocity fluctuated slightly and the amplitude of the fluctuations became bigger when measured at a point further down the centre line from the gust generator. The maximum offset value was 1.3% at 8C which was acceptable for this current study.

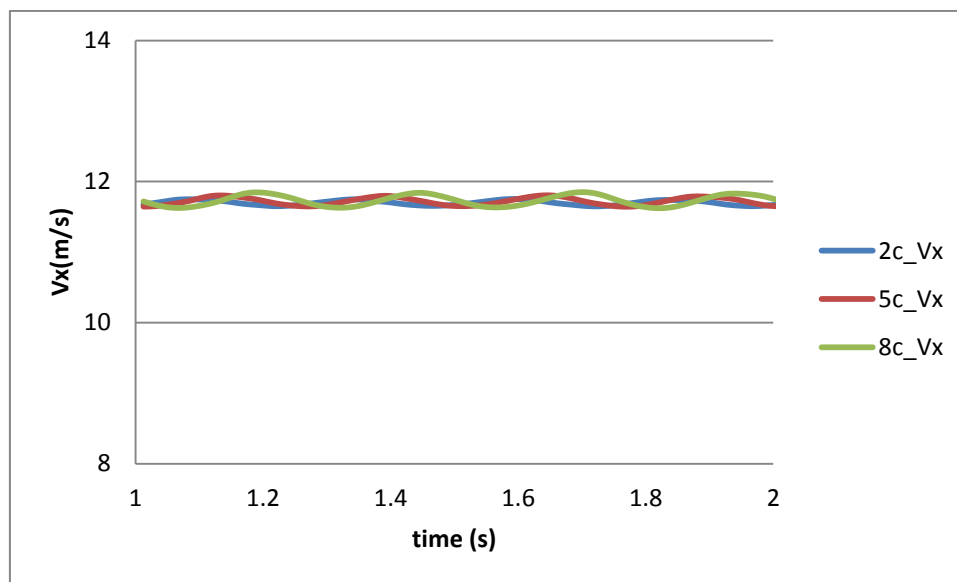


Figure 1-8 Airflow velocity fluctuation downwind from the gust generator

### 3.2.4 Mechanism

#### 3.2.4.1 Motor Selection

The first concern in motor selection was to make sure that the proposed motor was powerful enough to drive the system at the worst load case of the generator.

Since the NACA0015 aerofoil was symmetric and the shaft was located at 25% chordwise, in theory there should be no pitching moment due to aerodynamic



load applied to the system. So, only inertia load and friction were taken in consideration.

The maximum torque required for driving the blades could be obtained following equation (1-1).

$$T_{max} = J\ddot{\theta} \quad (1-1)$$

where,  $J$  is the moment of inertia;

$\ddot{\theta}$  is the second order derivative of the rotation angle of the blade.

In this test, for a single straight blade with 1m span and 0.2m chord, the moment of inertia was  $0.0042\text{kgm}^2$  relative to the current rotational axis which was at 25% of the aerodynamic centre line. In the case of  $10^\circ$  maximum rotation angle and 5Hz maximum frequency, the torque required was 1.45Nm.

An all-in-one brushless DC servomotor was chosen as the power unit for the generator based on the above estimation.

#### 3.2.4.2 Kinematical Simulation

The two blades were driven synchronously by the DC servomotor. A demo model shown in Figure 1-9 was built to demonstrate the mechanism operation. There were two slide blocks in this system to transfer circular motion to linear reciprocation and then back to rotation. An accurate simulation can be obtained with this design but the efficiency depends on the friction factor of the slide movement. The manufacturing cost will increase due to the high specification for the surface finish of the slides and their guide tracks.

Finally, a four-bar linkage system was used as the mechanism to drive the gust generator as shown in Figure 1-10.

The appropriate value for the design parameters was determined and demonstrated by kinematical simulation using the CATIA DMU module due to its excellent 3D modelling capability and friendly data export interface.

The blade fixed on bar 3 was driven by bar 1 (green) of mechanism model as shown in Figure 1-11. In Figure 1-11 (b), the tracks of blade at the leading edge and the trailing edge in a whole cycle are represented by white curves with cross marks. The maximum rotation angle of blade reached  $20^\circ$ , see Figure 1-12. Also it can be seen that when a constant 120 rpm was applied to the driving bar, over time angular movement at the revolute joint followed closely the standard sinusoidal curve expected.

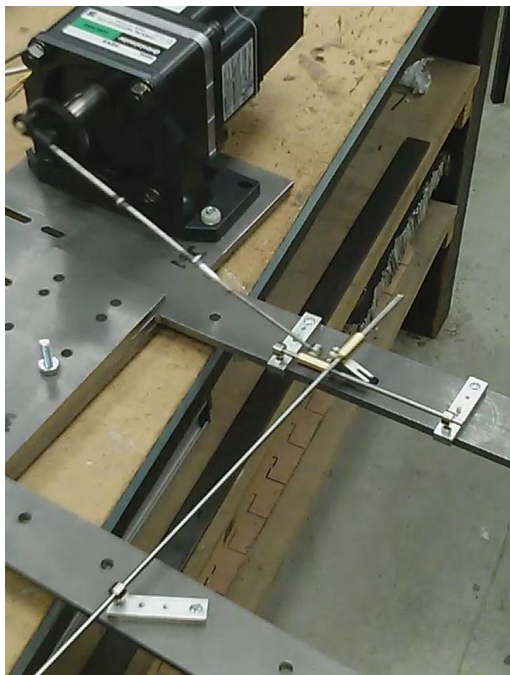


**Figure 1-9 Demo mechanism**

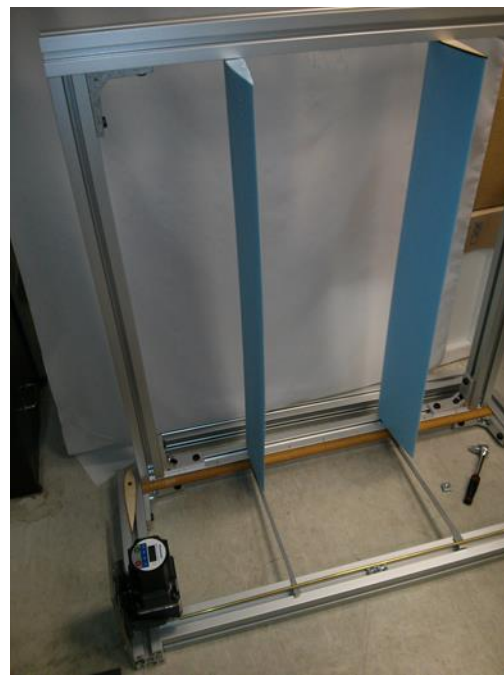


**Figure 1-10 Assembled generator**

The other blade could easily be added to the system driven by a rigid bar with the same length as the distance of axes between the two blades to keep their motion synchronous.

As the aerofoil of the blade had already been decided, the aerodynamic load could be acquired. For static case, the experimental and theoretical lift coefficients were 0.91 and 1.09 respectively at  $10^\circ$  maximum rotation angle (equivalent to AoA) [105]. The value would increase slightly to 1.2 if unsteady effect were considered. So, the maximum load on a single blade was 18.4N

approximately and this value was used as the reference load while designing the mechanism.

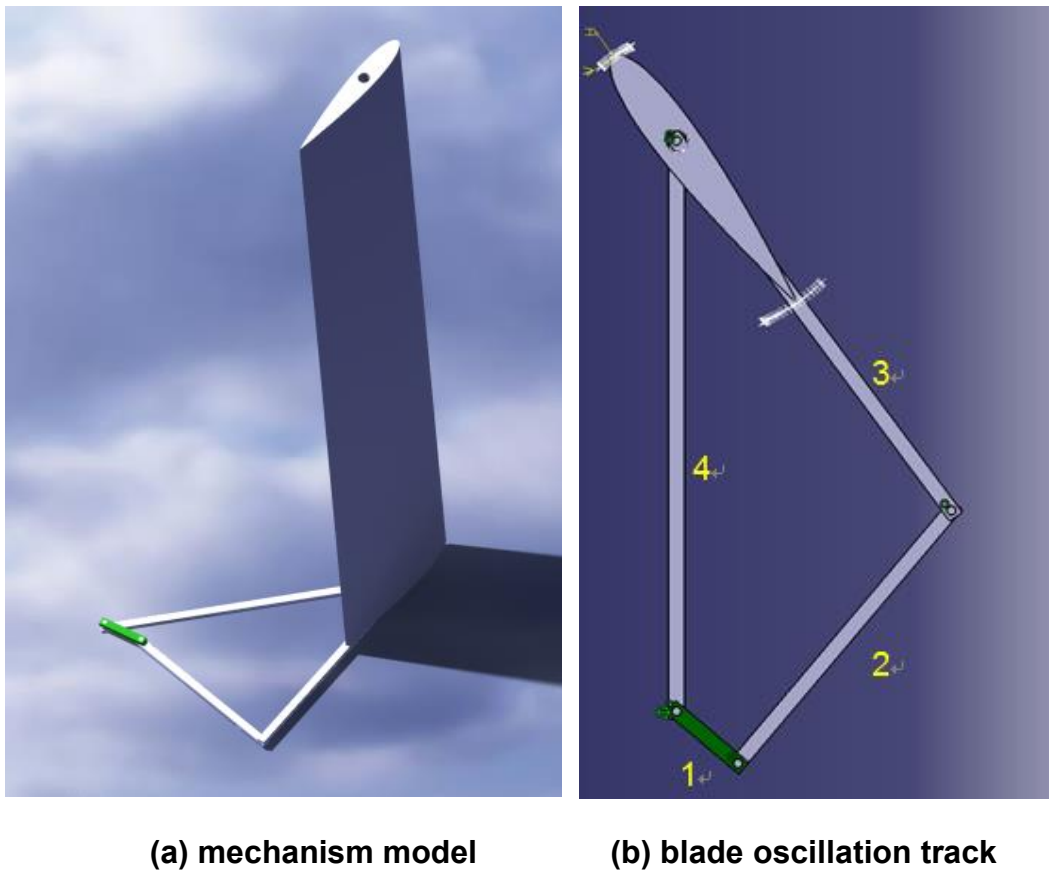


Figure 1-11 Mechanism simulation

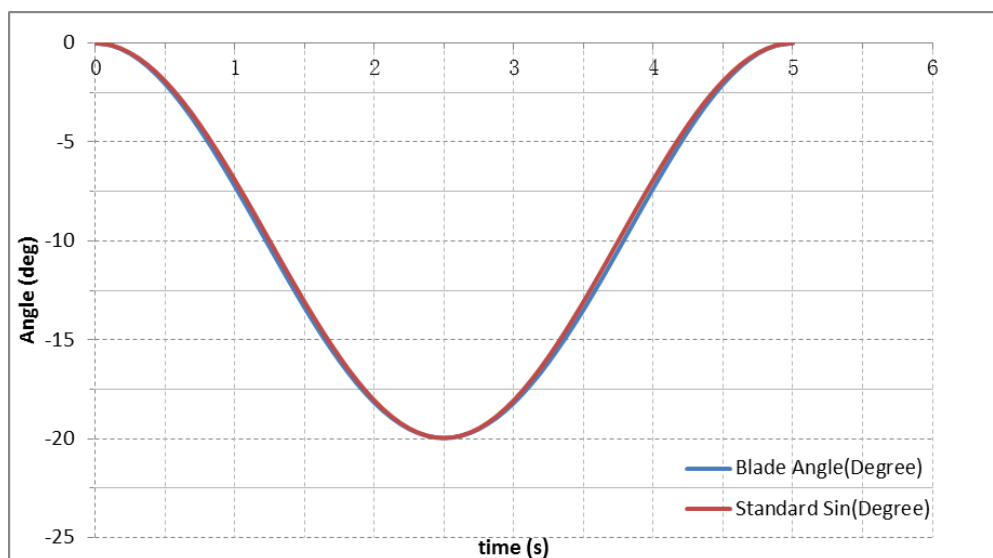


Figure 1-12 Contrast of movement track

### 3.3 Manufacture

The generator was composed of blades, supporting frame, mechanism, and power unit. The assembled gust generator is shown in Figure 1-10.

The supporting frame was built of 60x60 aluminium extrusion. The power unit was an off-the-shelf brushless DC servomotor with build-in gearhead and controller (model BLA550CB-5 from Oriental Motor (UK) Ltd). Rectangular cross-section aluminium beams and ball bearings were used to construct the mechanism.

The blades were made of high density modelling foam, which was shaped as a NACA0015 aerofoil following the same procedure as in wing manufacture. They were reinforced by a brass tube through the 25% chordwise axis, and were covered with shrinkable tissue.

### 3.4 Load Free Functional Test

Once assembled, the gust generator was tested to check if all the designed functions were achieved before operation in the wind tunnel. It had run for 10mins at 1Hz, 2Hz, and 5Hz respectively. The same procedure was repeated at the different maximum rotation angles. During all the test cases, the whole system worked well without sticking unexpectedly or structural failure.

## 4 WIND TURNNEL TEST OF THE SCALED WING MODEL

### 4.1 Test Plan and Preparation

First of all, an executable plan including two main parts was worked out for the wind tunnel test of the half span HAR wing 1:25 scaled model with PGAD. In part one, after checking the functionality of the gust generator, the flow field characteristics in the test section were investigated to make the final decision on test condition. In part two, dynamic response test was performed at optimal test position determined from the last study in different cases.

The entire experiment was conducted in a 5x4 wind tunnel at University of Hertfordshire. The open circuit tunnel is a low speed facility with 20m/s maximum. Appropriate hardware and software were chosen to enable measurement of required parameters, signal acquisition and data pre-processing. Once selected, all the instruments had to be checked to make sure they functioned well and were within a valid calibration cycle.

#### 4.1.1 Instrument Requirement

A Universal Serial Bus (USB) based data acquisition system was built up to meet the requirements of the wind tunnel test as shown in Figure 4-1. All channels were synchronized by a trigger signal as some of them were acquired through different ports with their own software.

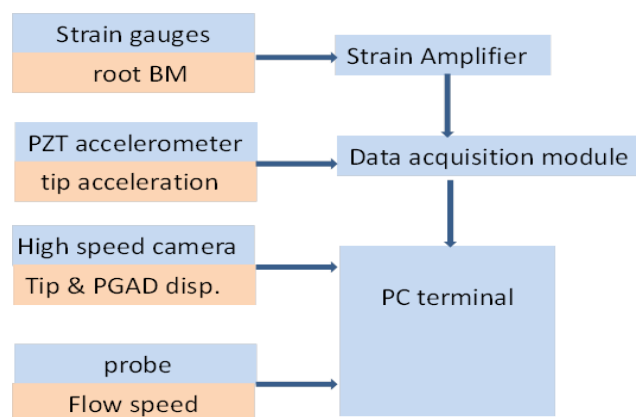


**Figure 4-1 Data acquisition system configuration**

The instruments used in the current experiment are listed in Table 4-1.

**Table 4-1 Instrument list**

Instrument	Model	Sensitivity	Amount	SN
Strain Amplifier	YE3842A	/	2	8520146/7
Acquisition module	NI9234	/		2713
Strain gauge	RS-N11MA512011	7 V/ $\epsilon$ (bridge)	8	/
Accelerometer	Dytran 3224A1	10.24mV/g	1	372
Impulse hammer	Dytran 5800B2	92.20mV/lb.F	1	5547
Servomotor	BLA550CB-GV	/	1	/

#### 4.1.2 Test Setting Up

The gust generator was mounted in upstream of the test section about 1 meter in from the tunnel inlet where flow is relatively steady, see Figure 4-2. The ceiling probe was installed as reference in the vertical symmetrical plane of the generator blades and 400mm down from the ceiling to avoid any effect from the tunnel wall. The 4-hole probe set was mounted on a 3D portable frame to move to each test point location as required.

The formal test was executed in two parts according to how the model was installed. In one test it was fixed vertically as seen in Figure 4-2 using the outer wing only due to the limitation imposed by the tunnel height. In this case, the response was purely gust induced as the generator support and tunnel wall effect could be ignored.

The other test, the wing was installed horizontally as seen in Figure 4-3 and Figure 4-4. The effect of gravity on the structure and initial deflection had to be considered during test setting up and post data processing.

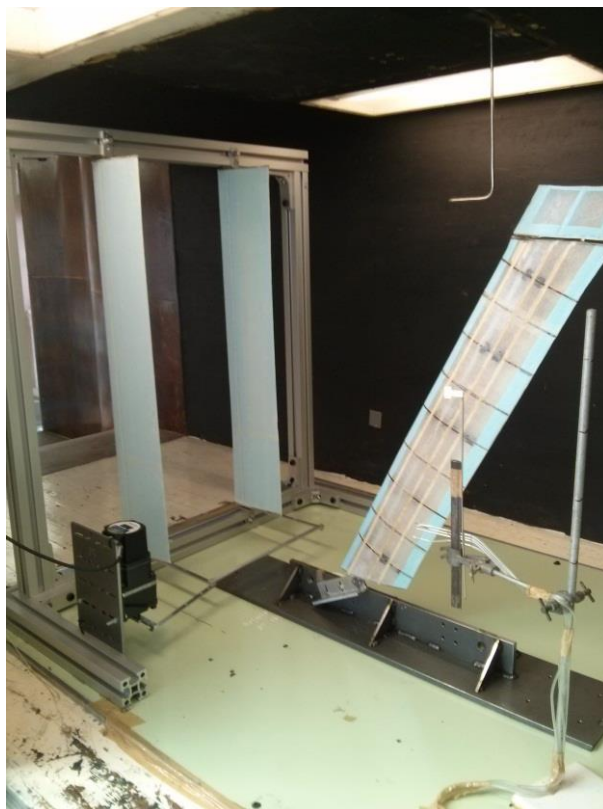


Figure 4-2 Outer wing test side view



Figure 4-3 Whole wing test front view





**Figure 4-4 Whole wing test rear view**

#### **4.1.3 Pre-test Load Calibration**

Once the horizontal test configuration had been determined, the strain gauge was calibrated to work out the force and moment applied to the wing structure. It was difficult to perform an accurate dynamic strain calibration to match the real test case. Since the operational frequency around 2Hz was relatively low, it was believed that an alternative quasi-static calibration would be acceptable without many errors.

A single point load was applied at the joint between the wing tip and the PGAD. The force-strain relationships of the front and rear spars are presented in Figure 4-5 and Figure 4-6 respectively.



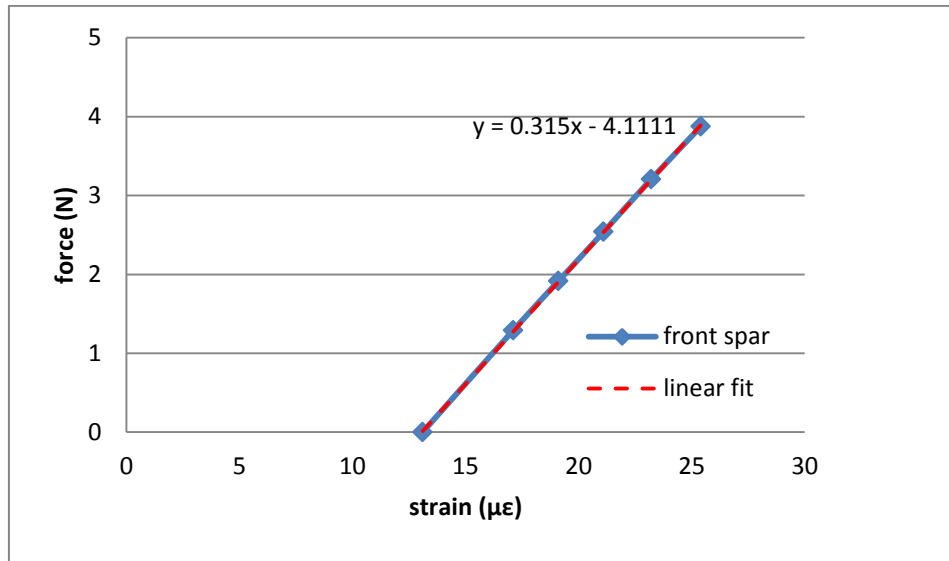


**Figure 4-5 Front spar force-strain calibration curve**

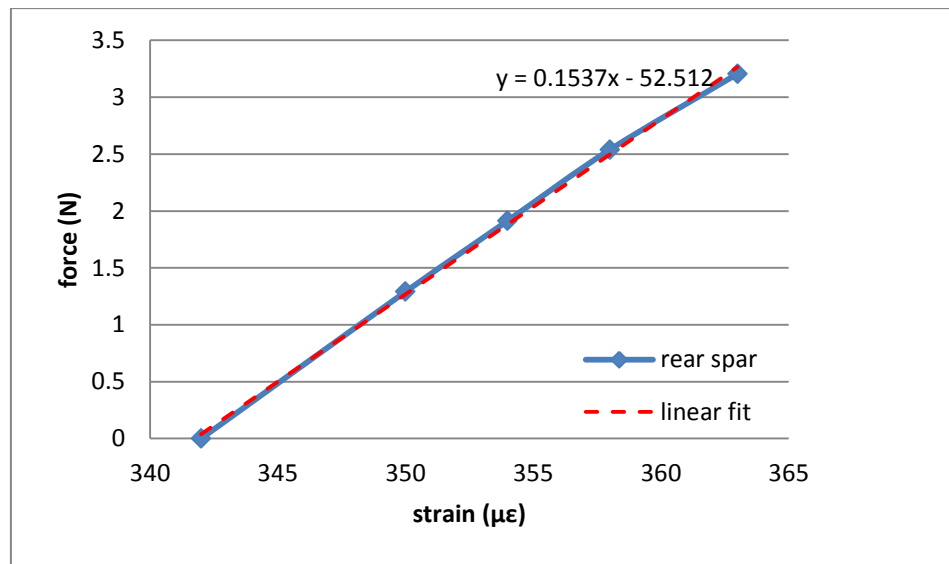


**Figure 4-6 Rear spar force-strain calibration curve**

Strain- deflection curves are shown in Figure 4-7 and Figure 4-8. A dashed red line added in each figure gives the linear fit and shows that all strain- deflection curves were almost linear. So, the deflection of wing structure remained in the linear elastic range under the calibration loads.

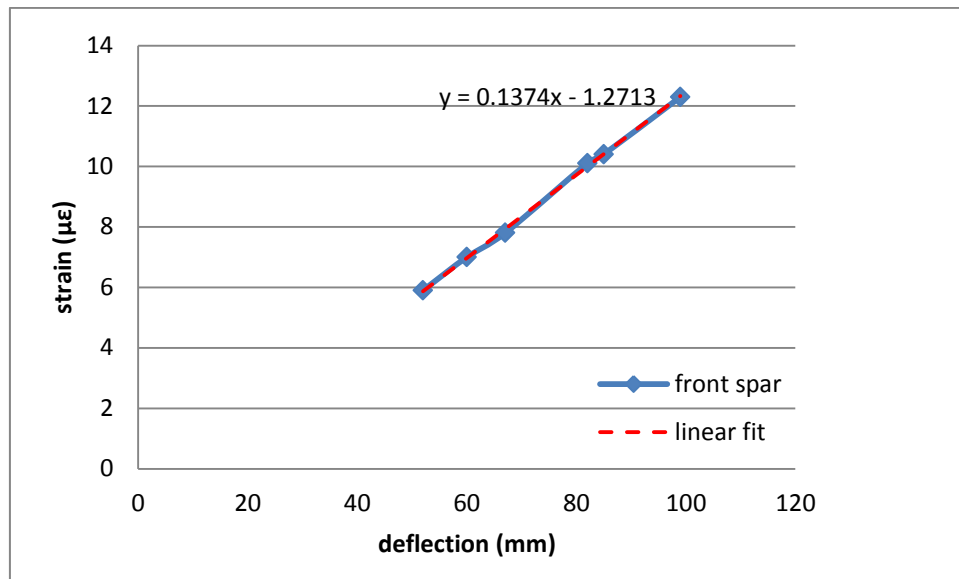


**Figure 4-7 Front spar strain- deflection curve**

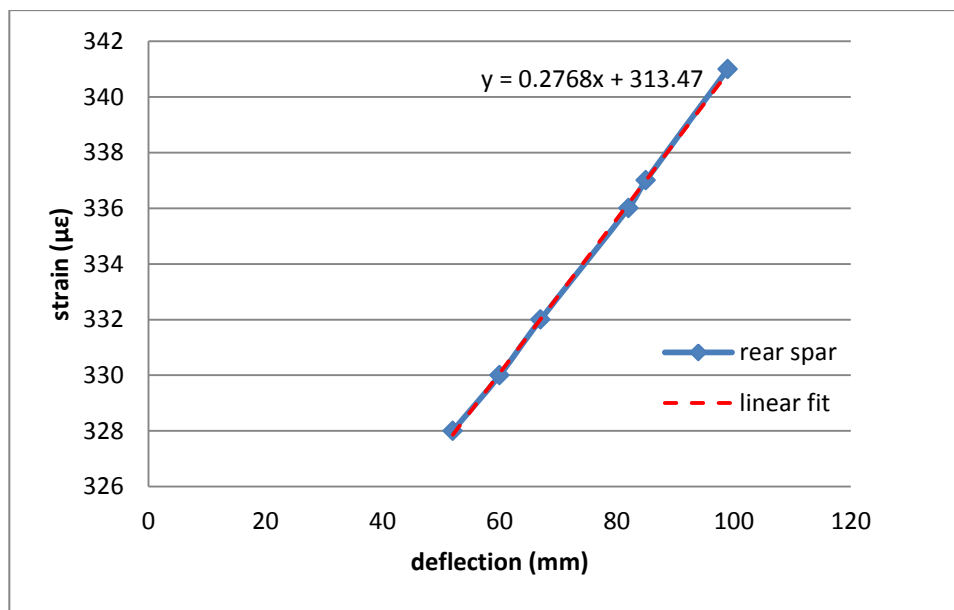


**Figure 4-8 Rear spar strain- deflection curve**

A digital simulation by static analysis in NASTRAN was done as well. The result showed that the maximum deflection of wing tip under the same load case in simulation was 105mm compared to a measured value of 102mm. This indicates that the physical test model was accurate enough to represent the design and the calibrated results could be used to acquire further non-directly measured parameters.

## 4.2 Experimental Validation of Gust Flow Field

Based on CFD simulation, the turbulent field depends on several independent parameters: air flow speed, blade pitch, blade AoA, blade rotational frequency, test point location. In this study, some of the parameters defined as shown in Figure 4-9 could be specified by their individual reasonable working condition and are listed in Table 4-2.

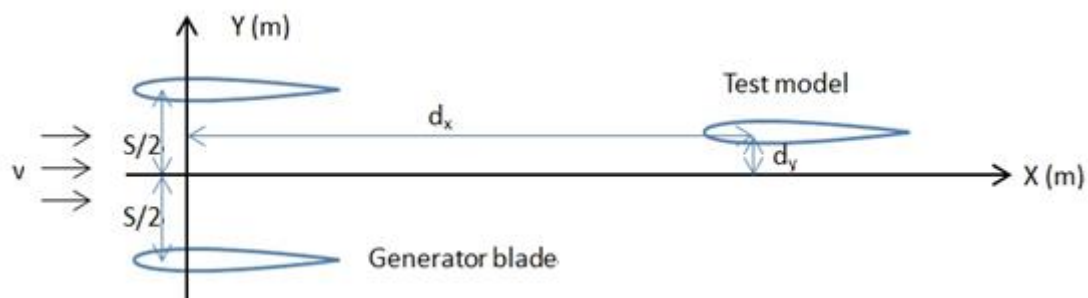


**Figure 4-9 Parameter definition (top view)**

**Table 4-2 Validation test case matrix**

	Symbol	Unit	Range	Isolated test point
Air speed	V	m/s		5,10,11.7
Blade pitch	s	m	0.3~0.6	0.3, 0.4, 0.5
Blade AoA	$\alpha$	$^{\circ}$	0~10	5, 10, 15
Blade rotational Frequency	f	Hz	0~5	1, 2, 3, 5
test point location X	dx	m	0~2	0.6, 1.0, 1.6
test point location Y	dy	m	-0.4~0.4	-0.5, -0.3, 0, 0.3, 0.5

### 4.2.1 Calibration of Gust Velocity

It was important to validate and calibrate the method for measuring gust velocity before all formal tests. The measurement principle of Pitot probes discussed above is shown in Figure 4-10 and their relationship is expressed as Equation (4-1). The data acquired from the ceiling probe acted as a reference and as a backup signal resource as well.

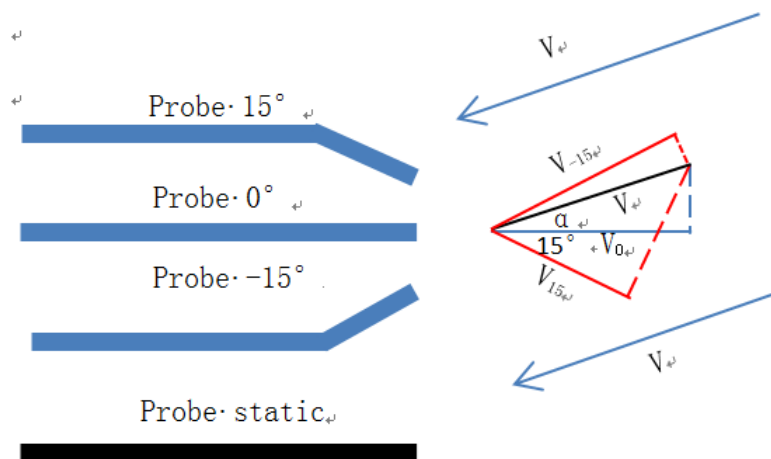


**Figure 4-10 Air speed measurement illustration**

$$\begin{aligned}
 P_0 &= \frac{1}{2} \rho v_0^2 + P_s \\
 P_{15} &= \frac{1}{2} \rho v_{15}^2 + P_s \\
 P_{-15} &= \frac{1}{2} \rho v_{-15}^2 + P_s \\
 v_0 &= v \cos \alpha \\
 v_{15} &= v \cos(\alpha + 15^\circ) \\
 v_{-15} &= v \cos(\alpha - 15^\circ)
 \end{aligned}
 \tag{4-1}$$

where,

$P_0$  is the total pressure of  $0^\circ$  direction;

$P_{15}$  is the total pressure of  $15^\circ$  direction;

$P_{-15}$  is the total pressure of  $-15^\circ$  direction

$v_0$ ,  $v_{15}$ , and  $v_{-15}$  have the same meaning of velocity in each direction and all of them are treated as a decomposed vector of the real wind speed in their own direction.

The angle  $\alpha$  between  $v$  and  $v_0$  can be worked out and therefore gave the gust velocity. Based on the above method, the angle of attack could easily be read from Figure 4-11, a contrast curve with four order polynomial fit between  $\pm 30^\circ$  which is believed to be wide enough to cover the required range. Although the

dynamic pressure ratios of any two directions could be used,  $P_{15}/P_{-15}$  should be the best choice which was more accurate as the symmetrical characteristics cancelled out some of the system errors.

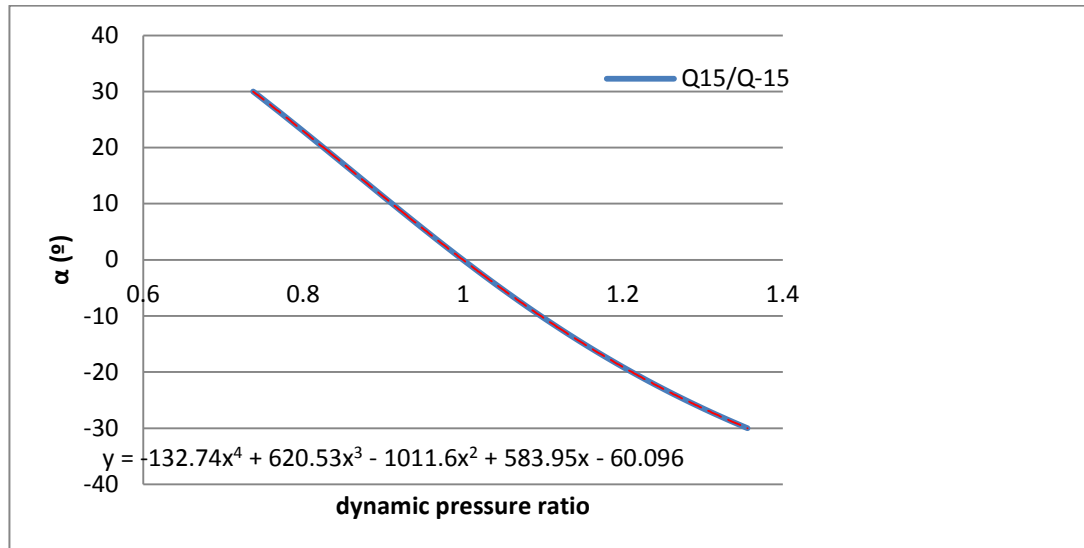


**Figure 4-11 AoA versus dynamic pressure ratio**

A comparison of the gust velocity obtained from CFD simulation and wind tunnel test in downstream of the gust generator is shown in Figure 4-12 and Figure 4-13. The gust generator was operated at 2Hz with maximum 15° blade deflection in 10m/s airflow field. The gust velocity was measured from the centre in dy-direction normal to the streamline as shown in Figure 4-9. As shown in Figure 4-12, all the measured data were slightly smaller than the CFD simulation and the result deviation between the two methods increased as the measurement point dy increased from the centre line. For example, the deviation increased from 3.8% at the centre line to maximum 10.2% at dy=0.4m. For the gust generator in symmetrical layout, the maximum gust velocity was at the centreline with 20% loss at both sides mainly due to the wind tunnel wall boundary effect. For the cantilever model mounted on one side of the wall, the wall effect was minimum.

For gust velocity in streamwise, data was measured at points 0.6m, 1.0m and 1.6m in the downstream field along the centreline. As shown in Figure 4-13, the test data and the CFD simulation have better agreement with maximum

deviation 6.5% at the location of 0.6m. The gust velocity became steadier after 1.5m downstream. For the model wing of 30° sweep angle, it was preferable to set the model within this zone.

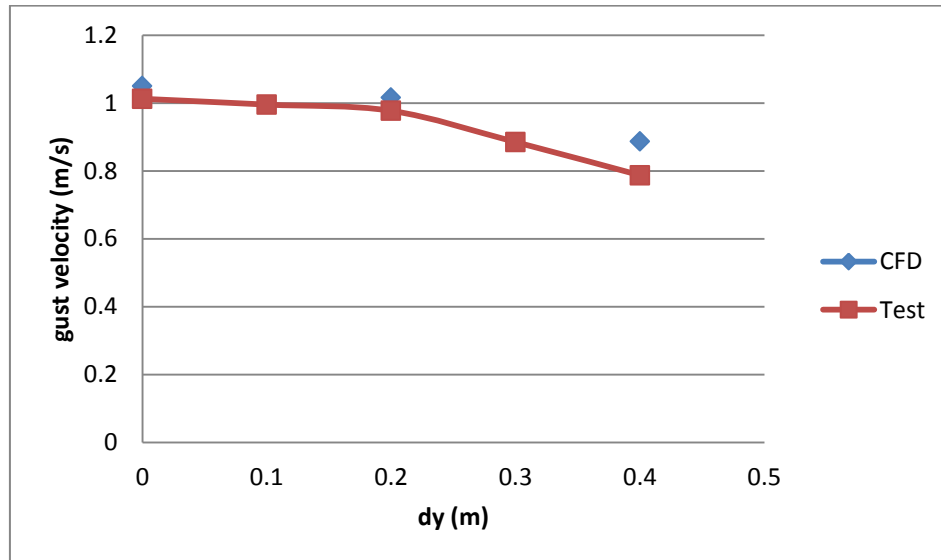


Figure 4-12 Cross section gust velocity comparison

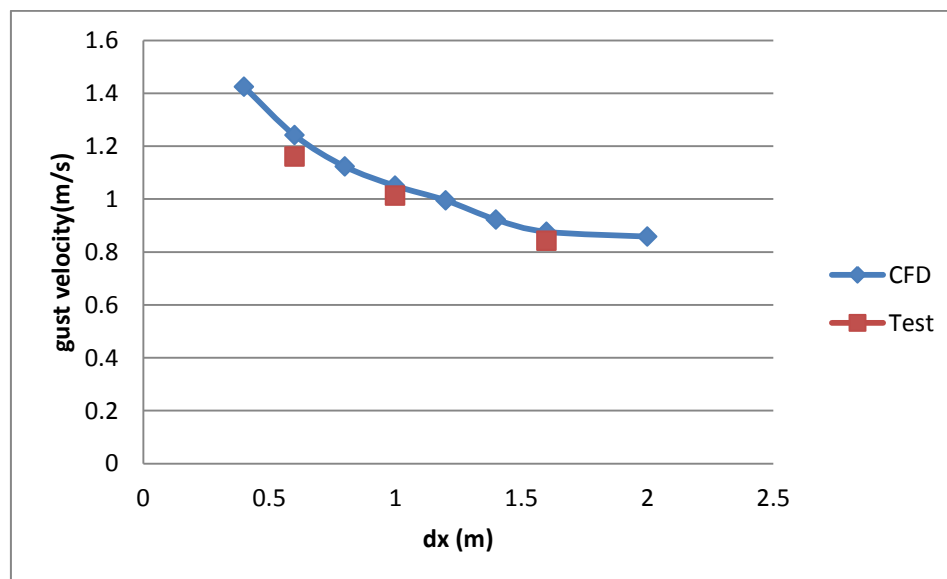


Figure 4-13 Streamwise gust velocity comparison

#### 4.2.2 Test Results of Flow Field

A typical result is shown in Figure 4-14 at 11.7m/s air speed and 10° maximum AoA of the blade. Triangle, square and diamond marks were used to represent

the relative AoA of the wing in the gust field at 0.6m/3C (3 times mean chord), 1.0m/5C and 1.6m/8C respectively (see Equation (4-2)). One set of data at 0.3m cross direction was lost during data transfer.

$$\text{AoA} = \tan^{-1}(v_{\text{gust}}/v_0) \quad (4-2)$$

A low pass digital filter with upper frequency at 2.5Hz was applied in post data processing to eliminate the noise introduced in measurement. The trend makes a well agreement with the simulation results.

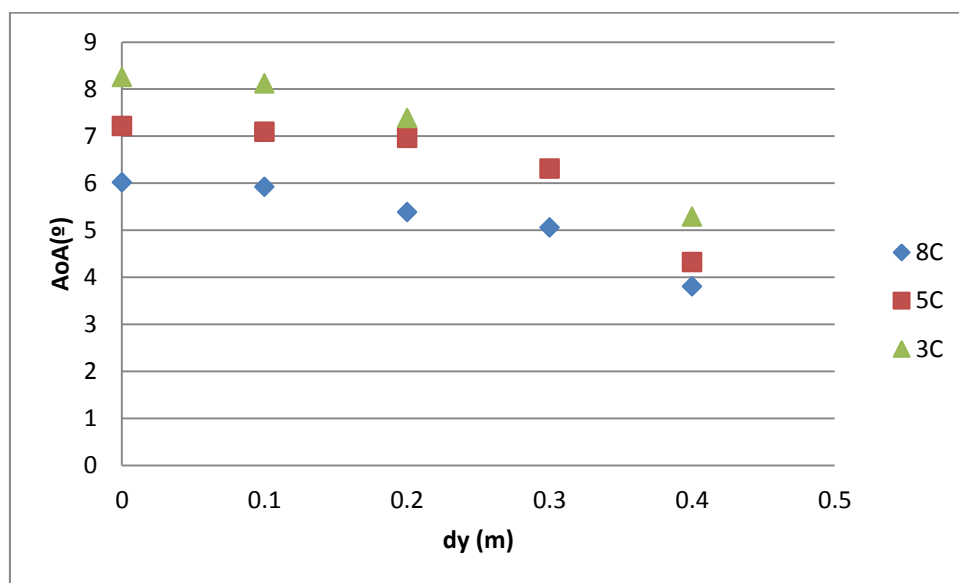


Figure 4-14 Gust flow field calibration at 11.7m/s wind speed

## 4.3 Gust Alleviation Test

### 4.3.1 Vertical Fixed Outer Wing Test

The only reason for doing the test with vertical installation was to keep the response as simple as possible in order to find out the effective parameters and to discover and solve some problems which might lead to failure or unexpected errors. So, a few typical cases were tested instead of the whole case matrix.

Figure 4-15 shows the interface of the software called 'tracker', which was used to deal with the post processing of the high-speed-camera data. The results as

seen in Figure 4-16 show that with PGAD enabled, the wing tip deflection reduced clearly at 8m/s wind speed and 2Hz gust.

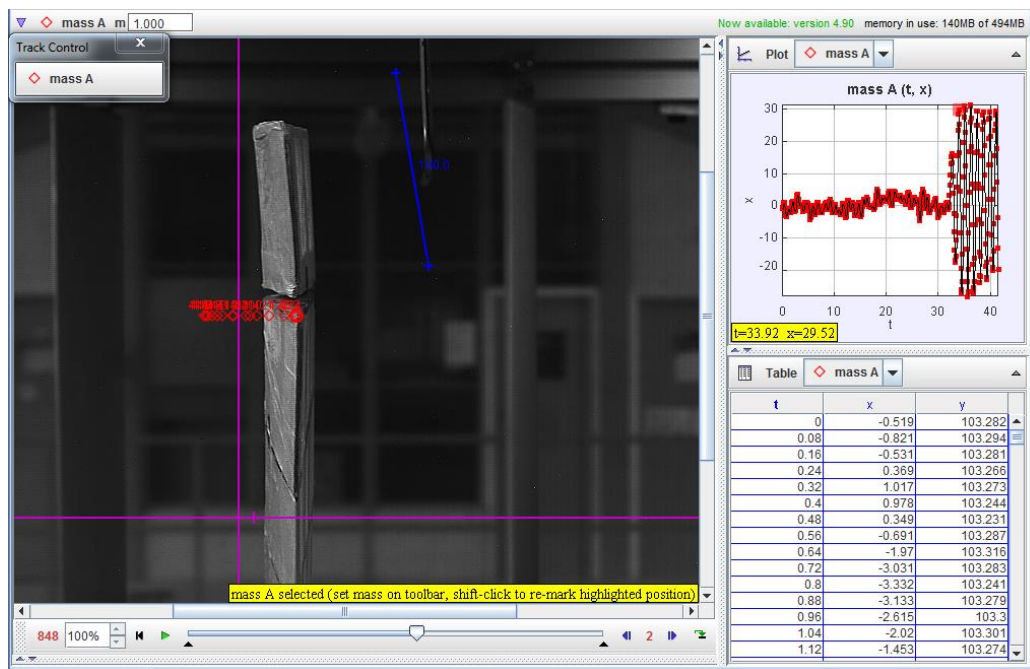


Figure 4-15 Post process of high speed camera data

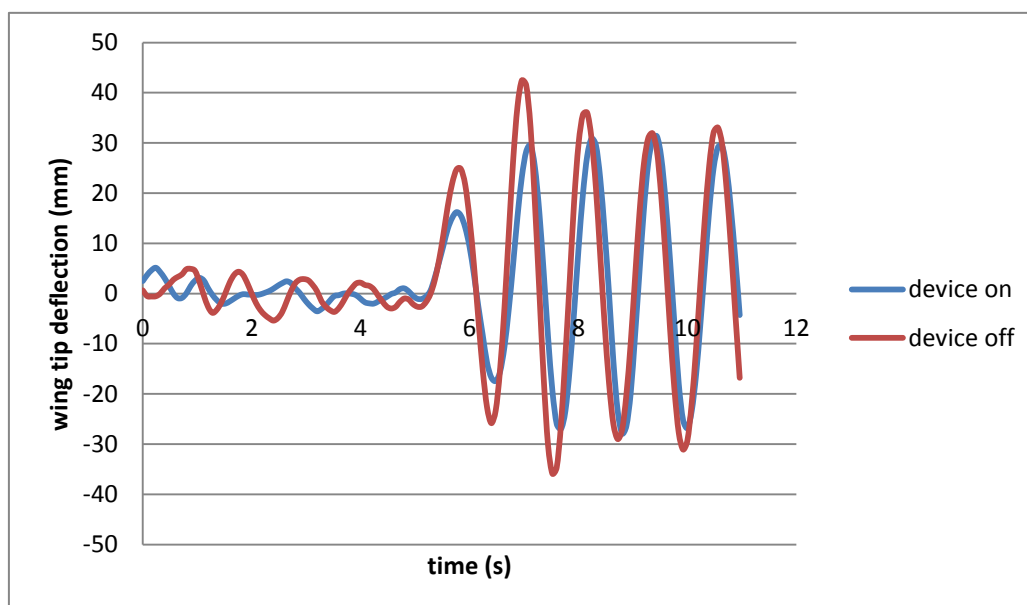


Figure 4-16 Gust response of vertical fixed wing



### 4.3.2 Horizontal Fixed Whole Wing Test

A half span wing model response test was conducted with the model fixed at the ideal location found in the above study.

The dynamic response of the wing was measured in different cases with and without the PGAD activated. The major parameters chosen to represent the response were: wing tip deflection and acceleration in out-of-plane direction, relative rotational angle of the PGAD, and wing root bending moment. Those parameters were measured by the instruments mentioned above.

The flow field around the model, especially at the leading edge and trailing edge, were measured. In addition, to get a clear comparison, the flow field without the model was measured at the same location using identical method.

In general, the test case matrix was a combination of wind speed, gust amplitude and device status as shown in Table 4-3. All the pertinent cases were tested mainly at 2Hz gust frequency which was expected to be the most critical condition for this model. Nevertheless adjacent frequencies of 1Hz and 3Hz were checked using only 10° maximum blade AoA of gust generator to prove the conclusion drawn from the numerical simulation.

**Table 4-3 Formal test case matrix**

		Gust Freq.	Gust amplitude								
			Device fixed( 0° )			Device fixed(-10°)			Device active		
			0	10°	15°	0	10°	15°	0	10°	15°
Air speed (m/s)	8	1Hz		■			■			■	
		2Hz	■	■	■	■	■	■	■	■	■

		3Hz		■			■			■	
	10	2Hz	■	■	■	■	■	■	■	■	■
	11.7	2Hz	■	■	■	■	■	■	■	■	■

The efficiency of gust response alleviation is mainly based on the amount of aerodynamic load reduction by the negative rotation of the device. The PGAD deflection angle increased proportionately with the dynamic pressure which is represented by wind speed and gust intensity, see Figure 4-17.

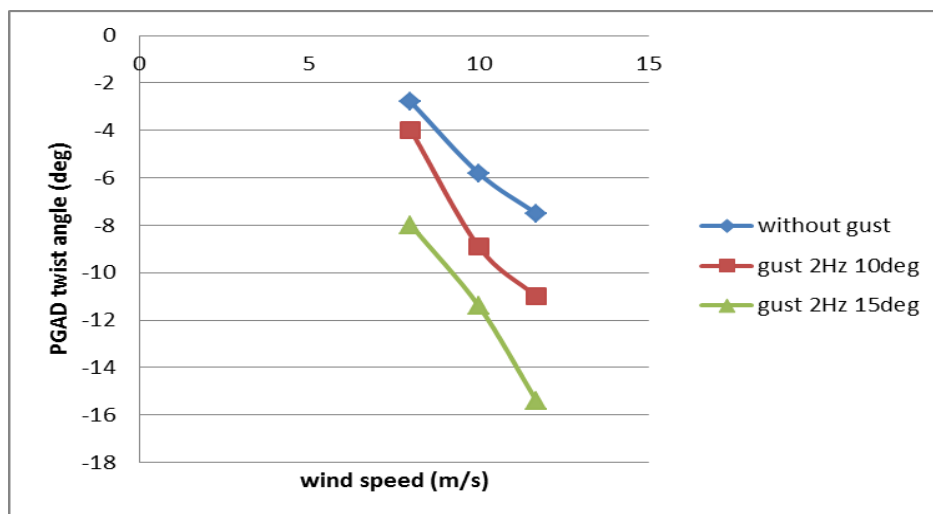


**Figure 4-17 PGAD rotation angle for various cases**

According to Figure 4-18~Figure 4-20, it is clear that the PGAD played a positive role in the alleviation of wing tip oscillation amplitude. The amplitudes in all gust cases tested were reduced when the device was activated. Up to 9.4% alleviation could be achieved.

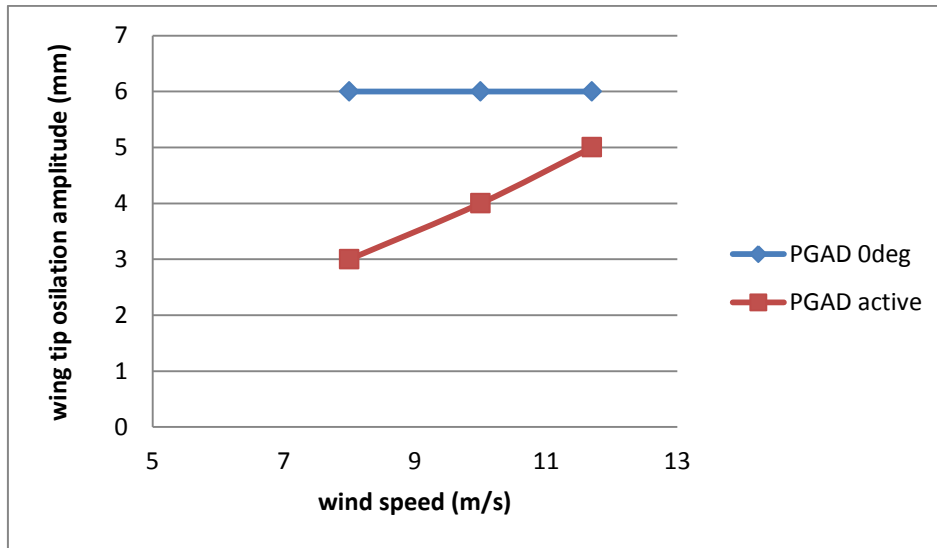


**Figure 4-18 Wing tip deflection without gust**

It should be noted that the amplitude value in Figure 4-18 is not in accordance with the theoretical analysis in which there was no oscillation without turbulence. It can be explained in two ways. Firstly, the flow field is not absolutely steady because the generator structure itself induced perturbation even in the situation with the gust generator off and the blades kept in a neutral position. The second reason is that the amplitude was one order less than the gust case, which makes the system error much more obvious. As to the response with the device activated, another possible reason for the increasing oscillation with wind speed was the increasing vortex intensity generated by the slot between PGAD and wing tip. Details of this vortex are illustrated in Figure 2-15.

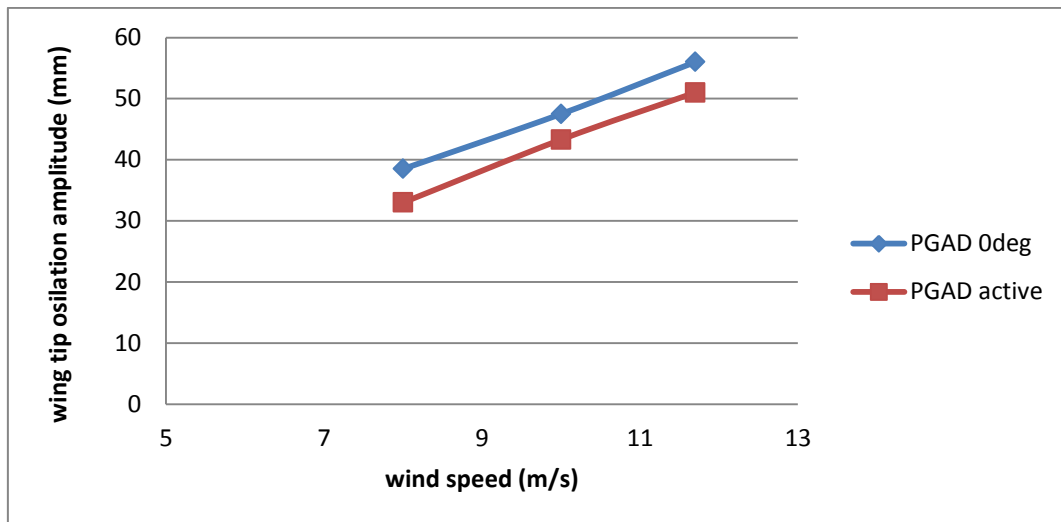


Figure 4-19 Wing tip deflection at 2Hz/10° maximum blade angle

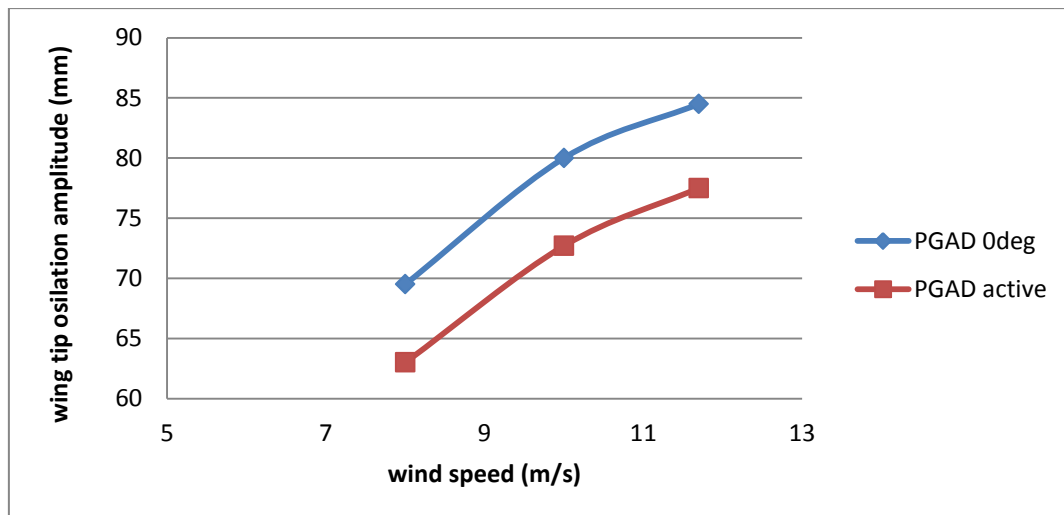
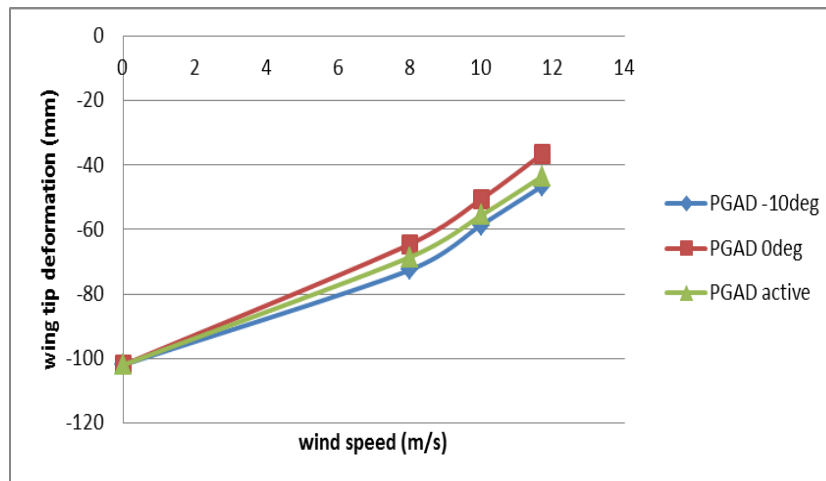


Figure 4-20 Wing tip deflection at 2Hz/15° maximum blade angle

Figure 4-21 shows the neutral position of wing tip displacement taking the wing root as the reference point with the PGAD fixed at  $-10^\circ$ , fixed at  $0^\circ$ , and activated at 8m/s wind speed. The initial value at -105mm indicates the static deflection due to gravity. The trend of the curves makes well agreement with theoretical analysis. 14.3% reduction can be reached when the PGAD is fixed at  $-10^\circ$ .



**Figure 4-21 Wing tip neutral position**

The following results shown in Figure 4-22~Figure 4-25 show the wing response at gust frequencies of 1Hz, 2Hz and 3Hz. A general conclusion can be drawn that in all cases the gust response at 2Hz because it is very close to the first bending mode of this wing model. The response is much greater than the rest of frequencies in terms of wing tip oscillation amplitude/acceleration and wing root bending moment. The results also show that the maximum response reduction due to PGAD occurs at 2Hz. It is noted that the maximum response at 2Hz occurred for PGAD fixed at  $-10^\circ$  which was supposed to be the lowest one. It means that the vortex really plays a negative role in gust alleviation and needs to be solved.

Figure 4-26 (without PGAD) and Figure 4-27 (with PGAD) show a comparison of wing tip oscillation amplitude in the numerical simulation with that in experimentation. A maximum 8.8% difference appears at 2Hz,  $15^\circ$  maximum blade deflection with PGAD which from engineering point of view is reasonable.

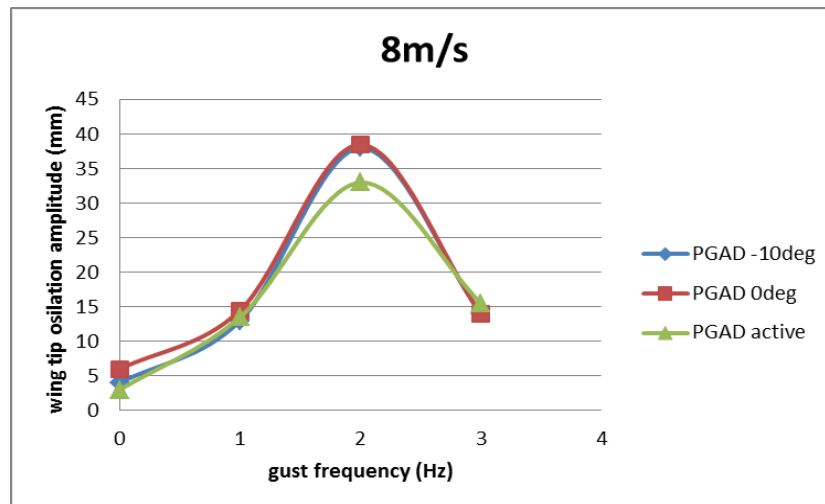


Figure 4-22 Wing tip oscillation amplitude at various gust frequency

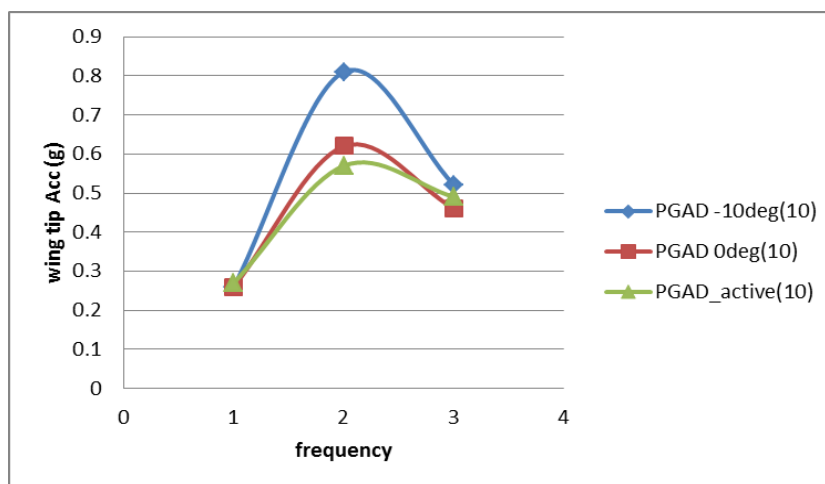


Figure 4-23 Wing tip acceleration at various frequency

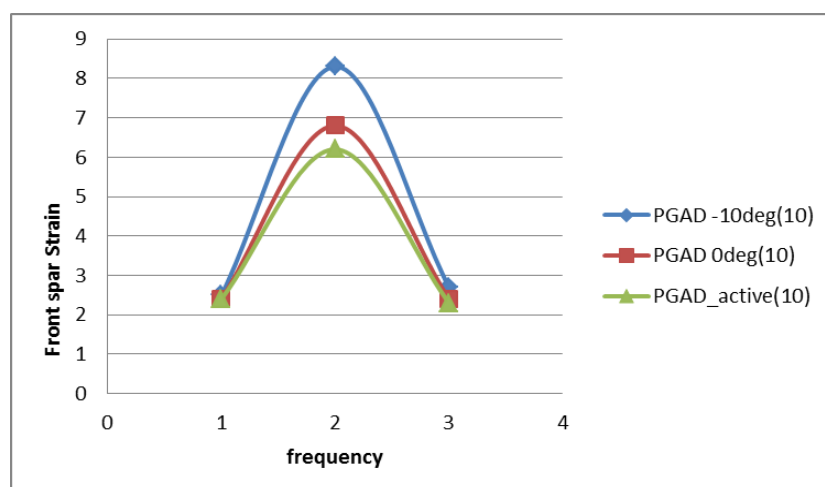


Figure 4-24 Wing root front spar strain at various frequency

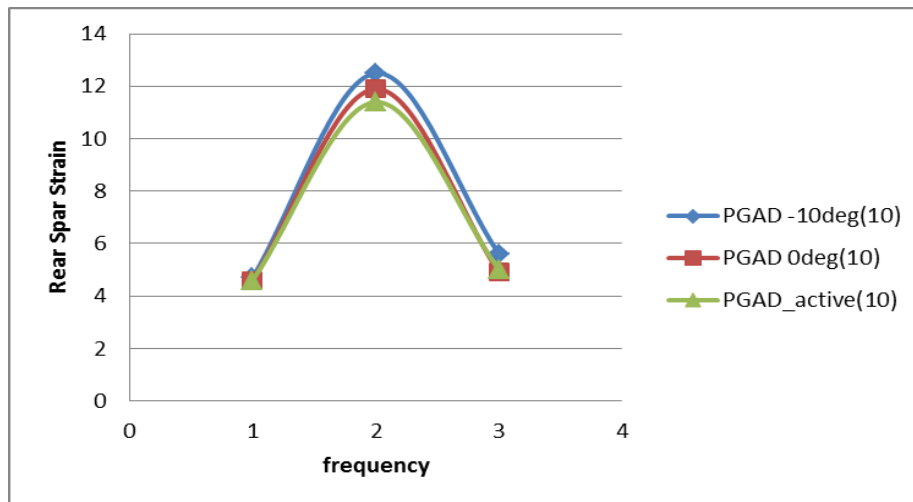


Figure 4-25 Wing root rear spar strain at various frequency

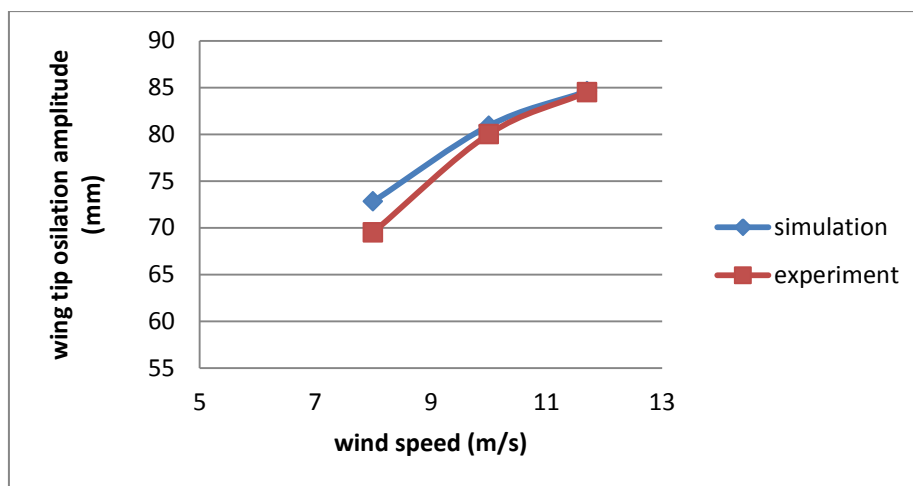


Figure 4-26 Comparison of simulation and experiment without PGAD

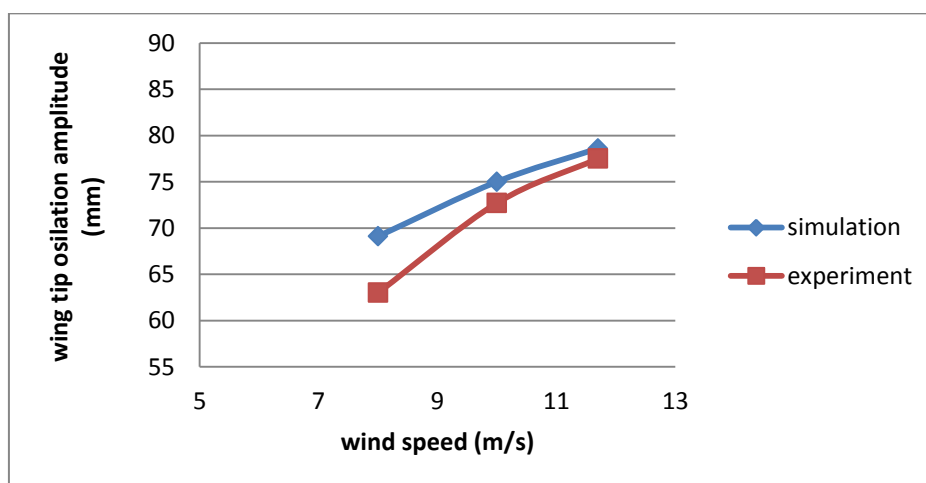


Figure 4-27 Comparison of simulation and experiment with PGAD

## 5 AEROELASTIC TAILORING

Aeroelastic tailoring is a technique in design procedure to alleviate gust response. Theoretically a combination with PGAD should produce more effective reduction. Therefore, an aeroelastic tailoring study was conducted subject initially to minimum gust response. And then, taking PGAD into account, the final efficiency was obtained by performing a comprehensive analysis based on the aeroelastic tailored design. Details are described in this chapter.

In the flight condition of sea level, MTOM, 2.95g gust load factor and 0.3 Mach number, is taken in the following analysis. The aeroelastic tailoring of the wing is performed in the boundary condition of clamped wing root.

### 5.1 Aeroelastic Tailoring of Baseline Wing

Aeroelastic tailoring is a design process to optimize the laminated composite wing structure with specific aeroelastic constraint or objective. It is usually a multi-disciplinary optimization subject to various design constraints. The time cost of executing such a complicated analysis is normally much higher than that without aeroelastic constraint. It is also a challenge to ensure the process converge to an optimal solution if not the ultimate optimal.

A two-stage method developed in the author's previous study [99] has been introduced to solve the problem. It was proved to be more efficient in terms of computing resource consumption.

#### 5.1.1 Weight Optimization

In the first stage of optimization, minimum weight was taken as the design objective subject to static and dynamic strength constraints. The problem can be expressed by Equation (5-1).



$$\left\{ \begin{array}{l} MinW(X) \\ \varepsilon_{lower} \leq 4000\mu\varepsilon \\ \varepsilon_{upper} \leq 3500\mu\varepsilon \\ BLF \geq 1.0 \\ F.I. < 1.0 \\ V_f \geq 1.15V_D \end{array} \right. \quad (5-1)$$

where,

$\varepsilon_{lower}$  is the maximum allowable strain applied to the lower skin

$\varepsilon_{upper}$  is the maximum allowable strain applied to the upper skin

$BLF$  is buckling factor

$F.I.$  is failure index

$V_f$  is flutter velocity

$V_D$  is the maximum diving velocity

The maximum allowable strain of  $4,000 \mu\varepsilon$  and  $3,500 \mu\varepsilon$  under limit load were set for the lower skin in tension and the upper skin in compression respectively. Those values were based on the experimental data taking damage tolerance requirement into consideration [100]. Buckling factor and failure index followed the usual structural design rules. Flutter velocity is defined in CS-25 [87].

In this study case, only the skins were taken in the optimization process since the skin played the dominant role in the wing torsion mode and aeroelastic behaviour.

#### 5.1.1.1 Design Variables

The ply thicknesses and fibre angles were both defined as design variables in the aeroelastic tailoring. The initial layup of the skin laminate was set as quasi-isotropic  $[(0/45/-45/90)_n]_s$  considering manufacturing constraints.

The wing skin was divided into 10 spanwise sections for both upper and lower skin panels. To reduce the number of design variables and improve the computational efficiency accordingly, the plies with same initial orientation in each panel were grouped. One design variable was defined to represent the change of individual group. It meant that only 4 angular design variables for each panel. Under the constraint of balanced laminate layup,  $45^\circ$  and  $-45^\circ$  can share the same angular variable. Thus, the number was further reduced to 3 for each skin panel, and 6 variables for one section. For the whole wing divided into 10 sections, there are 60 design variables for the fiber orientations in total.

Regarding the ply thickness, the same process was applied considering manufacture constraint [99]. So, another 60 design variables were defined for ply thicknesses. There are two ways to deal with the boundary of thickness variables. The simple way is to define a lower and upper limit for the ply thickness. The optimized laminate will show the overall thickness with the optimal layup. Alternatively, release the boundary limit during the optimization and rearrange the stacking sequence in a post-processing after aeroelastic tailoring. The tailored thickness will be trimmed in the post processing according to the practical material property (standard ply thickness).

#### **5.1.1.2 Design Constraints**

Design constraints have significant influence in the optimization once design objective, design variables and algorithm have been set. Ideally, all the related constraints should be included in a multi-disciplinary optimization (MDO) process. In practice however, limited constraints are considered for a compromise engineering solution because of the risk of conflict among multi-constraints. In the latter case, the iteration either cannot converge or terminates due to uncertainty or numerical errors. Even if the MDO can be carried out without any conflict, the time cost will still be very high and some of the constraints may not even be satisfied. Therefore only the major and critical constraints are normally employed in the process.

In this study, maximum strain and failure index were introduced as static strength constraints while the flutter was taken as aeroelastic constraint. It

should be noted that the buckling constraint shown in Equation (5-1) was excluded to improve the optimization speed. The reason is that the results of a skin panel design subject to buckling by another researcher [92] shows that the buckling boundary is far away from the current design.

### 5.1.1.3 Results and Discussion

In this case study, the optimization terminated at the 27<sup>th</sup> iteration with the 32.3% reduction of skin weight from 1.812T to 1.226T as shown in Figure 5-1. It is also shown in Figure 5-2 that the maximum wing tip deflection dropped down slightly from 2,981mm to 2,747mm.

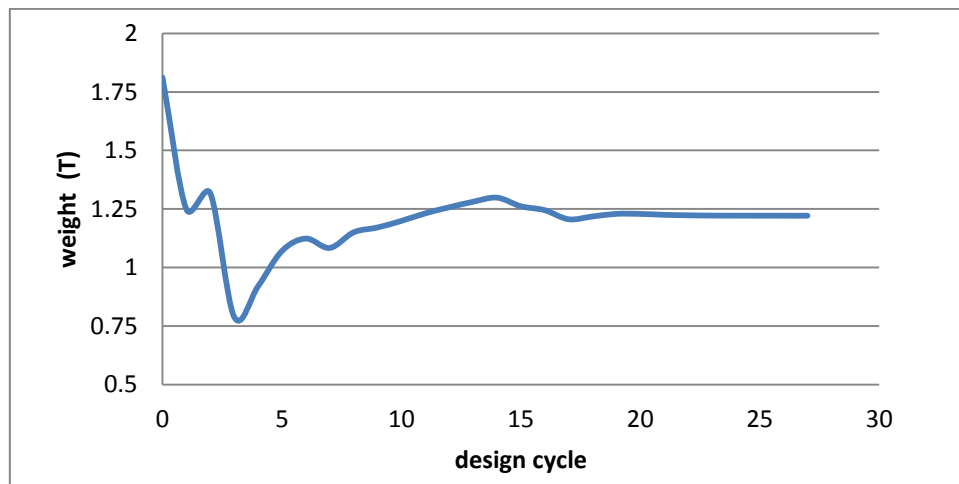


Figure 5-1 Objective function history of weight optimization

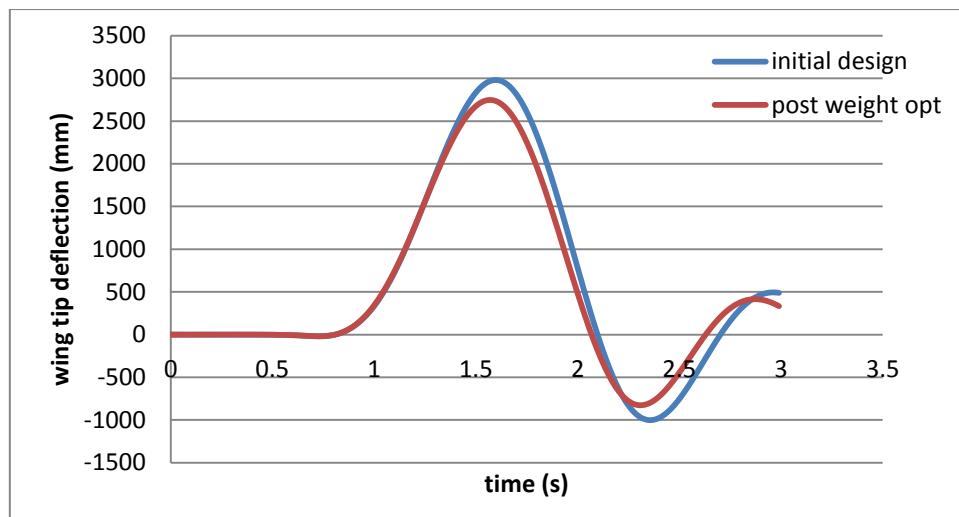
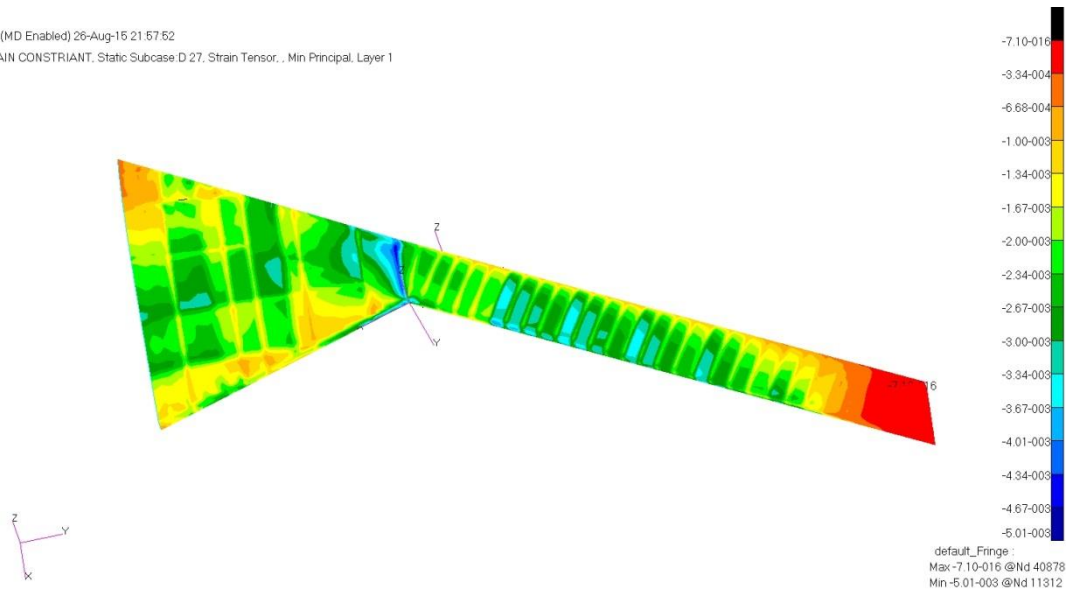


Figure 5-2 Wing tip response to gust after weight optimization

Patran 2010 (MD Enabled) 28-Aug-15 21:57:52

Fringe: STRAIN CONSTRIANT, Static Subcase: D 27, Strain Tensor, Min Principal, Layer 1



**Figure 5-3 Optimized strain distribution of upper skin**

The strain after weight optimization was much more evenly distributed than the original design as shown for the upper skin in Figure 5-3. The only elements that reached the constraint boundary were located in the kink. This was due to the dramatic change of geometry and discontinuity of fibre orientation in the region. At the wing tip region, the lower boundary of ply thickness was reached and the thickness could not be further reduced although the strain was already very low.

**Table 5-1 Failure Index constraint comparison**

	Element ID	Lamina No.	Max. F.I. Value	Upper Bound	Activation
Initial	15856	2	0.62	1.0	No
Post opt	15856	2	0.79	1.0	No

As shown in Table 5-1, the maximum Failure Index was below the ultimate limit although the value increased from 0.62 to 0.79. This indicates that not all the constraints are critical in the specific study case.

The flutter speed of the initial design was 256 m/s associated with the coupling of the first bending and first torsion mode as shown in Figure 5-4 and Figure 5-5. The flutter velocity was increased to 345 m/s with the mode switched to second bending and first torsion coupling as shown in Figure 5-6 and Figure 5-7

after weight optimization. Both weight saving and flutter improvement were achieved in the same optimization process.

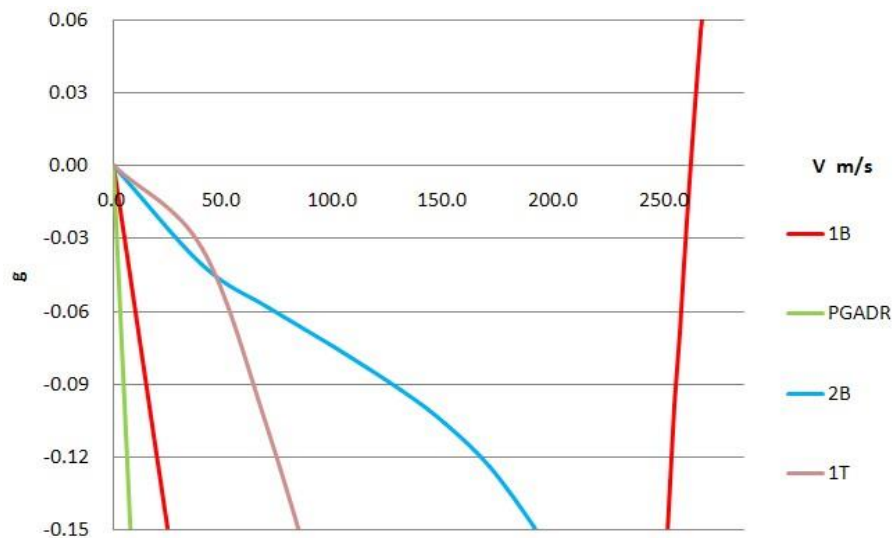


Figure 5-4 V-g diagram of initial design

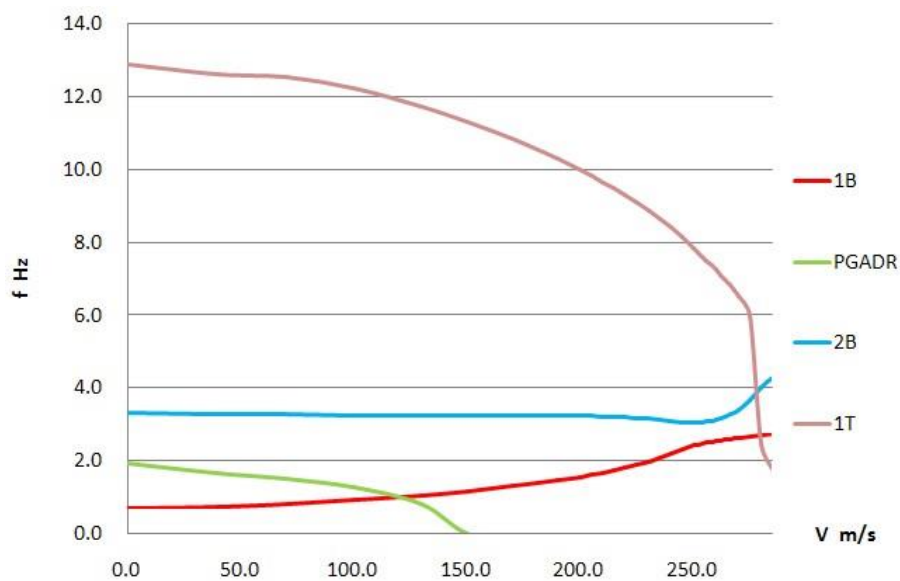


Figure 5-5 V-f diagram of initial design

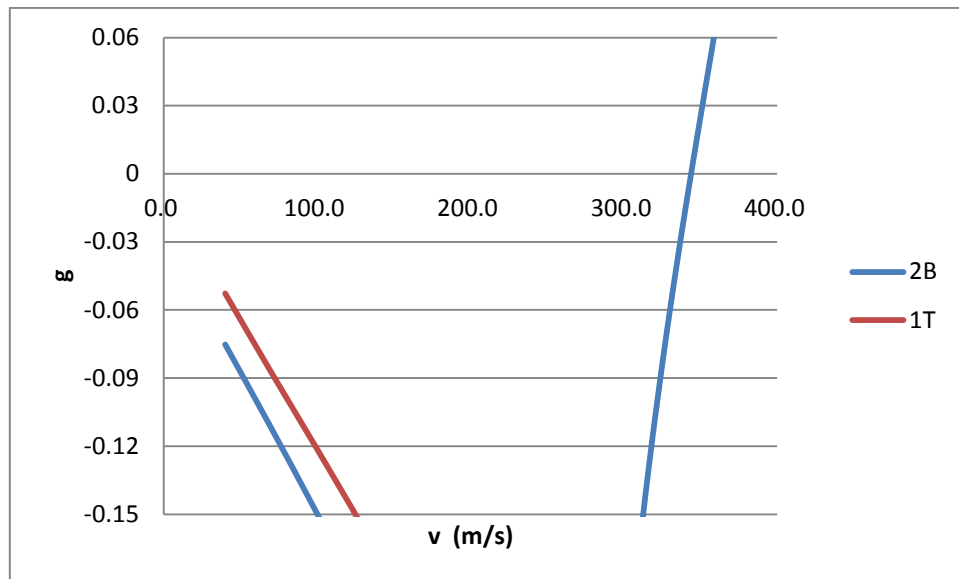


Figure 5-6 V-g diagram of weight optimized design

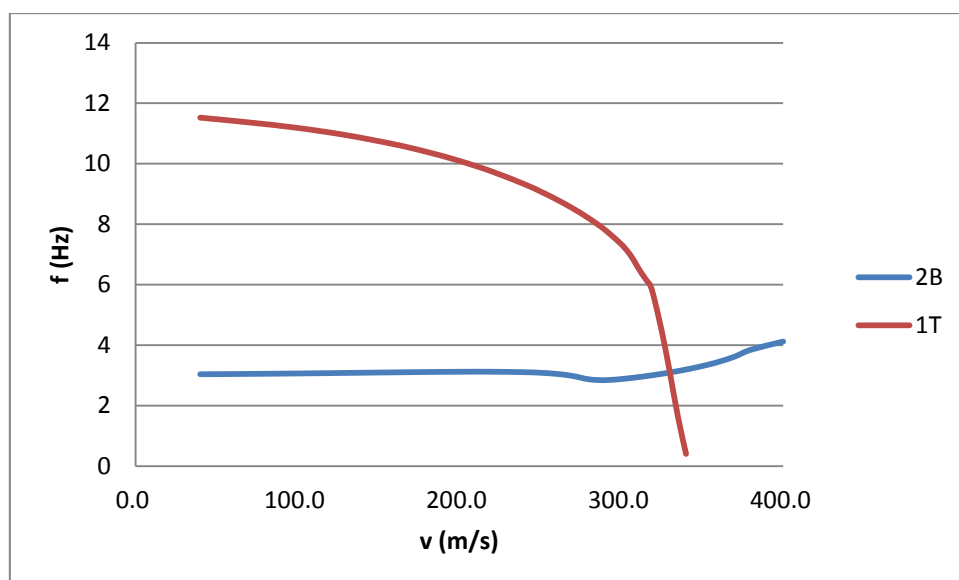


Figure 5-7 V-f diagram of weight optimized design

### 5.1.2 Aeroelastic Tailoring for Minimum Gust Response

As stated above, the second stage aeroelastic tailoring for gust alleviation was executed by taking the last weight optimized design as the starting point. The procedure can be described as in Equation (5-2). The design objective was to minimize the maximum gust response at the wing tip in the time domain.

$$\left\{ \begin{array}{l} \text{Min Disp. (X)} \\ \varepsilon_{\text{lower}} \leq 4000\mu\varepsilon \\ \varepsilon_{\text{upper}} \leq 3500\mu\varepsilon \\ F.I. < 1.0 \\ V_f \geq 1.15V_D \\ W_{\text{skin}} \leq W_{\text{skin initial}} \end{array} \right. \quad (5-2)$$

where,

$W_{\text{skin}}$  is the skin weight which is defined as an additional constraint

$W_{\text{skin initial}}$  is the skin weight of initial design (1.812T in this case)

#### 5.1.2.1 Design Variables and Constraints

It is not necessary to keep all the design variables from the previous stage-one optimization since the laminate has already been optimized. In this case, a coefficient was introduced to vary all ply thickness in proportion simultaneously while the layup was maintained as before.

For the gust response alleviation, an additional constraint was defined, namely that the skin weight should be no more than the initial design. That meant this stage of optimization process was aeroelastic tailoring without any weight penalty compared with the initial design.

Since the optimized laminate layup was determined, the stress distribution of the whole structure would remain and the strain level should decrease with the increasing stiffness due to increase of thickness. Some of the constraints listed in Equation (5-2) would not be critical at this stage of optimization and hence released, such as F.I. and maximum strain. The flutter constraint was retained as before.

### 5.1.2.2 Results and Discussion

At this stage of analysis, the optimization converged rapidly within just 10 iterations with the maximum wing tip response reduced almost linearly to 2,310mm as shown in Figure 5-8 and Figure 5-9.

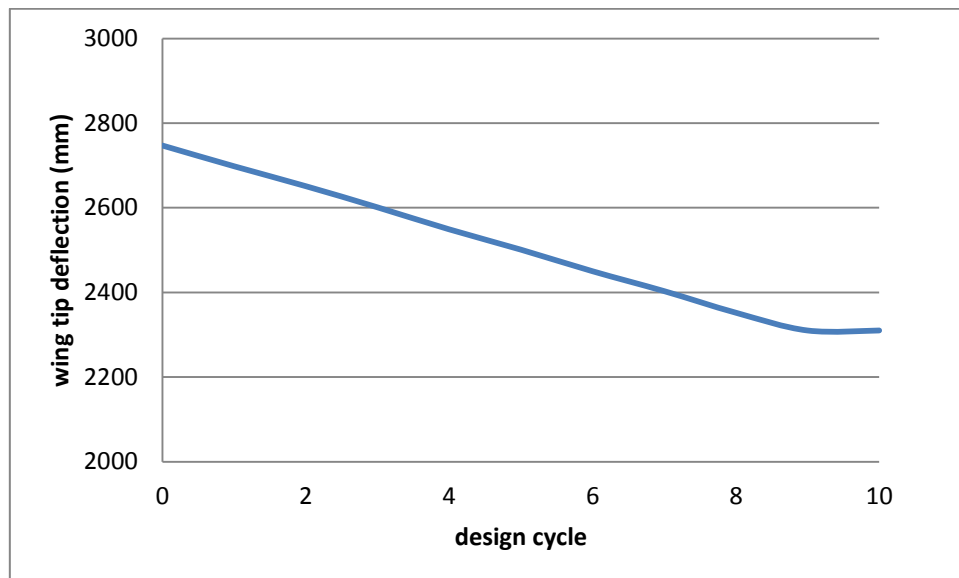


Figure 5-8 Objective function history of gust response optimization

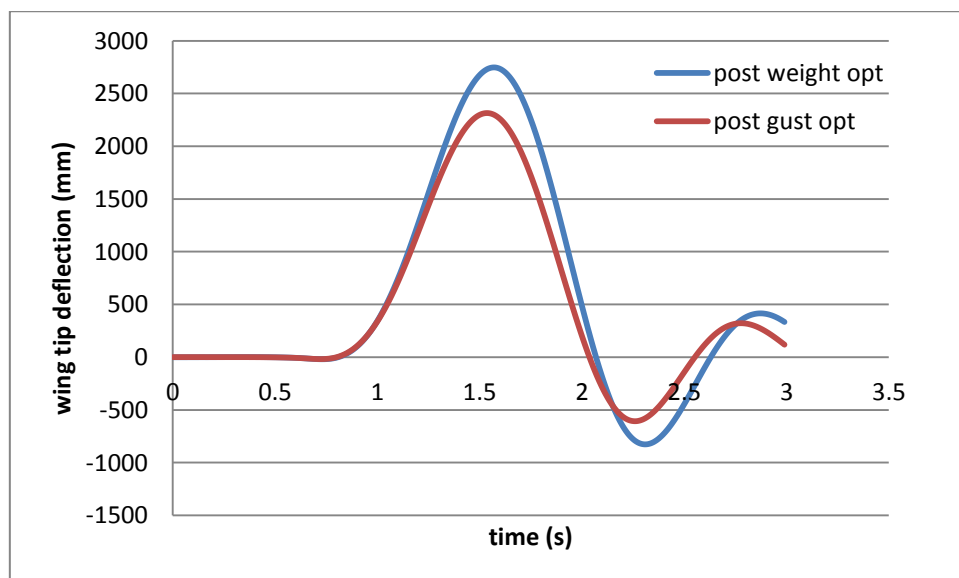
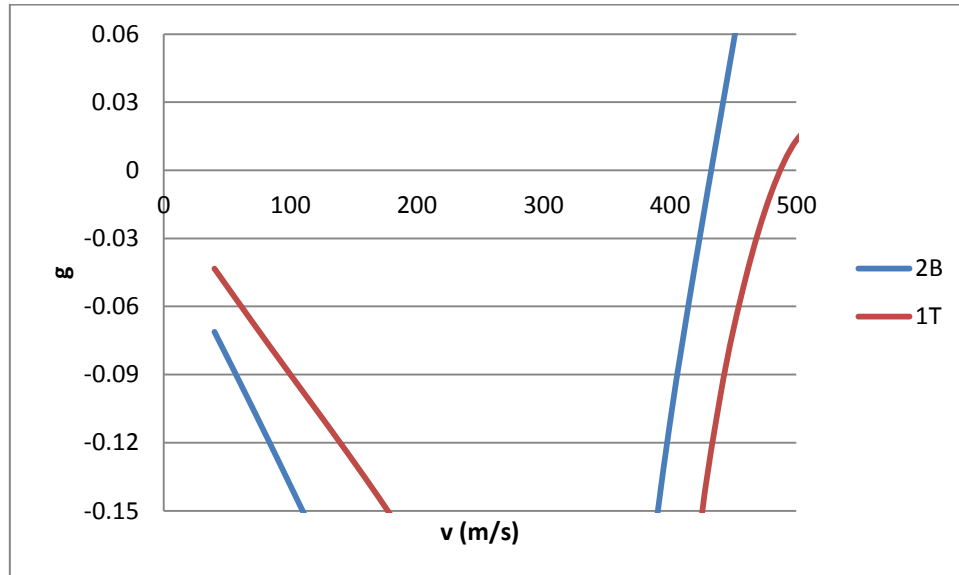


Figure 5-9 Wing tip deflection in gust response optimization



As a result of the aeroelastic tailoring, the flutter speed increased to 433m/s as shown in Figure 5-10 and Figure 5-11. It was because of the obvious increase of wing stiffness due to increased skin thickness.



**Figure 5-10 V-g diagram of gust optimized design**

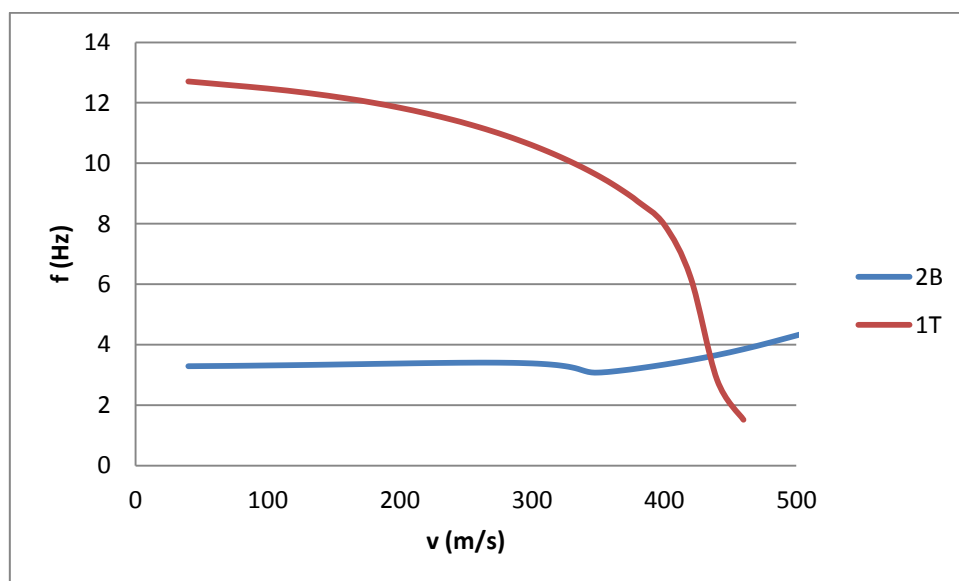


**Figure 5-11 V-f diagram of gust optimized design**

After the above two-stage optimization, a total 22.5% decrease of the gust response measured by maximum wing tip deflection was achieved without any weight penalty. A weight constraint can be imported if required.

## 5.2 Gust Response of Wing with PGAD

The study described in this section was to find out the combined effect of aeroelastic tailoring and PGAD. It can be determined by taking the optimal design of the above aeroelastic tailoring as the start point.

In this procedure, the torsion spring between PGAD and wing tip was set to the optimal stiffness obtained from previous study. The result in Figure 5-12 shows that the gust response measured at the wing tip gained a further 7.8% reduction from 2,310mm to 2,133mm with PGAD activated.

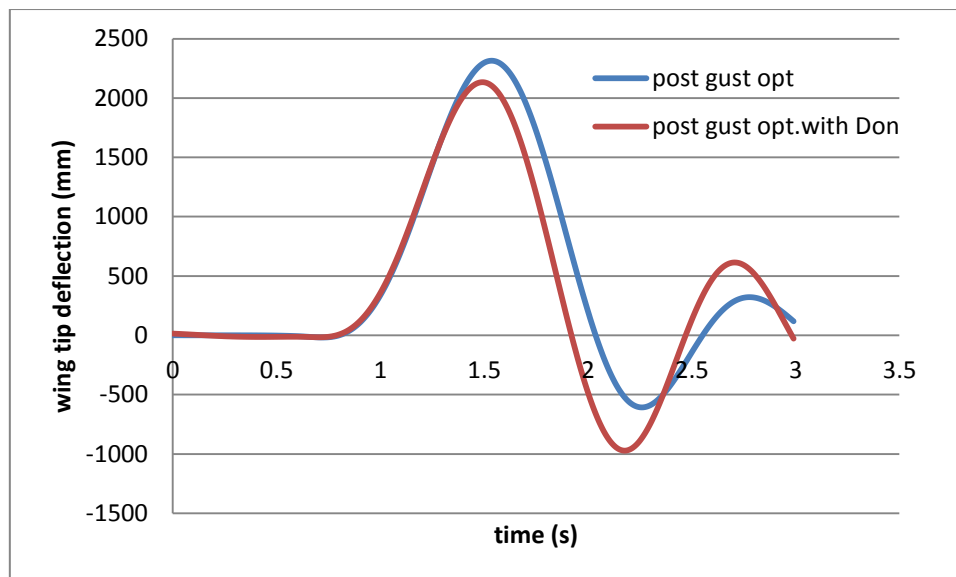


**Figure 5-12 Wing tip deflection with PGAD switched on**

It should be noted in Figure 5-12 that the second peak of wing tip deflection increased when PGAD was activated. This phenomenon was due to the relatively lower structural damping induced by the softer torsion spring. Therefore, it will take a longer time for the oscillation to damp out.

As shown in Figure 5-13 and Figure 5-14, the flutter mode switched to third bending coupling with first torsion at 416m/s. The rotational mode of PGAD led to a small reduction of flutter speed and frequency.

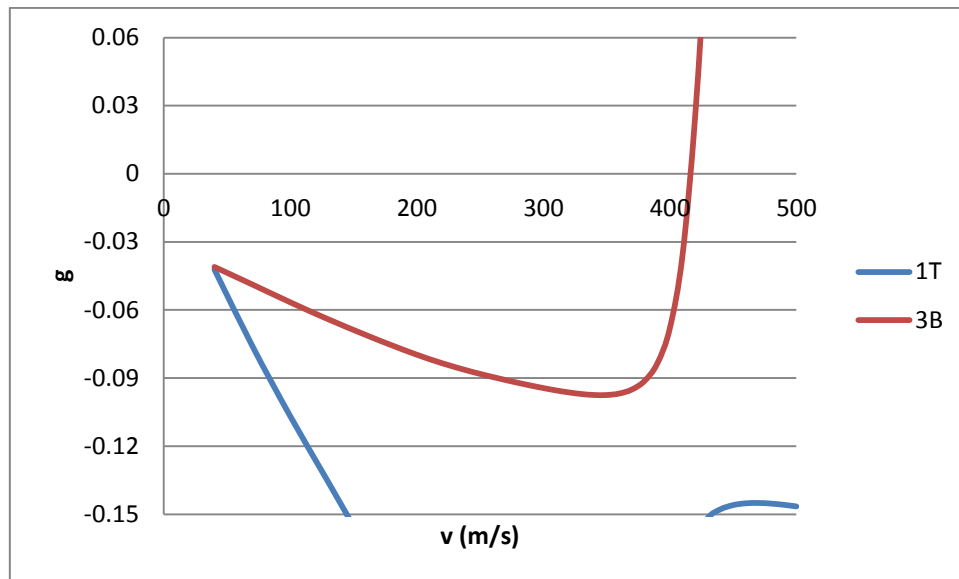


**Figure 5-13 V-g diagram of optimized design with PGAD**

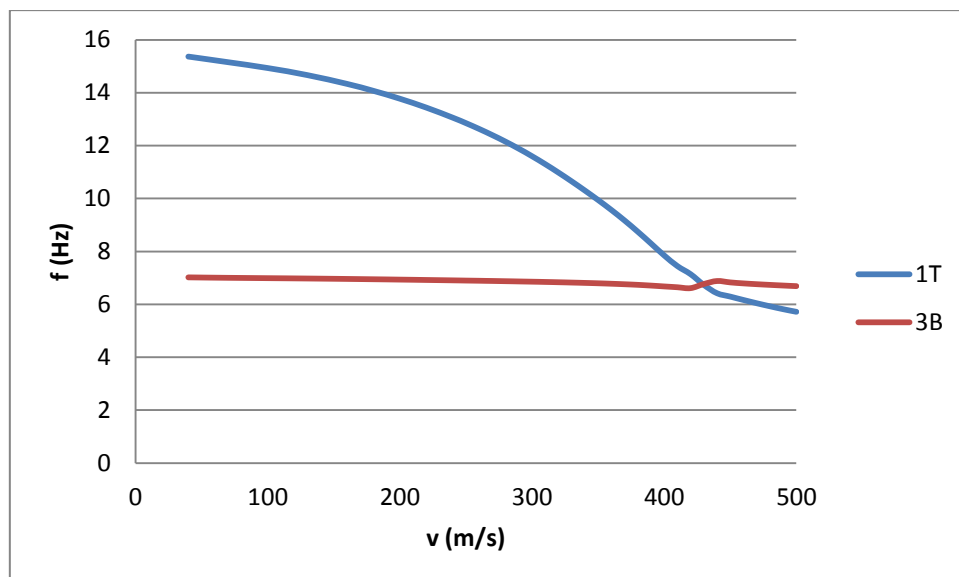


**Figure 5-14 V-f diagram of optimized design with PGAD**

The study has shown that 28.5% reduction of gust response measured as wing tip deflection has been achieved by combining the wing aeroelastic tailoring with the PGAD activation. This is a significant design improvement including 22% reduction by aeroelastic tailoring only and 8.8% by PGAD only.

Though not the objective of this aeroelastic tailoring, the flutter characteristics were also improved significantly. The flutter speed was increased by nearly 70% after the aeroelastic tailoring. Even if the PGAD is activated for the optimized

wing, the flutter speed was reduced by only 4.5% with the figure still much higher than the initial design. The safety margin means that the proposed technology has little negative effect on flutter and there was still a great potential to improve the design.

## 6 CONCLUSION

The feasibility and effectiveness of the passive gust alleviation device for the application of a sensorcraft of flying-wing configuration has been tested and validated by wind tunnel test. Previous numerical study showed that PGAD can effectively reduce the gust response by 15% (wing fixed at root). In the current project, a 1:25 dynamically scale model was successfully designed and manufactured to meet the dynamic similarity of the full scale aircraft wing for wind tunnel test. The scaled wing model was validated by a ground vibration test with a frequency deviation within 7% for the first five modes.

Based on the scaled model, numerical analysis shows that 8.8% gust response reduction can be achieved. For the wind tunnel test, a gust generator with two rotating blades driven by a motor was also manufactured to produce the required turbulence. The wind tunnel test results indicate that the test model with PGAD can alleviate gust load by 9.4%.

The study has been extended to aeroelastic tailoring of the composite wing structure for minimum gust response. The results show that a combination of aeroelastic tailoring and the PGAD lead to more effective gust alleviation by 28.5%.

Beyond the scope of the current study, an initial flutter analysis was made for the flying-wing aircraft in free flight mode. The study shows that the coupling of the aircraft rigid body pitching mode and the wing bending mode and the PGAD twist has significant impact on the flutter behaviour and velocity.

## REFERENCES

- [1] Noll, T. E., Brown, J. M., Perez-Davis, M. E., Ishmael, S. D., Tiffany, G. C. and Gaier, M. (2004), *Investigation of the Helios Prototype Aircraft Mishap*, vol.1, Mishap Report, NASA Report.
- [2] Ghiasi, H., Fayazbakhsh, K., Pasini, D. and Lessard, L. (2010), "Optimum stacking sequence design of composite materials Part II: Variable stiffness design", *Composite Structures*, vol. 93, no. 1, pp. 1-13.
- [3] Ghiasi, H., Pasini, D. and Lessard, L. (2009), "Optimum stacking sequence design of composite materials Part I: Constant stiffness design", *Composite Structures*, vol. 90, no. 1, pp. 1-11.
- [4] Evrard, T., Butler, R., Hughes, S. W. and Banerjee, J. R. (2000), "Ply angle optimization of nonuniform composite beams subject to aeroelastic constraints", *AIAA journal*, vol. 38, no. 10, pp. 1992-1994.
- [5] Keller, D. (2010), "Optimization of ply angles in laminated composite structures by a hybrid, asynchronous, parallel evolutionary algorithm", *Composite Structures*, vol. 92, no. 11, pp. 2781-2790.
- [6] Stanford, B. and Beran, P. (2013), "Optimal thickness distributions of aeroelastic flapping shells", *Aerospace Science and Technology*, vol. 24, no. 1, pp. 116-127.
- [7] James, K. A., Kennedy, G. J. and Martins, J. R. R. A. (2014), "Concurrent aerostructural topology optimization of a wing box", *Computers & Structures*, vol. 134, pp. 1-17.
- [8] Elham, A. (2015), "Adjoint quasi-three-dimensional aerodynamic solver for multi-fidelity wing aerodynamic shape optimization", *Aerospace Science and Technology*, vol. 41, pp. 241-249.
- [9] Hodges, D. H. and Pierce (2002), *Introduction to structural dynamics and aeroelasticity*, Cambridge University Press, Cambridge.
- [10] Collar, A. R. (1946), "The Expanding Domain of Aeroelasticity", *Journal of the Royal Aeronautical Society*, vol. 50, no. 428, pp. 613-636.

- [11] Bisplinghoff, R. L., Ashley, H. and Halfman, R. L. (1955), *Aeroelasticity*, Addison-Wesley Publishing Co., Inc.
- [12] Banerjee, J. R. (1984), "Flutter characteristics of high aspect ratio tailless aircraft", *Journal of Aircraft*, vol. 21, no. 9, pp. 733-736.
- [13] Banerjee, J. R. (1988), "Flutter modes of high aspect ratio tailless aircraft", *Journal of Aircraft*, vol. 25, no. 5, pp. 473-476.
- [14] Eslimy-Isfahany, S. H. R. and Banerjee, J. R. (1997), "Dynamic Response of Composite Beams with Application to Aircraft Wings", *Journal of Aircraft*, vol. 34, no. 6, pp. 785-791.
- [15] Roberts, Jr., R. W., Canfield, R. A. and Blair, M. (2005), "Sensor-craft structural optimization and analytical certification", *46th AIAA/ASME/ASCE/AHS/ASC Structures, Structural Dynamics and Materials Conference*, Vol. 4, 18 April 2005 through 21 April 2005, Austin, TX, pp. 2683.
- [16] Tang, D. M. and Dowell, E. H. (2001), "Experimental and Theoretical Study on Aeroelastic Response of High-Aspect-Ratio Wings", *AIAA Journal*, vol. 39, no. 8, pp. 1430-1441.
- [17] Banerjee, J. R., Liu, X. and Kassem, H. I. (2014), "Aeroelastic stability analysis of high aspect ratio aircraft wings", *Journal of Applied Nonlinear Dynamics*, vol. 3, no. 4, pp. 413-422.
- [18] Balakrishnan, A. V., Tuffaha, A. M., Patino, I. and Melnikov, O. (2014), "Flutter analysis of an articulated high aspect ratio wing in subsonic airflow", *Journal of the Franklin Institute*, vol. 351, no. 8, pp. 4230-4250.
- [19] Shirk, M. H., Hertz, T. J., and Weisshaar, T. A. (1986), "Aeroelastic tailoring-Theory, Practice, and Promise", *Journal of Aircraft*, vol. 23, no. 1, pp. 6-18.
- [20] Sobieszczanski-Sobieski, J. and Haftka, R. T. (1996), "Multidisciplinary aerospace design optimization: survey of recent developments", *34th AIAA Aerospace Sciences Meeting and Exhibit*, Vol. AIAA-1996-0711.

- [21] Lillico, M., Butler, R., Guo, S. and Banerjee, J. R. (1997), "Aeroelastic optimisation of composite wings using the dynamic stiffness method", *Aeronautical Journal*, vol. 101, no. 1002, pp. 77-86.
- [22] Attaran, A., Majid, D. L., Basri, S., Mohd Rafie, A. S. and Abdullah, E. J. (2011), "Structural optimization of an aeroelastically tailored composite flat plate made of woven fiberglass/epoxy", *Aerospace Science and Technology*, vol. 15, no. 5, pp. 393-401.
- [23] Guo, S., Banerjee, J. R., and Cheung, C. W. (2003), "Effect of laminate lay-up on the aeroelastic behaviour of composite wings", *Proceedings of the Institution of Mechanical Engineers, Part G, Journal of Aerospace Engineering*, vol. 217, pp. 115-122.
- [24] Guo, S., Banerjee, J. and Cheung, C. (2003), "The effect of laminate lay-up on the flutter speed of composite wings", *Journal of Aerospace Engineering*, vol. 217, no. 3.
- [25] Isogai, K. (1989), "Direct search method to aeroelastic tailoring of a composite wing under multiple constraints", *Journal of Aircraft*, vol. 26, no. 12, pp. 1076-1080.
- [26] Kameyama, M. and Fukunaga, H. (2007), "Optimum design of composite plate wings for aeroelastic characteristics using lamination parameters", *Computers & Structures*, vol. 85, no. 3-4, pp. 213-224.
- [27] Guo, S., Cheng, W. and Cui, D. (2006), "Aeroelastic tailoring of composite wing structures by laminate layup optimization", *AIAA Journal*, vol. 44, no. 12, pp. 3146-3150.
- [28] Kim, T. and Hwang, I. H. (2005), "Optimal design of composite wing subjected to gust loads", *Computers & Structures*, vol. 83, no. 19-20, pp. 1546-1554.
- [29] Chedrik, V. V. (2012), "Aero-structural optimization of high-aspect-ratio wings", *12th AIAA Aviation Technology, Intergration, and Operations(ATIO) Conference and 14th AIAA/ISSM*, 17-19 Sept. 2012, Indianapolis, Indiana, .



- [30] Rothwell, A. (1991), "Multi-level optimization of aircraft shell structures", *Thin-Walled Structures*, vol. 11, no. 1–2, pp. 85-103.
- [31] Weisshaar, T. A. (1981), "aeroelastic tailoring of forward swept composite wings", *Journal of Aircraft*, vol. 18, no. 8, pp. 669-676.
- [32] Wan, Z., Yan, H., Liu, D. and Yang, C. (2005), "Aeroelastic Analysis and Optimization of High-aspect-ratio Composite Forward-swept Wings", *Chinese Journal of Aeronautics*, vol. 18, no. 4, pp. 317-325.
- [33] Gretchikhine, A. (2011), *Su-47/S-37 Berkut*, available at: [www.globalsecurity.org/military/world/russia/su-47.htm](http://www.globalsecurity.org/military/world/russia/su-47.htm) (accessed Sept, 2015).
- [34] Calzada, R. (2015), *X-29*, available at: [http://www.nasa.gov/centers/dryden/multimedia/imagegallery/X-29/X-29\\_proj\\_desc.html](http://www.nasa.gov/centers/dryden/multimedia/imagegallery/X-29/X-29_proj_desc.html) (accessed Sept.,2015).
- [35] Hobbit, F.M., ( 1988), *Gust loads on aircraft: concept and applications*, AIAA education series, Washington DC.
- [36] Fuller, J. R. (1995), "Evolution of airplane gust loads design requirements", *Journal of Aircraft*, vol. 32, no. 2, pp. 325.
- [37] Wright, J. R. and Cooper, J. E. (2007), *Introduction to aircraft aeroelasticity and loads*, American Institute of Aeronautics and Astronautics, Reston, VA.
- [38] Abdelmoula, F. (1999), "Design of an Open-Loop gust alleviation control system for airborne gravimetry", *Aerospace Science and Technology*, vol. 3, no. 6, pp. 379-389.
- [39] Britt, R. T., Jacobson, S. B. and Arthurs, T. D. (2000), "Aeroservoelastic analysis of the B-2 bomber", *Journal of Aircraft*, vol. 37, no. 5, pp. 745-752.
- [40] Shao, K., Wu, Z., Yang, C., and Chen, L. (2010), "Theoretical and Experimental Study of Gust Response Alleviation Using Neuro-fuzzy Control Law for a Flexible Wing Model", *Chinese Journal of Aeronautics*, vol. 23, no. 3, pp. 290-297.

- [41] Kobayashi, H. and Hatanaka, A. (1992), "Active generation of wind gust in a two-dimensional wind tunnel", *Journal of Wind Engineering and Industrial Aerodynamics*, vol. 42, no. 1–3, pp. 959-970.
- [42] Disney, T. E. (1975), "The C-5A active load alleviation system", *AIAA Journal*, , no. 75, pp. 991.
- [43] Honlinger, H., Zimmermann, H., Sensburg, O. K. and Becker, J. (1995), "Structural aspects of active control technology", *AGARD Flight mechanics Panel Symposium*, Turin, Italy.
- [44] Frederick, M., Kerrigan, E. C. and Graham, J. M. R. (2010), "Gust alleviation using rapidly deployed trailing-edge flaps", *Journal of Wind Engineering and Industrial Aerodynamics*, vol. 98, no. 12, pp. 712-723.
- [45] Cesnik, C.E.S., Ortega-Morales, M., and Patil, M. J. (2000), "Active Aeroelastic Tailoring of High Aspect Ratio Composite Wings", AIAA-2000-1331, AIAA Report.
- [46] Norris, G. and Wagner, M. (2005), *Airbus A380:superjumbo of the 21st century*, Zenith Press, St.Paul,MN.
- [47] Noris, G. and Wagner, M. (2009), *Boeing 787 Dreamliner*, Zenith Press, Minneapolis,MN.
- [48] Roesch, P. and Harlan, R. B. (1975), *A passive gust alleviation system for a light aircraft*, CR-2605, NASA, Washington,D.C.
- [49] Miller, S., Vio, G. A. and Cooper, J. E. (2009), "Development of an adaptive wing tip device", *50th AIAA/ASME/ASCE/AHS/ASC Structures, Structural Dynamics and Materials Conference*, May 4-7, Palm Springs,CA, AIAA, United States.
- [50] Miller, S., Vio, G. A., Cooper, J. E. and Sensburg, O. K. (2008), "Optimisation of a scaled sensorcraft model with passive gust alleviation", *12th AIAA/ISSMO Multidisciplinary Analysis and Optimization Conference*, September 10-12, Victoria, BC, AIAA, Canada .

- [51] Guo, S., Cheung, W., Banerjee, J. and Butlar, R. (June,1995), "Gust alleviation and flutter suppression of an optimised composite wing", *the International Forum on Aeroelasticity and Structural Dynamics*, Manchester,U.K., pp. pp.41.1-41.9.
- [52] Perron, S. G. (2012), *Passive gust load alleviation through bend- rotation coupling of composite beams on typical commercial airplane wings*, Msc thesis, Massachusetts Institute of Technology.
- [53] Guo, S., Li, D. and Liu, Y. (2012), "Multi-objective optimization of a composite wing subject to strength and aeroelastic constraints", *Proceedings of the Institution of Mechanical Engineers, Part G: Journal of Aerospace Engineering*, vol. 226, no. 9, pp. 1095-1106.
- [54] Niu, M. (1999), *Airframe Stress Analysis and Sizing*, 2nd Edition, Hong Kong conmlit press ltd., 22/F, Sing Pao Building, 101 King's Road, North Point, Hong Kong.
- [55] Jones, R. (1999), *Mechanics of composite materials*, 2nd Edition, Taylor & Francis, Inc., 325 Chestnut Street, Philadelphia, PA 19106.
- [56] Kere, P., Lyly, M. and Koski, J. (2003), "Using multicriterion optimization for strength design of composite laminates", *Composite Structures*, vol. 62, no. 3–4, pp. 329-333.
- [57] Naik, N. G., Gopalakrishnan, S. and Ganguli, R. (2008), "Design optimization of composites using genetic algorithms and failure mechanism based failure criterion", *Composite Structures*, vol. 83, no. 4, pp. 354-367.
- [58] Guo, S. (2007), "Aeroelastic optimization of an aerobatic aircraft wing structure", *Aerospace Science and Technology*, vol. 11, no. 5, pp. 396-404.
- [59] Barcelos, M. and Maute, K. (2008), "Aeroelastic design optimization for laminar and turbulent flows", *Computer Methods in Applied Mechanics and Engineering*, vol. 197, no. 19–20, pp. 1813-1832.
- [60] Gern, F. H. (2000), "Passive load alleviation in the design of a strut-braced wing transonic transport", *8th AIAA/USAF/NASA/ISSMO*

*Symposium on Multidisciplinary Analysis and Optimization*, 6-8 Sept.2000, Long Beach, CA.

- [61] Chintapalli, S., Elsayed, M. S. A., Sedaghati, R. and Abdo, M. (2010), "The development of a preliminary structural design optimization method of an aircraft wing-box skin-stringer panels", *Aerospace Science and Technology*, vol. 14, no. 3, pp. 188-198.
- [62] Walker, M., Reiss, T., Adali, S. and Weaver, P. M. (1998), "Application of MATHEMATICA to the optimal design of composite shells for improved buckling strength", *Engineering Computations*, vol. 15, no. 2, pp. 260-267.
- [63] Park, W. J. (1983), "An optimal design of simple symmetric laminates under the first ply failure criterion", *Journal of Composite Materials*, vol. 16, pp. 341-355.
- [64] Venkataraman, S. and Haftka, R. T. (1999), "Optimization of composite panels- A review", *Proceedings of the 14th Annual Technical Conference of the American Society for Composites*, Dayton, OH, Sep.27-29
- [65] Erdal, O. and Sonmez, F. O. (2005), "Optimum design of composite laminates for maximum buckling load capacity using simulated annealing", *Composite Structures*, vol. 71, no. 1, pp. 45-52.
- [66] Miki, M. and Nakayasu, H. (1982), "Variation of in-plane elastic constants in material design of composite laminates", *Zairyo/Journal of the Society of Materials Science, Japan*, vol. 31, no. 351, pp. 1176-1182.
- [67] Kere, P. and Koski, J. (2002), "Multicriterion optimization of composite laminates for maximum failure margins with an interactive descent algorithm", *Structural and Multidisciplinary Optimization*, vol. 23, no. 6, pp. 436-447.
- [68] António, C. C., Marques, A. T. and Soeiro, A. V. (1995), "Optimization of laminated composite structures using a bilevel strategy", *Composite structures*, vol. 33, no. 4, pp. 193-200.

- [69] Lund, E. and Stegmann, J. (2005), "On structural optimization of composite shell structures using a discrete constitutive parametrization", *Wind Energy*, vol. 8, no. 1, pp. 109-124.
- [70] Lin, C. and Lee, Y. (2004), "Stacking sequence optimization of laminated composite structures using genetic algorithm with local improvement", *Composite Structures*, vol. 63, no. 3–4, pp. 339-345.
- [71] Pettit, C. L. and Grandhi, R. V. (2003), "Optimization of a wing structure for gust response and aileron effectiveness", *Journal of Aircraft*, vol. 40, no. 6, pp. 1185-1191.
- [72] Luersen, M. A. and Le Riche, R. (2004), "Globalized Nelder–Mead method for engineering optimization", *Computers & Structures*, vol. 82, no. 23, pp. 2251-2260.
- [73] Bisplinghoff, R. L., Ashley, H. and Halfman, H. (1983), *Aeroelasticity*, Addison Wesley Publishing Co.Inc., Cambridge, Mass.
- [74] Samikkannu, R. and Upadhyaya, A. R. (2011), "Wind Tunnel Flutter Testing of Composite T-Tail Model of a Transport Aircraft with Fuselage Flexibility", in *Wind Tunnels and Experimental Fluid Dynamics Research*, ISBN 978-953-307-623-2 ed, Intech, open access, pp. 75.
- [75] Rezaeepazhand, J. and Simites, G. J. (1996), "Design of scaled down model for predicting shell vibration response", *Journal of Sound and Vibration*, vol. 195, no. 2, pp. 301-311.
- [76] Rezaeepazhand, J. and Yazdi, A. A. (2011), "Similitude requirements and scaling laws for flutter prediction of angle-ply composite plates", *Composites Part B: Engineering*, vol. 42, no. 1, pp. 51-56.
- [77] Wu, Z., Chen, L. and Yang, C. (2013), "Study on gust alleviation control and wind tunnel test", *Science China Technological Sciences*, , pp. 1-10.
- [78] Chen, L., Wu, Z., Yang, C., Tang, C., and Wang, L. (2011), "Gust response, load alleviation and wind-tunnel experiment verification of elastic wing", *Gongcheng Lixue/Engineering Mechanics*, vol. 28, no. 6, pp. 212-218.

- [79] Mai, H., Meumann, J., Hennings, H. (2011), "Gust response: a validation experiment and preliminary numerical simulations", *In Processings of the International Forum on Aeroelasticity and Structural Dynamics-IFASD*, 26-29 June 2011, Paris, France, .
- [80] Penning, K. B., Zink, P. S., Wei, P., De La Garza, A. P., Love, M. H. and Martinez, J. (2008), "GLA and flutter suppression for a SensorCraft class concept using system identification", *Collection of Technical Papers - AIAA Applied Aerodynamics Conference*, .
- [81] Vartio, E., Shimko, A., Tilmann, C. P. and Flick, P. M. (2005), "Structural modal control and gust load alleviation for a SensorCraft concept", *46th AIAA/ASME/ASCE/AHS/ASC Structures, Structural Dynamics and Materials Conference*, Vol. 3, 18 April 2005 through 21 April 2005, Austin, TX, pp. 1799.
- [82] Neumann, J. and Mai, H. (2013), "Gust response: Simulation of an aeroelastic experiment by a fluid–structure interaction method", *Journal of Fluids and Structures*, vol. 38, no. 0, pp. 290-302.
- [83] Niu, M. (1999), *Airframe Structural Design*, 2nd Edition, Conmilit Press Ltd., 22/F, Sing Pao Building, 101 King's Road, North Point, Hong Kong.
- [84] *Aeroelastic analysis user's guide*, V68 ed., MSC Software Corporation.
- [85] Britt, R. T., Crimaldi, J. P. and Rodden, W. P. (1993), "Response of the B-2 aircraft to nonuniform spanwise turbulence", *Journal of Aircraft*, vol. 30, no. 5, pp. 652.
- [86] Regan, C. D. and Jutte, C. V. (2012), *Survey of applications of active control technology for gust alleviation and new challenges for lighter weight aircraft*, TM-2012-216008, NASA, Dryden Flight Research Center, Edwards, California.
- [87] *Certification Specifications and Acceptable Means of Compliance for Large Aeroplanes CS-25*, (2012), amendment 12 ed, European Aviation Safety Agency.

- [88] Howe, D. (2004), *Aircraft loading and structural layout*, Professional Engineering Publishing, Bury St Edmunds.
- [89] Jones, J. G. (2004), *Documentation of the Linear Statistical Discrete Gust Method*, DOT/FAA/AR-04/20, Office of Aviation Research, Washington, D.C .
- [90] *Msc. NASTRAN Aeroelastic Analysis User's Guide*, V68 ed, Msc.software.
- [91] Kim, T., Shin, J. W. and Hwang, I. H. (2007), "Stacking sequence design of a composite wing under a random gust using a genetic algorithm", *Computers & Structures*, vol. 85, no. 10, pp. 579-585.
- [92] Fu, Q. (2013), *Optimization of a Composite Wing Subject to Multi Constraints*, PhD thesis, Cranfield University, Cranfield, Bedfordshire, UK.
- [93] Hexcel Company (2012), *Aerospace Products: HexTow, HexForce, Composites*, available at: <http://www.hexcel.com/products/aerospace/> (accessed 8/2012).
- [94] Guo, S. and Fu, Q. (2011), *Preliminary sizing of skin-stringer panels* , computer programme,. Cranfield University, Cranfield, Bedfordshire, UK
- [95] Guo, S., ( 2002), *College of Aeronautics Laminate Analysis (CoALA)*, computer programme, Cranfield University, Cranfield, Bedfordshire, UK.
- [96] Guo,S.,Fu,Q.,Sensburg,O.K. (2012), "Optimal design of a passive gust alleviation device for a flying wing aircraft", *12th AIAA ATIO/14th AIAA/ISSMO MAO Conference, Session MAO-25*, Indianapolis, Indiana .
- [97] Assair, É. (2012), *Design and Gust Response Analysis of a Composite Flying Wing Aircraft*, Msc. thesis, School of Engineering, Cranfield University, Cranfield, Bedfordshire, UK.
- [98] Luo, W. (2014), *Design and Test of an Aeroelastic Model of a Wing with Passive Gust Alleviation Device*, Msc. thesis, Cranfield University, Cranfield, Bedfordshire, UK.
- [99] Liu, Y. (2010), *Aeroelastic Tailoring of a Composite Wing Subject to Multi Design Constraints*, Msc. thesis, Cranfield University, Cranfield, Beds, UK.



- [100] Hull, D. (1982), "Test methods and design allowables for fibrous composites", *Composites*, vol. 13, no. 2, pp. 104.
- [101] Wen, B. (2010), *Mechanical Design Manual*, vol.1, no. 11, China Machine Press, Beijing
- [102] Shao, K. (2010), "Design of an Adaptive Gust Response Alleviation Control System: Simulation and Experiments", *Journal of Aircraft*, vol. 3, no. 47, pp. 1022.
- [103] Volpe, R. and Silva, A. D. (2013), "Experimental and Numerical Validation of a Wind Gust Facility", *Journal of Fluids Engineering*, vol. 135, no. 1, pp. 011106/1-9.
- [104] Brenner, M. J., Lind, R. C. and and Voracek, D. F. (1997), *Overview of Recent Flight Flutter Testing Research at NASA Dryden*, TM-4792, Dryden Flight Research Center, Edwards, California.
- [105] Tang, D. M., Cizmas, P. G. A. and Dowell, E. H. (1996), "Experiments and analysis for a gust generator in a wind tunnel", *Journal of Aircraft*, vol. 33, no. 1, pp. 139-148.
- [106] Miller, S. (2008), *Lift, drag and moment of a NACA0015 airfoil*, department of aerospace engineering, the ohio state university.
- [107] Jørgensen, F. E. (2002), *How to measure turbulence with hot-wire anemometers*, Dantec Dynamics, Skovlunde, Denmark.
- [108] Cao, X., Liu, J., Jiang, N. and Chen, Q. (2014), "Particle image velocimetry measurement of indoor airflow field: A review of the technologies and applications", *Energy and Buildings*, vol. 69, pp. 367-380.
- [109] Nakanishi, T., Nakamura, T., Watanabe, Y., Handou, K. and Kiwata, T. (2007), "Investigation of air flow passing through louvers", *Komatsu Technical Report*, vol. 53, no. 160.



## APPENDIX A . GUST RESPONSE WITH PGAD

### A.1 PGAD Design

As introduced above, the PGAD has the same aerofoil as the wing and mounted to the wing tip by a rigid shaft and a torsion spring. Based on a previous study [92], shaft location, torsion spring stiffness, mass, and CG are the key parameters for PGAD design to alleviate the gust response. The initial values of parameters for the PGAD are shown in Table A-1.

**Table A-1 PGAD key design parameters for single wing**

	Span (m)	Mass (kg)	CG (% of local chord from LE)	Shaft location (% of local chord from LE)	Spring stiffness (Nm/rad)
Initial value	2	82	44.7%	15%	5.8E4

The PGAD mass and CG had been investigated in a previous parametric study [98]. To quantify the effect of PGAD spring stiffness, the study was carried out with the stiffness altered in a range of 0.1 to 10 times of initial value, CG shifted from 10% to 70%, and the mass changed between 1 and 3 times of initial value. The results indicated that the more flexible the spring, the better the gust alleviation. The mass and CG had less influence on the gust response but would affect the flutter characteristics. For this case, the mass should be less than twice of the initial design and the CG should be ahead of the mid chord.

The torsion spring stiffness was designed to restrict the PGAD rotation angle within 10 degrees to prevent stall. To minimize the interaction between wing and PGAD, the interface is set to run parallel to the air stream. Accordingly the shaft should be normal to the interface to make sure the PGAD can rotate freely. The shaft location 'a', which is defined in Equation (A-1) and Figure A-1, and the torsion spring stiffness (GJ) were taken as independent design variables. In the FE modelling, the shaft and torsion spring are modelled by using spring elements.

$$a = \frac{x_s - x_m}{b_l/2} \quad (\text{A-1})$$

where,

$x_s$  is the shaft x-axis location in global coordinate system;

$x_m$  is the local mid-chord point in global x-axis coordinate;

$b_l$  is the local chord length

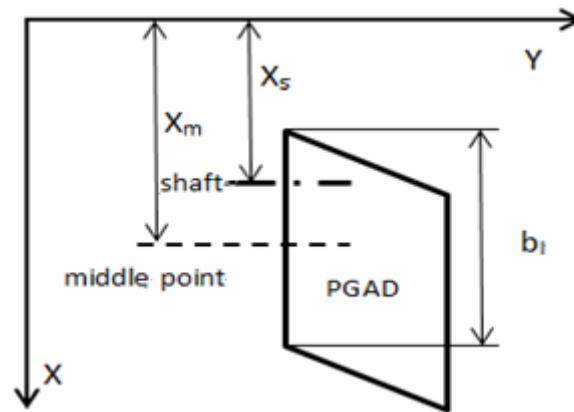


**Figure A-1 Definition of parameter 'a' related variables**

Further investigation on PGAD shaft location was implemented in the following section.

## A.2 Gust Response Analysis

The gust response analysis is presented in four parts: a) First, the analysis was implemented with the aircraft restricted at the centre line which in this case is the same as wing root because of the flying-wing configuration. b) Then the aircraft was set free in Z direction to take the heave motion effect into account. c) Next, after trimming the aircraft longitudinally, the investigation was extended to involve both heave and pitching mode by releasing the translational DoF in Z direction ( $U_z$ ) and rotational DoF in Y direction ( $R_y$ ). d) Finally, further response investigation with an actively controlled device was carried out for better comparison and evaluation.

The All case studies took the same flight conditions of sea level, 0.3 Mach and full fuel mass (MTOM). Results of the first two parts a) and b) presented in last technical report FA8655-11-1-3073 were not included in this report.

## A.2.1 Response with Longitudinal Rigid Body Motion

### A.2.1.1 Aircraft Trim

Normally, an aircraft with tailless flying-wing configuration is statically unstable. Hence an elevon and active control was employed to meet the dynamic stability requirement. The following section presents an investigation into the PGAD efficiency considering the interaction between gust response and stability. Longitudinal analysis, which is relatively simple but typical and important, was involved in the current study.

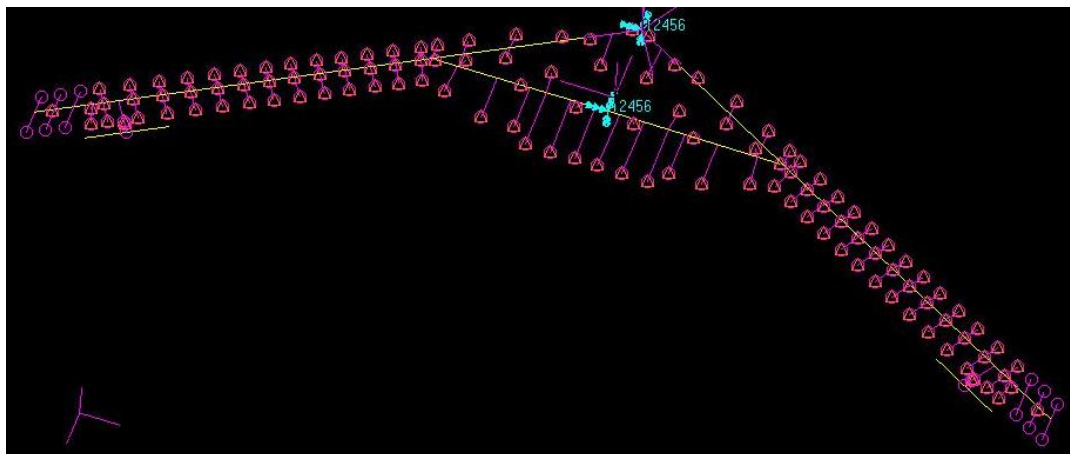


**Figure A-2 Aircraft model with PGAD and elevon**

As shown in Figure A-2, an elevon was added to the FE model to trim the aircraft to level flight condition. The elevon was modelled by rigid beam and concentrated mass (80kg) with its hinge line located at 80% of the local chord. The aerodynamic load was calculated based on the mesh shown in Figure A-3, in which the elevon surface (shown in grey) was 4,000mm span length and 780mm chord length.

Because the stiffness information about the actuator of the elevon was unavailable, an empirical value was applied to fall the rotation frequency into a

practical range. The frequency needed to be high enough to avoid the coupling between the elevon rotation and wing bending, which would decrease the flutter speed significantly. According to modal analysis, the elevon rotation frequency of 30.5Hz was not involved in the undesirable coupling and was unlikely to cause aeroelastic instability problem.

The trim condition was set to 0.3 Mach with MTOM at sea level, the typical gust case. It should be noted that the engine attachment point was moved forward 4m to balance approximately the nose up moment. Without moving the engine position, the elevon would not have been able to trim the aircraft by itself even using the maximum deflection angle of  $30^\circ$ . Finally, the aircraft was trimmed at the AoA of  $-1.3^\circ$  with a small elevon deflection of  $0.17^\circ$ . The abnormal negative AoA, which was in accordance with the CFD result of  $-1^\circ$  [97], was because of the fairly high lift coefficient of the NACA4415 aerofoil ( $C_{l_0} \approx 0.5$ ).

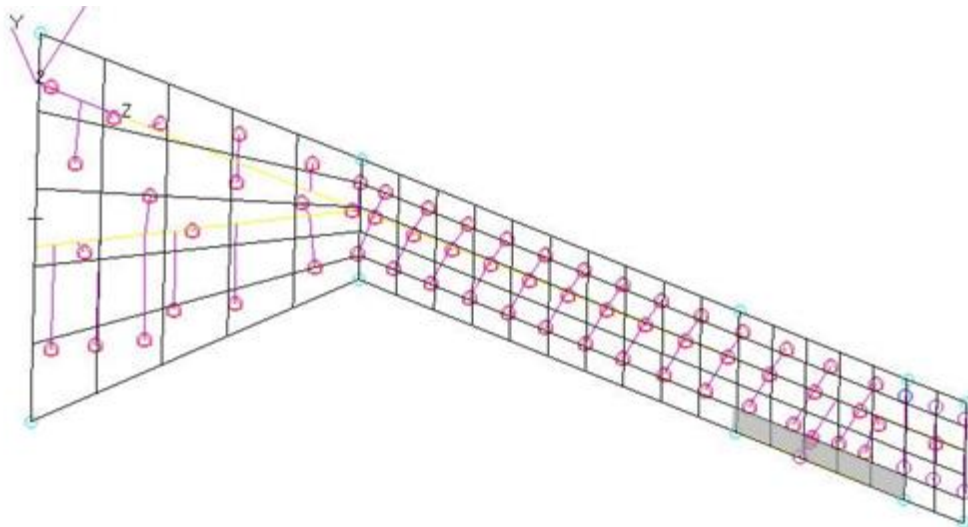


**Figure A-3 Aerodynamic mesh with PGAD and elevon**

#### **A.2.1.2 Response with Heave and Pitching Motion**

Once the aircraft was trimmed longitudinally, the gust response analysis could proceed forward appropriately with both heave and pitching modes included by releasing  $U_z$  and  $R_y$ .

In this case, the gust induced wing tip deflection relative to wing root with heave and pitching motion of the aircraft is shown in Figure A-4. The PGAD passive rotation in response to the gust load is shown in Figure A-5. 'Don', and 'Doff'

indicate the conditions of Device free and Device clamped respectively. As shown in Figure A-4, the 17.3% gust response reduction in terms of wing tip elastic deflection achieved with the PGAD.

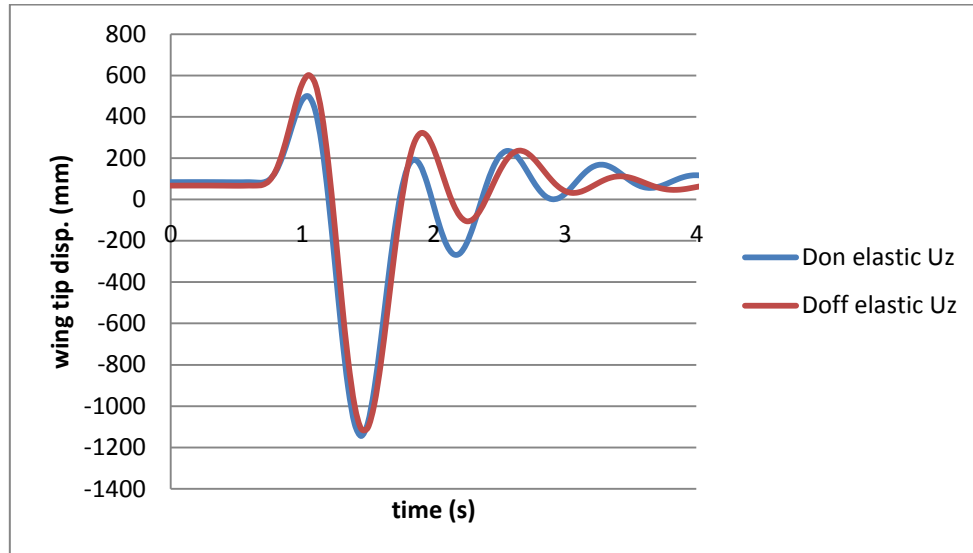


Figure A-4 Wing tip response with heave and pitching mode

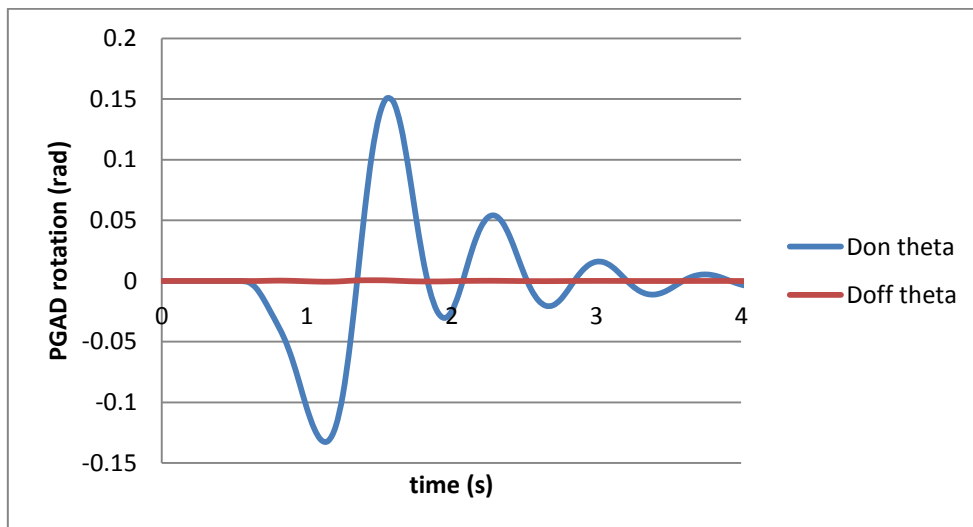
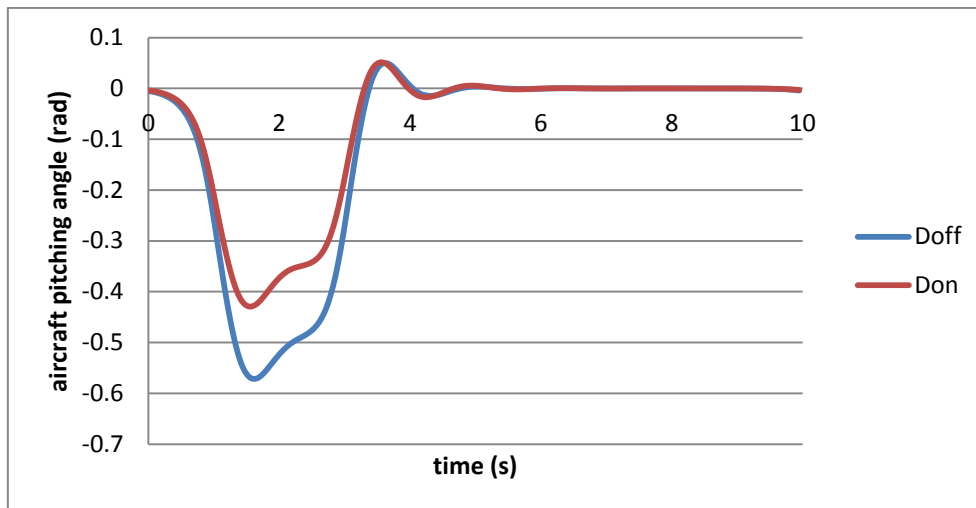


Figure A-5 PGAD rotation with heave and pitching mode



**Figure A-6 Aircraft pitching angle under gust**

The entire aircraft longitudinal gust response is shown in Figure A-6 represented by the pitching angle at CG. Due to the positive increment of lift and pitching moment produced by gust, the aircraft, without a flight control system, experienced a nose down pitching motion. A sufficient alleviation of this response with PGAD activated was observed from the simulation.

### **A.2.2 Open Loop Active Control Case**

In order to make a comparison of the passive gust alleviation with active control, a simple open loop active control of the PGAD was studied. In this case, the wing root was clamped and the gust was set at the same frequency of 0.5Hz, and 0.8Hz respectively. An enforced deflection, with identical amplitude as passive motion of device and exactly opposite phase as gust input, was applied on the PGAD to simulate the active control case.

The response results of the wing are presented in Figure A-7~Figure A-10. Curve legend 'Don Uz', 'Doff Uz' and 'act Uz' mean the wing tip deflection in Z directions with the device on, device off and active control respectively. 'Theta' is the PGAD rotation relative to the wing tip. The angular limit to PGAD rotation was removed to give a clear picture.

In the 0.5Hz gust case, the gust response was reduced by 15.8% for the active device and 8.2% for the passive device, see Figure A-7.

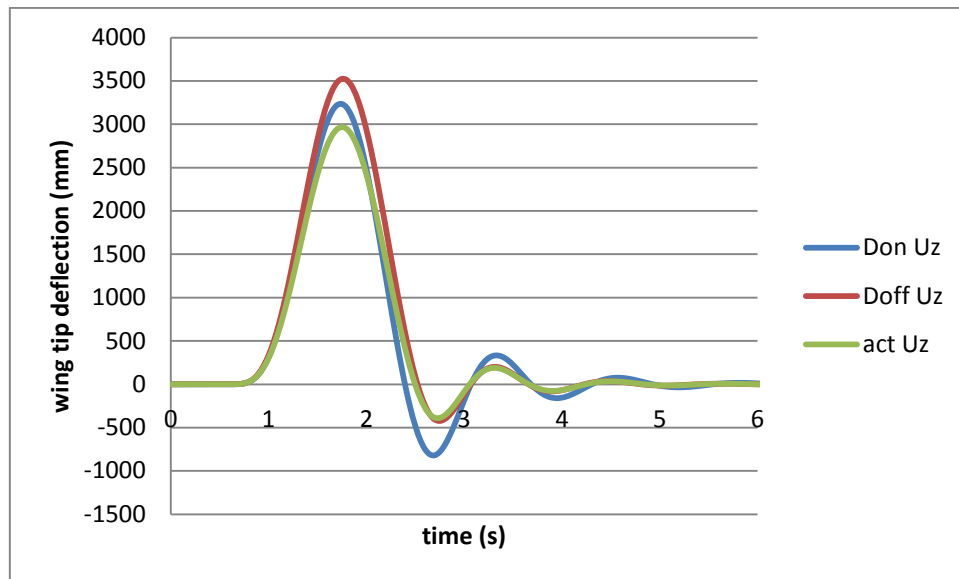


**Figure A-7 Wing tip deflection in response to 0.5Hz gust**

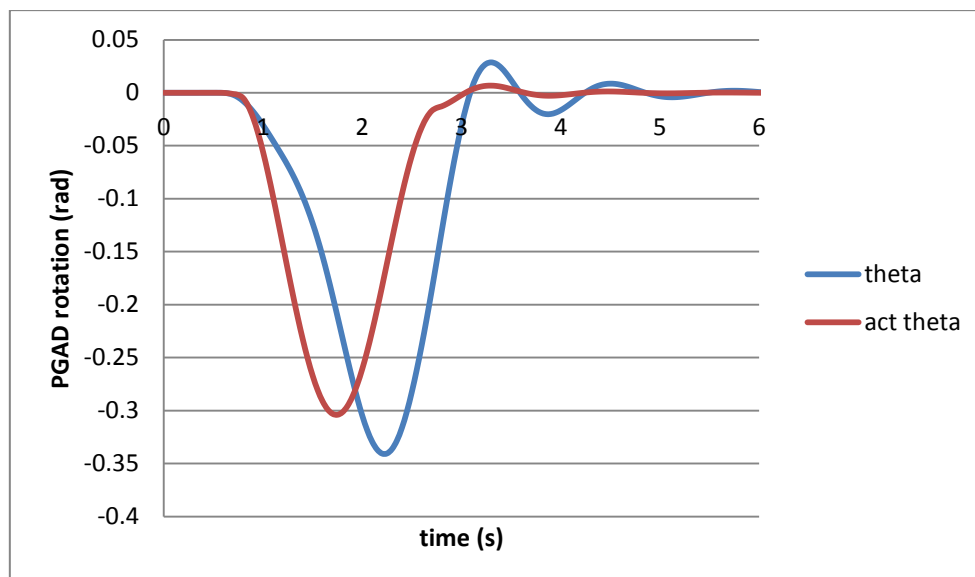


**Figure A-8 PGAD relative rotation at 0.5Hz gust**

In the 0.8Hz gust case, the reduction was 8.4% and 5.8% for active and passive device respectively, see Figure A-9. So, the active controlled device achieved more reduction in the 0.5Hz and 0.8Hz gust input. This is mainly because the specified rotation angle of the active device is larger and the phase much different from the PGAD. It can be observed in Figure A-10 that a clear phase delay of the PGAD occurs for the passive maximum nose down deflection compared with the active device.

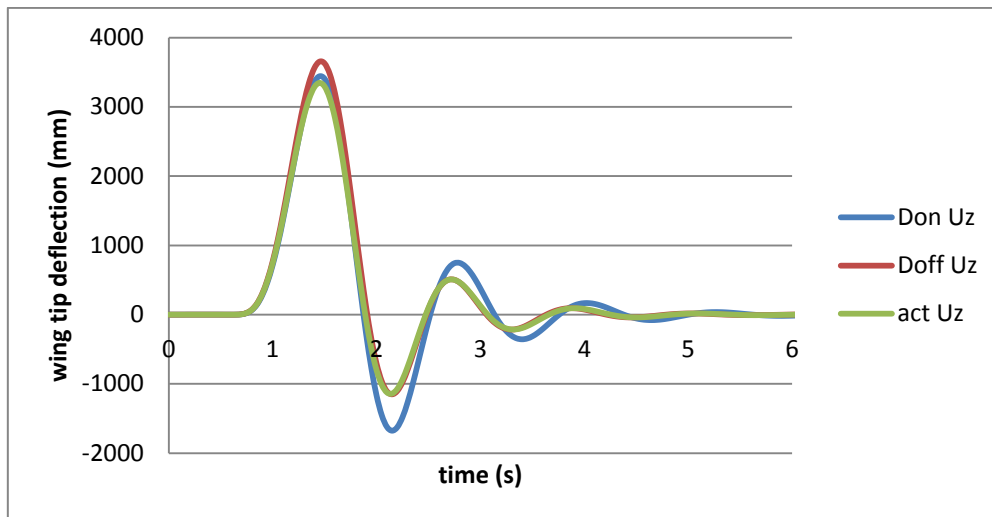


**Figure A-9 Wing tip deflection in response to 0.8Hz gust**

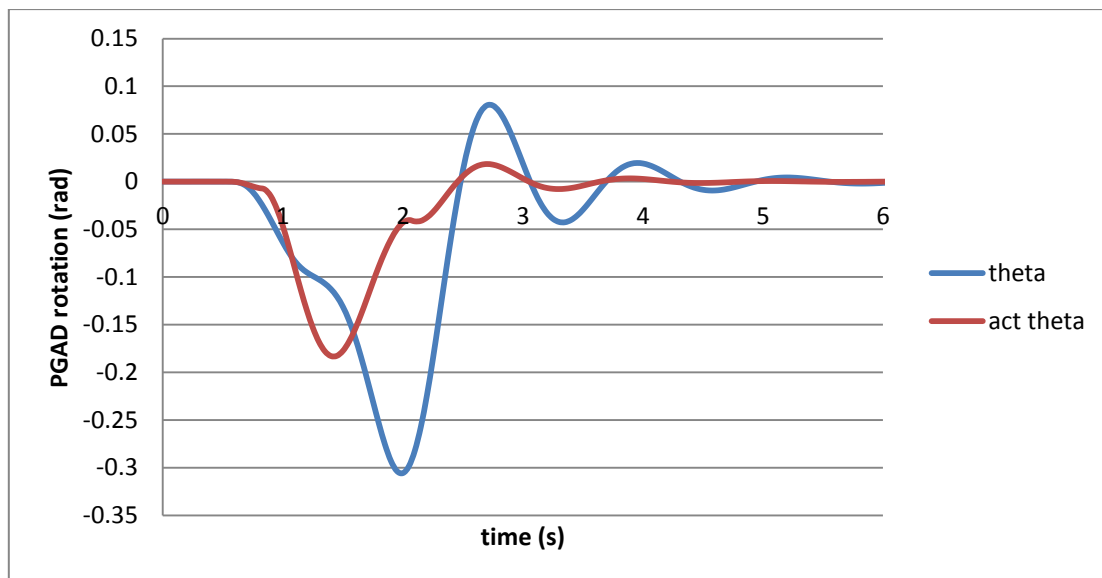


**Figure A-10 PGAD relative rotation at 0.8Hz gust**

The conclusion can be drawn that both passive and active device are effective in gust response alleviation. The efficiency is also related to the phase of deflection motion which is one of the dynamic characteristics of the rotation spring and device mode. So, phase should be another dependent design parameter for focus in the future.



## APPENDIX B . POSSIBLE DESIGNS FOR GUST GENERATOR

There are a few possible designs for a gust generator. A typical configuration is shown in Figure B-1 [102]. Two straight blades with symmetrical aerofoil are mounted on a rigid frame in front of the experimental model in the test section of the wind tunnel. An auxiliary wind tunnel with variable and measurable output as seen in Figure B-2 [103] can be quite helpful to generate the turbulence expected. Another option employing two pairs of vanes installed on the side wall of the tunnel instead of whole blades can achieve the same purpose, see Figure B-3. A fixed vane with a rotational slotted cylinder located at its trailing edge was firstly proposed by Dynamic Engineering Inc. as an onboard flutter exciter [104]. A periodical oscillation is generated by the changing of slot orientation with cylinder spin. It is proved that this type of device can also be applied efficiently in wind tunnel with lower energy requirement due to continuous movement of the cylinder [105].

The first option with two straight blades in front of the model was the best choice for the current study taking into account wind tunnel condition, functional requirements, and cost.

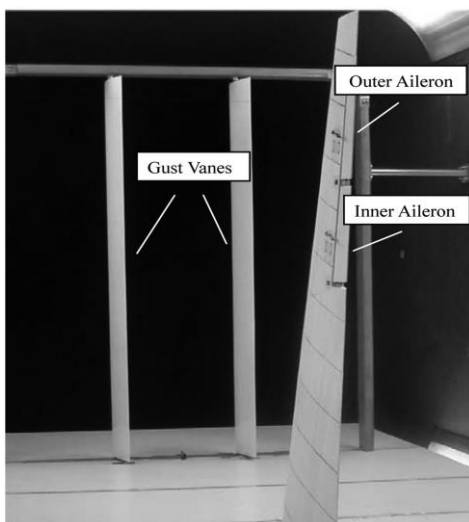


Figure B-1 Gust vane model

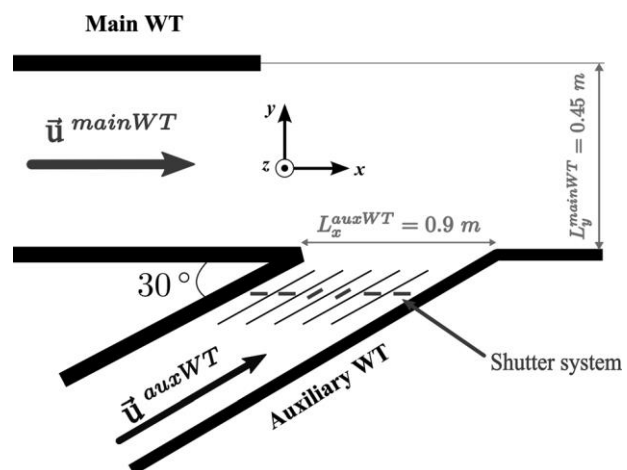


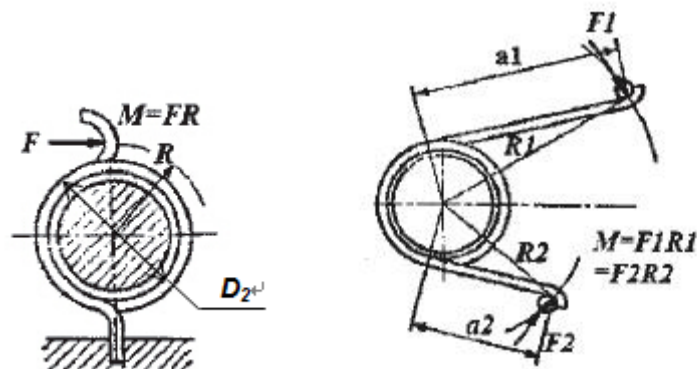
Figure B-2 Generator by an auxiliary WT



Figure B-3 The Gust Oscillator Vanes [81]

## APPENDIX C . TORSION SPRING DESIGN

Generally, there are two kinds of torsion spring categorized by the length of leg as shown in Figure C-1.



a) Short leg spring      b) Long leg spring

Figure C-4 Torsion springs

For the former, spring stiffness can be expressed as Equation C-1.

$$K = \frac{Ed^4}{64D_2n} \quad (\text{C-1})$$

$D_2$ , is mean diameter of coil

$n$ , is number of effective turns

$d$ , is wire diameter

When the condition in Equation B-2 is met, spring will be the long leg one. Spring stiffness should be estimated using Equation B-3.

$$(a_1 + a_2) \geq 0.09\pi D_2 n \quad (\text{C-2})$$

$a_1, a_2$  are leg lengths

$$K = \frac{M}{\alpha} = \frac{EI}{l} = \frac{E\pi d^4}{64[\pi D_2 n + \frac{1}{3}(a_1 + a_2)]} \quad (\text{C-3})$$

The final design parameters of the torsion spring are listed in Table C-1.

**Table C-1 Spring design parameters**

D2 (mm)	E (Gpa)	d (mm)	n	a1 (mm)	a2 (mm)
12	200	0.75	1.5	12	12

So, Equation C-2 is met and the practical spring stiffness calculated from Equation C-3 is 47.9 Nmm/rad.

## APPENDIX D . TEST INSTRUMENTS SPECIFICATIONS

The instruments needed are introduced briefly based on their own application scope. Detailed specifications can be found in the user manuals.

### a) Accelerometer

A piezoresistive accelerometer shown in Figure D-5 is fixed at the tip of outboard spar to get the acceleration in vertical direction. Both time and frequency domain response can be extracted from accelerometer output. Mode type cannot be identified directly with only one accelerometer, but nevertheless it could be classified by other techniques.



Figure D-5 Accelerometer

### b) Strain gauge

Two sets of strain gauges in pure bending full bridge configuration were attached to both surfaces at the roots of the front and rear spars respectively as seen in Figure D-6 and Figure D-7.

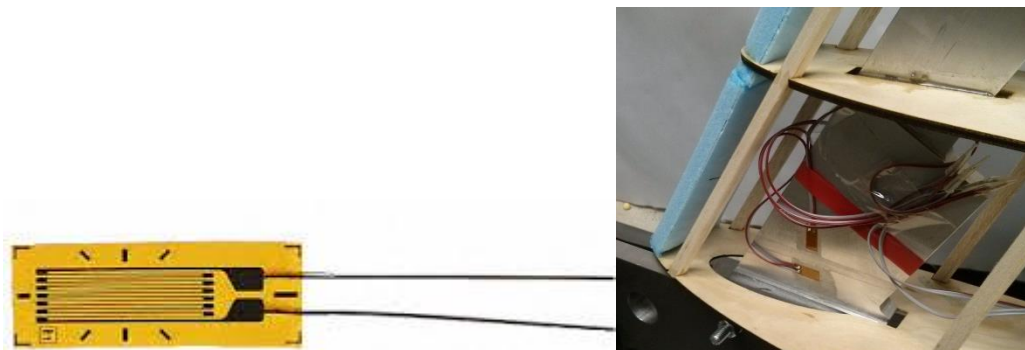


Figure D-6 Strain gauge

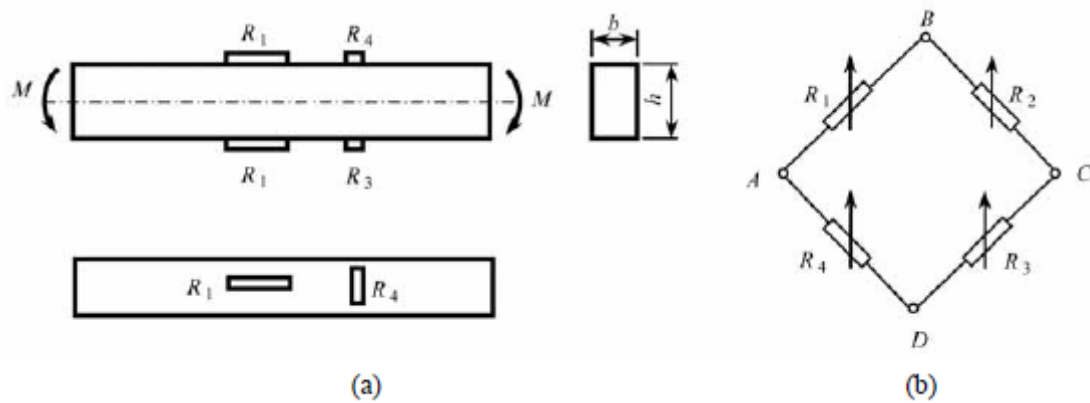


Figure D-7 Pure bending full bridge configuration

$$\varepsilon_{bending} = \frac{\varepsilon_{reading}}{2(1 + \mu)} \quad (D-4)$$

Bending strain of the beam could be expressed as Equation (D-4). Temperature and tension/compression effects were eliminated by this type of circuit connection.

#### c) Geometrical measurement

Solution1: laser distance measuring instrument as shown in Figure D-8

Two different points on the rigid part of the wing tip and the PGAD tip respectively were specified as reference points for the laser test method. Linear and rotational deformation could be achieved by simple data reduction. This method could give very accurate results but was not so flexible in regard to working distance and range.

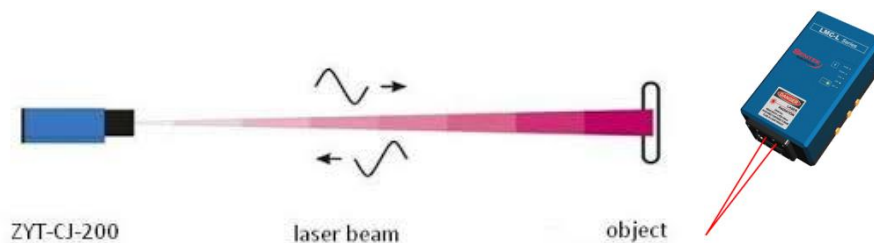
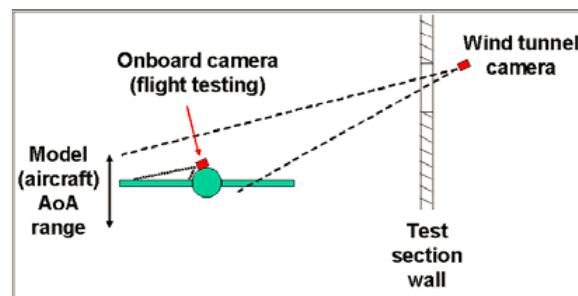


Figure D-8 Laser distance measuring instrument

Solution 2: High speed video camera as shown in Figure D-9

Geometrical parameters for the whole wing can be computed by specific digital graphic processing technology.



**Figure D-9 Illustration of differing camera geometries for wind tunnel**

In this case, a high speed camera was more applicable considering the range and instrument availability.

d) Air speed measurement

There are 3 methods normally used in flow field measurement as following.

Solution 1: Hot-wire anemometer system

The hot-wire anemometer system as shown in Figure D-10 consists of sensors, data acquisition module and PC terminal which provides a user interface and data post-processing. A typical hot-wire probe is shown in Figure D-11 which was the core component for this measurement [107].

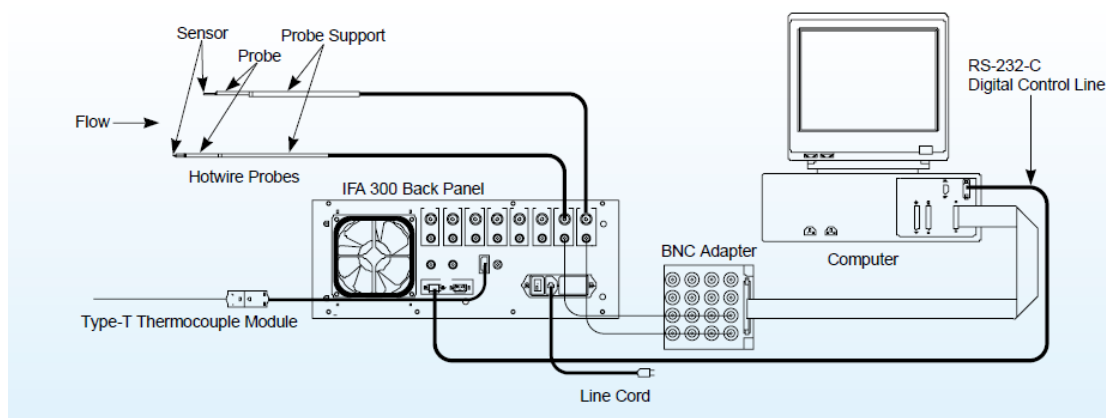


**Figure D-10 Hot-wire anemometer system**

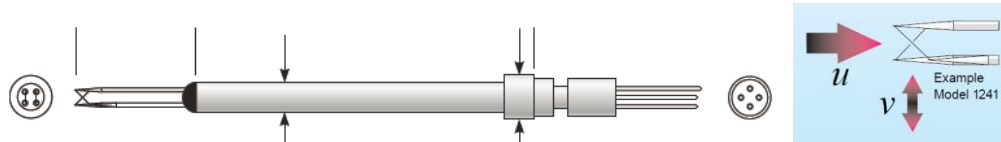


**Figure D-11 Hot-wire probe**

#### Solution 2: PIV method

A more efficient option is Particle Image Velocimetry (PIV), which acquires the flow field characteristics in any specified plane in one run [108]. The system includes high energy laser, high resolution CCD camera synchronizer timing unit, seed particle generator and capture and analysis software, see Figure D-12.

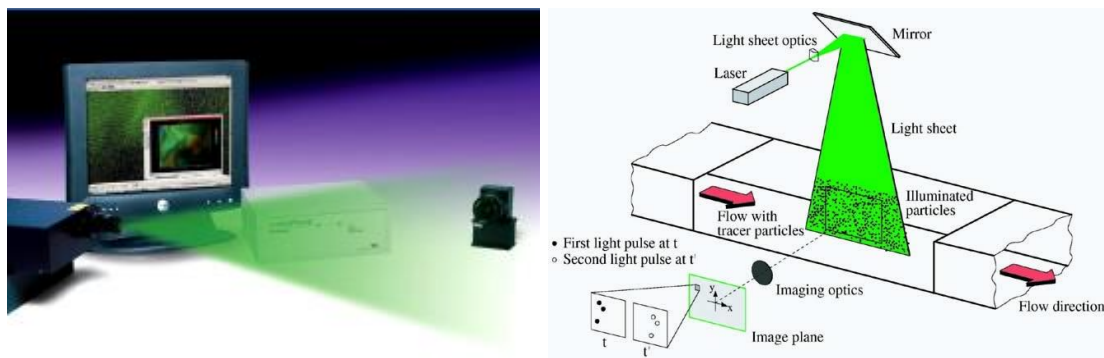


**Figure D-12 2D PIV system**

#### Solution 3: LDV method [109]

Laser Doppler velocimetry (LDV) is shown in Figure D-13, which consists of laser, incident optical unit, frequency shift system, receiving optical unit, seed particle generator and signal processing software. The technique uses the Doppler shift in a laser beam to measure the velocity in fluid flows.



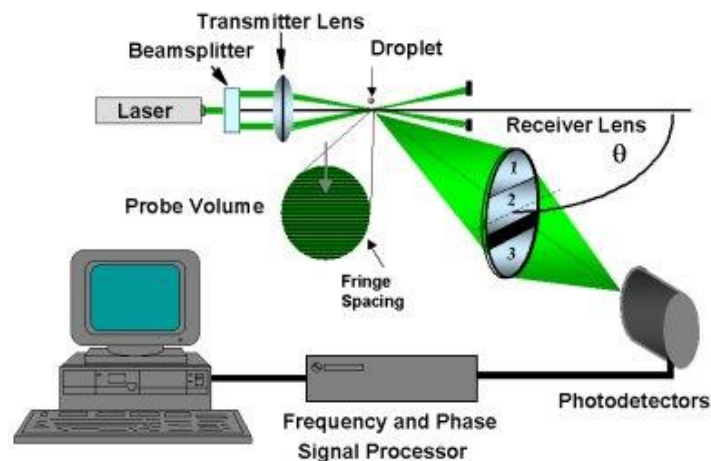


**Figure D-13 LDV system**

However, none of the instrument above for airflow measurement was available for the test. An alternative method was proposed using two sets of Pitot probes. One L-shape probe was fixed on the ceiling as reference and the other set of probes was installed on the test point as required. The 4-hole probe was composed of 1 hole for static pressure and 3 holes for total pressure with  $-15^\circ$ ,  $0^\circ$  and  $15^\circ$  incident angle with straight airflow as shown in Figure D-14. So, in the whole range of blade AoA variations, there will always be a difference between those 3 holes which after calibration can be used to calculate the gust velocity in a cross section.



**Figure D-14 Pitot probe installation in wind tunnel**